



**UNIVERSITAT POLITÈCNICA DE CATALUNYA  
BARCELONATECH**

---

**Escola Tècnica Superior d'Enginyeria  
de Telecomunicació de Barcelona**

**Six Degree of Freedom Force/Torque Sensor**

**A Master's Thesis**

**Submitted to the Faculty of the  
Escola Tècnica d'Enginyeria de Telecomunicació de  
Barcelona**

**Universitat Politècnica de Catalunya**

**by**

**Oriol Escoté i Lluís**

**In partial fulfilment  
of the requirements for the degree of  
MASTER IN ELECTRONIC ENGINEERING**

**Advisor: Antoni Turó**

**Barcelona, November 2017**



UNIVERSITAT POLITÈCNICA  
DE CATALUNYA  
BARCELONATECH



**Title of the thesis:** Six Degree of Freedom Force/Torque Sensor

**Author:** Oriol Escoté i Lluís

**Advisor:** Antoni Turó

## **Abstract**

This work describes the design, development and calibration of a complete six-degree-of-freedom force and torque sensor.

Compared to commercial sensors, this design has the advantage of simplicity and low cost. The sensor was machined from aluminium, and sensed by an array of commercial low-cost strain gauges. As a sensor, it could be applied in multi-DOF industrial, scientific and medical robotic systems, for instance.



To my parents.

## **Acknowledgements**

My acknowledgement to the ESAll department to let me use their installations to do this project, and to Professor Antoni Turó for his helpful.

## Revision history and approval record

Revision	Date	Purpose
0	07/09/2015	Document creation
1	18/11/2015	Introduction and State of Art
2	12/5/2016	Mechanical design
3	06/03/17	Electronics design
4	09/05/17	Measurements
5	20/06/17	Calibration

Written by:		Reviewed and approved by:	
Date	10/11/2017	Date	10/11/2017
Name	Oriol Escoté	Name	Antoni Turó
Position	Project Author	Position	Project Supervisor

## Table of contents

Abstract .....	1
Acknowledgements .....	3
Revision history and approval record.....	4
Table of contents .....	5
List of Figures.....	8
List of Tables .....	13
1. Introduction.....	15
1.1. Requirements and specifications .....	17
1.2. Work plan .....	19
2. State of the art of the technology .....	20
2.1. DOF .....	20
2.2. Technology used.....	21
2.2.1. Resistive.....	21
2.2.2. Magnetic.....	23
2.2.3. Optic.....	24
2.3. Mechanical frame .....	29
2.3.1. Classical columns.....	29
2.3.2. Classical tubes .....	30
2.3.3. Cantilever Beams .....	31
2.3.4. Middle bent bars with fixed ends.....	32
2.3.5. Others .....	34
3. Mechanical design.....	35
3.1. Introduction.....	35
3.2. Frame & Material selection .....	35
3.3. Sketch .....	37
3.4. Dynamic Simulation.....	41
3.4.1. Model Developement.....	42
3.4.2. ANSYS Simulation.....	51
3.5. Post Process .....	59
3.6. Milling .....	61
4. Electronics design .....	64
4.1. Introduction.....	64

4.2.	Circuit & Component selection.....	64
4.2.1.	Circuit topology.....	66
4.2.2.	Strain gauges .....	67
4.2.3.	Wheatstone bridge .....	68
4.2.4.	Bridge balancing.....	74
4.2.5.	Instrumentation Amplifier.....	77
4.2.6.	Amplifier .....	79
4.2.7.	Digital Communications.....	81
4.2.8.	ADC .....	83
4.2.9.	Micro Controller .....	88
4.2.10.	Sensors .....	91
4.2.11.	Supply.....	93
4.2.12.	Timing.....	94
4.2.13.	PCB .....	97
5.	Software program.....	98
5.1.	Introduction.....	98
5.2.	Functions.....	99
6.	Results .....	104
6.1.	Introduction.....	104
6.2.	Setup.....	105
6.3.	Sensor characterization .....	106
6.3.1.	Channel response .....	106
6.3.2.	Accuracy .....	107
6.3.3.	Precision .....	107
6.3.4.	Repeatability.....	108
6.3.5.	Drift .....	109
6.3.6.	Noise.....	110
6.3.7.	Resolution .....	112
6.3.8.	Measurement Range.....	112
6.3.9.	Response and Recovery Time .....	112
6.3.10.	Linearity .....	112
6.3.11.	Sensitivity .....	114
6.3.12.	Hysteresis.....	114
6.4.	Calibration .....	115



6.4.1.	Matrix .....	116
6.4.2.	Calibration .....	118
6.4.3.	Calibration matrix calculation .....	127
7.	Budget.....	136
7.1.	Introduction.....	136
7.2.	Tasks.....	136
7.3.	Personnel costs.....	137
7.4.	Material costs .....	137
7.5.	Total cost of development.....	138
7.6.	Cost per unit of the force sensor.....	138
8.	Conclusions and future development.....	139
8.1.	Conclusions.....	139
8.2.	Future development.....	140
	Bibliography.....	141
	Annexes .....	144

## List of Figures

Figure 1-1. General F/T Sensor diagram blocks .....	15
Figure 1-2. Motion Control Coordinate System .....	16
Figure 1-3. ATI Gamma XXX sensor .....	17
Figure 1.4 – Work distribution .....	19
Figure 2-1. Load cell ( <a href="http://www.coventryscale.co.uk/">http://www.coventryscale.co.uk/</a> ) .....	20
Figure 2-2. Degrees of freedom .....	20
Figure 2-3. Electrical conductance.....	21
Figure 2-4. Example of magnetic flux characteristic in push-pull slide-by magnet configuration ( <a href="http://www.allegromicro.com/">http://www.allegromicro.com/</a> ) .....	23
Figure 2-5. Example of an angle of incidence sensor [1].....	25
Figure 2-6. Loss of light in a fibre under compression [24].....	25
Figure 2-7. Wavelength filtered.....	26
Figure 2-8. Change of $\lambda$ under tensile stress .....	27
Figure 2-9. Compressed column.....	30
Figure 2-10. Compressed tube .....	31
Figure 2-11. Helical load cell.....	31
Figure 2-12. Cantilever beam .....	32
Figure 2-13. Contact mode AFM ( <a href="http://www.physik.uni-greifswald.de/">http://www.physik.uni-greifswald.de/</a> ) .....	32
Figure 2-14. Middle bent bars with fixed ends.....	33
Figure 2-15. Patent US3956930 A.....	33
Figure 2-16. Stewart Platform in a surgical tool (in yellow). ( <a href="http://www.robotic.dlr.de/">http://www.robotic.dlr.de/</a> )...	34
Figure 2-17. Basic structure of SPIDAR-G.....	34
Figure 3-1. Mechanical work diagram .....	35
Figure 3-2. Three and four arms middle bent bars with fixed ends frame.....	35
Figure 3-3. Sensor sections .....	37
Figure 3-4. SolidWorks 2014 .....	37
Figure 3-5. Middle section .....	38
Figure 3-6. Bottom section.....	38
Figure 3-7. Spacer between sensor and PCB.....	39
Figure 3-8. Holes and fixed support element .....	39
Figure 3-9. Thick analysis for 25° between fixing holes.....	40
Figure 3-10. Thick analysis for 20° between fixing holes.....	40

Figure 3-11. Thickness in compliant beams .....	40
Figure 3-12. Cura Software.....	40
Figure 3-13. 3D plastic model .....	41
Figure 3-14. Parameters.....	42
Figure 3-15. Beam sections .....	42
Figure 3-16. Infinitesimal section of a Timoshenko beam .....	44
Figure 3-17. Frame deformation under $F_x$ (force in purple arrows, fixed face in green) ..	45
Figure 3-18. Mechanical model under $F_x$ .....	45
Figure 3-19. Frame deformation under $F_z$ (force in purple arrows, fixed face in green) ..	46
Figure 3-20. Mechanical model under $F_z$ .....	46
Figure 3-22. Frame deformation under $M_x$ (force in purple arrows, fixed face in green)..	48
Figure 3-21. Mechanical model under $M_x$ .....	48
Figure 3-23. Mechanical model under $M_x$ .....	50
Figure 3-24. Frame deformation under $M_z$ (force in purple arrows, fixed face in green)..	50
Figure 3-25. Stress in a 3D solid.....	52
Figure 3-26. Strain vs. Stress .....	54
Figure 3-27. Solid mesh of the frame structure .....	54
Figure 3-28. Von Mises Stress simulation under $F_x$ (Deformation scale: 803) .....	55
Figure 3-29. Displacement simulation under $F_x$ (Deformation scale: 803) .....	55
Figure 3-30. Safety factor stress test .....	56
Figure 3-31 Von Mises Stress simulation under $F_z$ (Deformation scale: 1487.28) .....	57
Figure 3-32. Displacement simulation under $F_z$ (Deformation scale: 1487.28).....	57
Figure 3-33.Safety factor stress test .....	57
Figure 3-35 Von Mises Stress simulation under $M_x$ (Deformation scale: 8799).....	58
Figure 3-34. Displacement simulation under $M_x$ (Deformation scale: 8799).....	58
Figure 3-37. Von Mises Stress simulation under $M_z$ (Deformation scale: 8130.3).....	58
Figure 3-36. Displacement simulation under $M_z$ (Deformation scale: 8130.3).....	58
Figure 3-38. SolidWorks CAM Post Process.....	59
Figure 3-39. AutoCAD Post Process.....	60
Figure 3-40. Sinumerik 820 Program .....	60
Figure 3-41. Sinumerik 820 Simulation .....	60
Figure 3-42. EMCO ConceptMill 55 .....	61
Figure 3-43. Centre drill .....	61
Figure 3-44 2.4mm drill.....	61

Figure 3-46. 8mm flat end mill .....	62
Figure 3-45. 8mm flat end mill .....	62
Figure 3-48. Frame in known position.....	62
Figure 3-47. 4mm flat end mill .....	62
Figure 3-49. 4mm flat end mill .....	62
Figure 3-50. Mechanical work finished.....	63
Figure 4-1. Electronic work diagram .....	64
Figure 4-2. General structure of a force measurement chain .....	64
Figure 4-3. Different simultaneous sampling circuits.....	65
Figure 4-4. Parallel amplifiers and an in circuit multiplexed ADC .....	67
Figure 4-5. Gauge misalignment.....	68
Figure 4-6. Wheatstone Bridge .....	68
Figure 4-7. A pair of dummy gauges shared by eight half bridges.....	72
Figure 4-8. Strain gauges glued in the frame .....	73
Figure 4-9. NCV4274 Block diagram .....	73
Figure 4-11. Parallel resistor.....	74
Figure 4-10. Serial resistor .....	74
Figure 4-12. Detailed Functional Block Diagram of AD5171 .....	75
Figure 4-13. Balancing circuit schema .....	76
Figure 4-14. AD8293G160 typical use .....	77
Figure 4-15. OPA336.....	79
Figure 4-16. OPA336 in non-inverter configuration and variable gain .....	79
Figure 4-17. AD5254 functional block diagram .....	80
Figure 4-18. I2C vs. SPI protocols .....	81
Figure 4-19. ADC architectures, resolution vs. sampling rates.....	83
Figure 4-20. MAX11628 block diagram.....	85
Figure 4-21. Clock Mode 10 Timing .....	86
Figure 4-22. ISL60002 noise reduction network.....	87
Figure 4-23. ATmega328 block diagram.....	89
Figure 4-24. Arduino mini v5 board.....	89
Figure 4-25. USB to serial cable converter .....	90
Figure 4-26. Low voltage sensor.....	91
Figure 4-27. Temperature sensor .....	91
Figure 4-28 3-axis accelerometer .....	92

Figure 4-29. Adafruit module .....	92
Figure 4-30. Low pass filter input.....	94
Figure 4-31. MAX11628Timing diagram .....	95
Figure 4-32. PCB A and B .....	97
Figure 4-33. PCB's attachments .....	97
Figure 5-1. Software Flowchart.....	98
Figure 6-1. Z force setup .....	105
Figure 6-2. X and Y force setup .....	105
Figure 6-3. X and Y torque setup.....	105
Figure 6-4. Z torque setup .....	106
Figure 6-6 force in Z axis .....	106
Figure 6-5 Channels outputs.....	106
Figure 6-8 force in X axis.....	107
Figure 6-7 force in Y axis.....	107
Figure 6-9 Precision Gaussian distribution.....	108
Figure 6-10. Repeatability test .....	108
Figure 6-11. Repeatability Gaussian distribution.....	109
Figure 6-12 Drift test.....	109
Figure 6-13 Noise test .....	110
Figure 6-14 Noise vs. N_bits.....	111
Figure 6-15 Noise vs. Averaging.....	111
Figure 6-16 Calibration curve in +Z axis .....	113
Figure 6-17 Hysteresis test on Z axis.....	114
Figure 6-18 Hysteresis result on Z axis.....	115
Figure 6-19 Results and sensing channels relationships .....	118
Figure 6-22. Z torque setup .....	119
Figure 6-20. Weights used.....	119
Figure 6-21. X and Y force, X and Y torque and Z force setups .....	119
Figure 6-23. +FY test.....	120
Figure 6-24. +FX test.....	121
Figure 6-25. +FZ test .....	122
Figure 6-26 +MX test.....	123
Figure 6-27. +MY test .....	124
Figure 6-28. +MZ test .....	125

Figure 6-29. – Force and Torque in +FY test .....	130
Figure 6-30. – Force and Torque in +FY test .....	131
Figure 6-31. – Force and Torque in +FZ test .....	132
Figure 6-32. – Force and Torque in +MY test .....	133
Figure 6-33. – Force and Torque in +MX test .....	134
Figure 6-34. – Force and Torque in +MZ test.....	135

## List of Tables

Table 1- Comparisons between commercial F/T sensor and the new prototype specifications.....	18
Table 2 - Comparisons on the multi-dimensional F/T sensor .....	28
Table 3 - Advantages and disadvantages of different models .....	36
Table 4 - Aluminium alloy 5083 Composition .....	36
Table 5 - Thickness Analysis .....	39
Table 6 - $\beta$ coefficient vs. b/h ratio .....	48
Table 7 - Aluminium alloy 5083 Properties (The Aluminum Association, Inc.) .....	55
Table 8 - Program descriptions .....	59
Table 9 - Bridge Configurations for uniaxial members.....	72
Table 10 – Current consumption.....	93
Table 11 – Float multiplication speed test program.....	96
Table 12 – ADC values in +FY test.....	120
Table 13 – percentage of variation of each channel in +FY test.....	120
Table 14 – ADC values in +FX test.....	121
Table 15 – percentage of variation of each channel in +FY test.....	121
Table 16 – ADC values in +FZ test .....	122
Table 17 – percentage of variation of each channel in +FZ test .....	122
Table 18 – ADC values in +MX test .....	123
Table 19 – percentage of variation of each channel in +MX test .....	123
Table 20 – ADC values in +MY test .....	124
Table 21 – percentage of variation of each channel in +MY test.....	124
Table 22 – ADC values in +MZ test .....	125
Table 23 – percentage of variation of each channel in +MZ test .....	125
Table 24 – Force and Torque values in +FY test .....	130
Table 25 – Force and Torque values in +FX test .....	131
Table 26 – Force and Torque values in +FZ test .....	132
Table 27 – Force and Torque values in +MY test .....	133
Table 28 – Force and Torque values in +MX test .....	134
Table 29 – Force and Torque values in +MZ test.....	135
Table 30 – Tasks definition and hour cost.....	136
Table 31 – Tasks definition and hour cost.....	137

Table 32 – Material costs.....	137
Table 33 – Annual cost of equipment.....	138
Table 34 – Total cost .....	138
Table 35 - Comparisons between commercial F/T sensor, proposed specifications and goals achieved.....	139



# 1. Introduction

The use of robots and manipulators in many kind of applications such as scientific, medical or industrial requires efficient multi-component force sensing schemes to control the force exerted by the robot end-effector on a human or an object.

The main purpose in utilizing a multiaxis force sensor is to measure the contact force as accurately as possible, and to feed it back to the command signal so that the robot can achieve the pre-specified contact force.

In general, multiaxis force sensors are devices in which several small transducers measure unknown loads (normally three forces and moment components) applied to the robot end-effector. A typical force and torque sensor (figure 1.1) consists of an elastic structure affected by forces and torques. The physical change is converted to very small electrical changes (in order of micro-volts), that must be filtered and amplified before an analog-to-digital converter (ADC), converts it to the data which is digitally filtered and processed by a microcontroller.

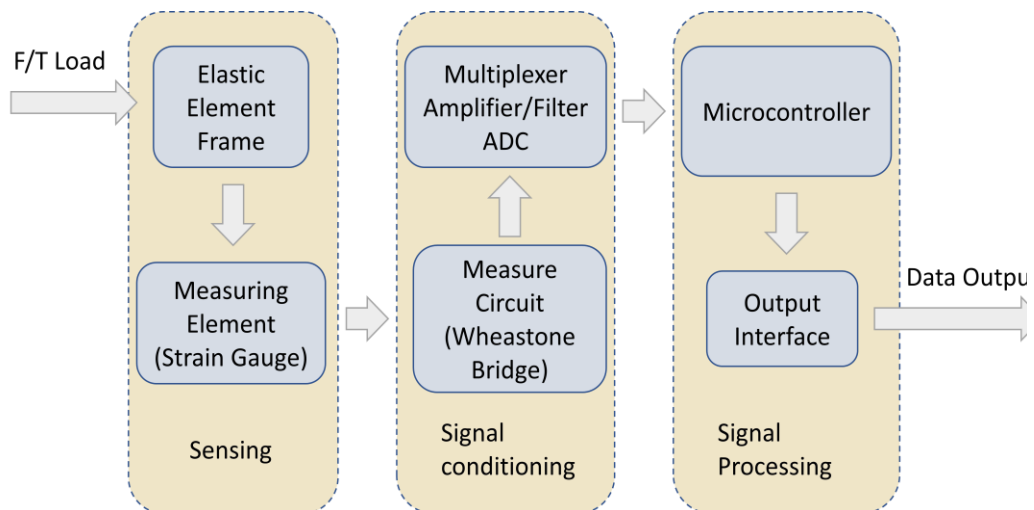


Figure 1-1. General F/T Sensor diagram blocks

The force component output is represented by deformations sensed by n strain gauges glued on the deformable part. The estimation of the applied force/torques from the strain measurements is usually obtained by assuming a quasi-static relationship between the forces applied at the strains. This assumption is maintained even if the force is time varying. The faster the deformation sensing is, the larger the bandwidth of the sensor will be. The force vector components are derived from these strain measurements, and they will give an output vector as

$$z = [z_1 z_2 z_3 \dots z_n]^T$$

In some cases, the flexibility of the mechanical structure is such that the measured strains include components due to the vibration of the structure, and consequently the estimation of the applied, time-varying, force cannot be done by using quasi-static relationships. If the sensor body has been designed to remain in the elastic region, the superposition principle is applicable; in consequence, the relationship between internal strains and external forces is therefore linear.

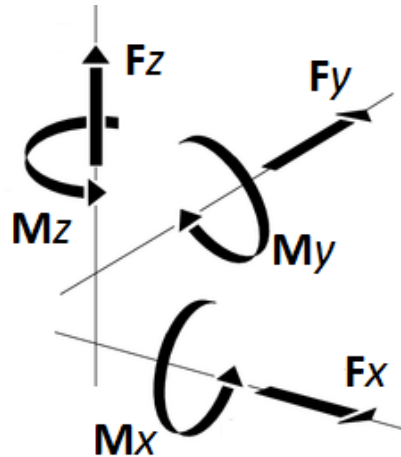


Figure 1-2. Motion Control  
Coordinate System

This can be written in a matrix form:  $[z_1 z_2 z_3 \dots z_n]^T = C[F_x F_y F_z M_x M_y M_z]^T$  (figure 1-2) where  $C$  is an  $n \times 6$  matrix called “calibration matrix”. This relation needs to be inverted to derive the force components from the measurement of  $n$  strain transducers. When the number of strain transducers exceeds six, pseudo-inverse matrix calculations have to be used.

In this work, it is proposed not a completely new design of a three arms sensor, but a low-cost version of the commercial ones. In this case, the result of the work can't be commercialized because the frame is subject to the patent EP 2510325 A2, where multiaxial force-torque sensors having a transducer structure are patented, with strain gauges placed in defined areas to measure the strain, from which the forces and torques are calculated, and where the transducer structure advantageously consists of two concentric rings connected with spokes. The transducer structure is a planar mechanical structure and all strain gauges are placed to the same surface of the structure in a way that non-radial strain components are measured [1].

This project consist of four different parts. First of all it is necessary to design, simulate and build the frame of the sensor where the strain gauges will be glued. Secondly, a design and implementation of a PCB where the electronic signal will be amplified, filtered and converted into digital data. Third part is to program a microcontroller that will process this data and will be the interface with the computer and/or user. And finally, it is necessary to calibrate the sensor in order to permit the user to know each force and torque.

### 1.1. Requirements and specifications

In the Departament d'Enginyeria de Sistemes, Automàtica i Informàtica Industrial (ESAI), commercial multiaxis force sensor have been using to control their robots. The price of one of this commercial sensors, for example the ATI Gamma (figure 1-3) with an estimated cost of, is of 6000 euros approximately, plus 2000 euros for the National instruments board to measure the sensor voltages.



Figure 1-3. ATI Gamma XXX sensor

The objective of this work is to make a multiaxis force sensor that could replace the commercial ones in most cases.

Because of this, the main requirement is that the fixing points to the robot and to the end-effector must be the same ones, in order to use the same robot and the same tools as in the commercial ones.

The second requirement is that the data given by the sensor must be compatible with the software developed until now.

As the ATI sensor uses a 24 bits National Instruments AD board, the data of the sensor is of 24 bits, but only 12 of them are useful because of the length of the data. Therefore a 12 bits AD converter is enough to cover the uses given right now.

The National instruments board can give up to 100k data per second. This amount of data is not necessary because the sensors are used to measure the force applied by an operator, in order to move the robot. It is considered that 100 samples per second is enough to use the sensor in most cases for manual manipulation.

One of the problems of the use a National instruments board, is that the data can only be processed by the computer that have the board installed, and as the board is PCI type, is not easy to use any computer we want. To improve the usability of the sensor, the new sensor will support more data protocols, at least, USB and Ethernet.

Finally, we want that the cost of the new sensor will be a 10% of the original one.

	ATI Gamma	Prototype proposed
Data byte	24	10/12
Baud rate	100k/s	100/s
Software	Closed	Open source
Communications	PCI board	Serial      USB, Ethernet
Price	8000€ approximately	<800€

Table 1- Comparisons between commercial F/T sensor and the new prototype specifications

### 1.2. Work plan

This project has been divided in 15 different tasks which can be seen in the follow Gantt diagram (figure 1.4), with the time necessary to finish, expressed in weeks

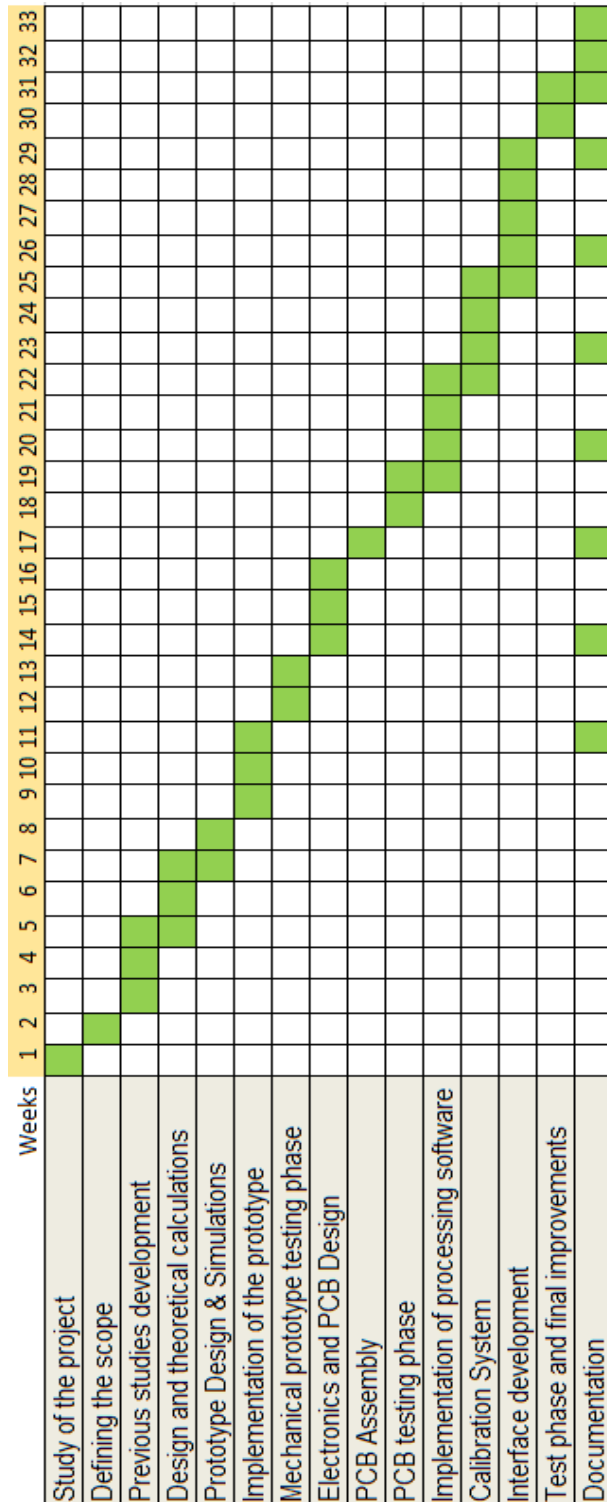


Figure 1.4 – Work distribution

## 2. State of the art of the technology

Different classifications of force sensors can be done depending on the number of degrees of freedom (DOF) measured, technology used or type of mechanical frame.

### 2.1. DOF

In mechanics, Degrees of freedom (DOF) refer to the possible movements of a rigid body in three-dimensional space. In sensors, means the number of different forces/torques that can be measured (figure 2-2). X, Y and Z are forces, and  $\theta_x$ ,  $\theta_y$  and  $\theta_z$  are torques around each axe.

Force torque sensors are built from a mechanical transducer structure which is installed at the position where forces and torques are to be determined.

A classification according to DOF is:

- 1 DOF: give information about a component force or torque. These sensors are cheap and usually use technology based on strain gauges. The most common applications are torque sensor of a spinning axe, or load cells for weight sensors (figure 2-1).
- 3 DOF: give information about the three components of strength. This can be forces, torques or a combination of both. A joystick to play flight games is an example.
- 6 DOF: in addition to providing information about the forces, the sensor gives also the torques. These are the most useful, but also the most complicated and therefore the most expensive ones.



Figure 2-1. Load cell  
(<http://www.coventryscale.co.uk/>)

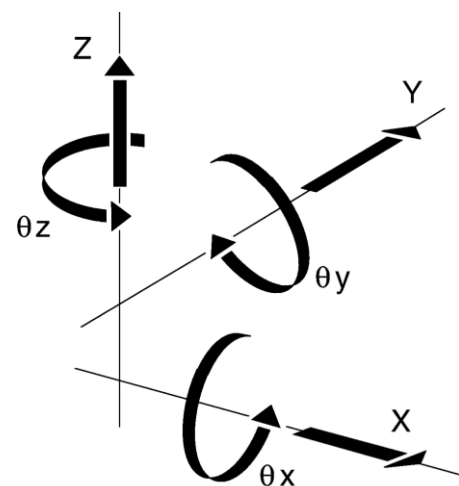


Figure 2-2. Degrees of freedom

## 2.2. Technology used

Any technology that can detect a change in its characteristics or its position when a force is applied can be used as a force sensor. Resistive elements and magnetic or optical sensors are some of the most used.

### 2.2.1. Resistive

The type of sensor most used is based on resistive sensors (also known as strain gauges). These are formed by metal rods with a certain degree of elasticity due to mechanical stress. On these bars are bonded strain gauges that measure the deformation. The impedance variation due to deformation is proportional (linearly or not) to force or torque exerted on them. A strain gauge uses the physical property of electrical conductance and its dependence on the conductor's geometry (figure 2-3).

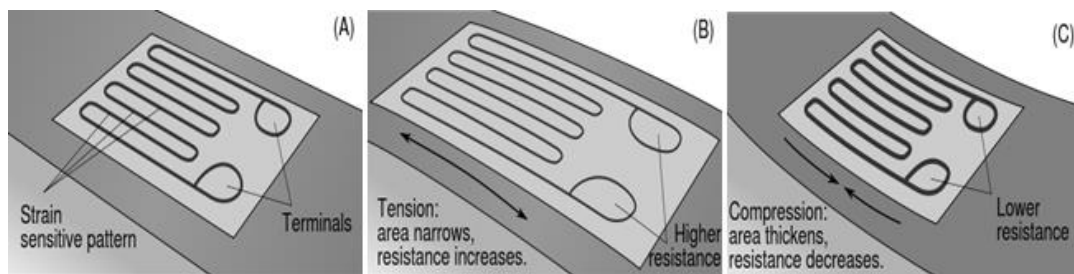


Figure 2-3. Electrical conductance

Resistance  $R$  in a conductor is defined as:

$$R = \rho \frac{\ell}{A}$$

Where:

$\rho$  is the electrical resistivity of the material, measured in ohm-metres ( $\Omega \cdot m$ ),

$\ell$  is the length measured in meters, and

$A$  is the cross-sectional area of the conductor measured in square metres [ $m^2$ ]

When an electrical conductor is stretched within the limits of its elasticity such that it does not break or permanently deform, it will become narrower and longer, changes that increase its electrical resistance end-to-end. Conversely, when a conductor is compressed such that it does not buckle, it will broaden and shorten, changes that decrease its electrical resistance end-to-end. Metals (normally aluminium in force sensors) are the materials used, because they have a linear relationship between deformation and strength.

The most common type of strain gauge consists of an insulating flexible backing which supports a metallic foil pattern. Normally it measures forces in one direction, but some kind of strain gauges, can detect in more than one direction, even omnidirectionally. The gauge is attached to the object by a suitable adhesive, such as cyanoacrylate. As the object is deformed, the foil is deformed, causing its electrical resistance to change. This resistance change, usually measured using a Wheatstone bridge, is related to the strain by the quantity known as the gauge factor.

The gauge factor  $GF$  is defined as:

$$GF = \frac{\Delta R / R_g}{\varepsilon}$$

Where:

$\Delta R$  is the change in resistance caused by strain,

$R_g$  is the resistance of the undeformed gauge, and

$\varepsilon$  is the strain.

Other ones uses a flat coil of a piezo-resistive material. Its operating principle is based on the change in resistance of the piezo-resistive material when they are subjected to mechanical stress; in this case the compression appears when interacting with another surface. These have a larger gauge factor than a foil gauge. Semiconductor gauges tend to be more expensive, more sensitive to temperature changes, and more fragile than foil gauges [2].

The main disadvantage presented by these sensors is that gauges vary their impedance when they are subjected to mechanical stress but they are also sensitive to changes in temperature. The temperature variation causes a variation of the resistivity of the gauge material, which varies the reading of the sensor when no force on the sensor. To minimize the error due to variation of temperature gauges, two other strain gauges are placed where they are only affected by the temperature. Thus, the deformation due to the applied force does not affect the second gauges. Although any change in temperature will affect both gauges alike. Consequently the output voltage of the bridge Wheatstone does not change because the relationship between the two resistors remains the same.

In this prototype, this kind of sensing elements will be used; therefore they will be explained more extendedly.



### 2.2.2. Magnetic

The Hall Effect magnetic sensors are used to measure the variation of the electromagnetic field. The variation is caused by the difference in position or distance between the magnetic field and the Hall Effect sensor; in consequence, a change in output voltage will be registered (figure 2-4). These kinds of sensors are formed by at least six pairs of sensor-magnet if 6DOF are wanted.

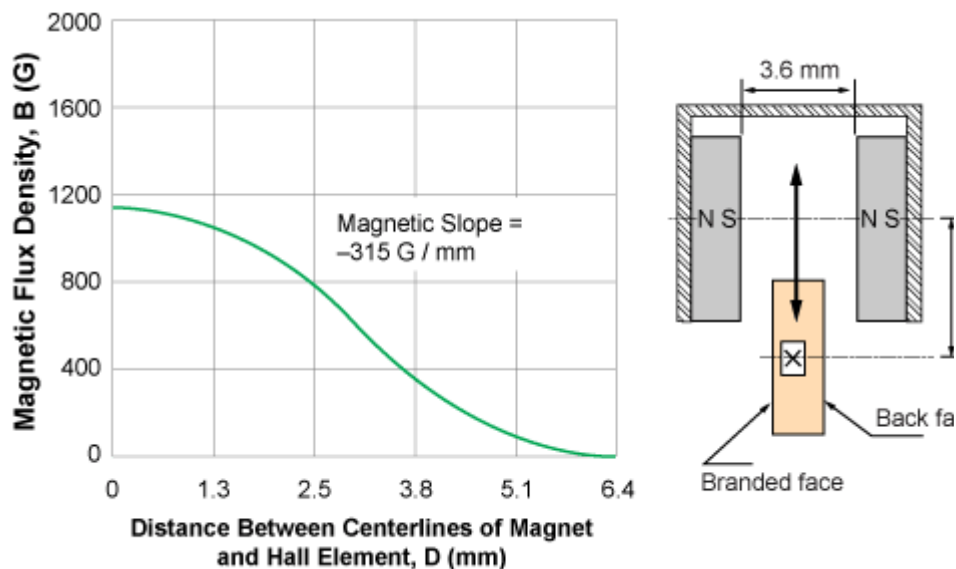


Figure 2-4. Example of magnetic flux characteristic in push-pull slide-by magnet configuration (<http://www.allegromicro.com/>)

The Hall effect is the production of a voltage difference (the Hall voltage) across an electrical conductor, transverse to an electric current in the conductor and a magnetic field perpendicular to the current.

It is based on the principle of Lorentz force acting on a charged particle moving through a magnetic field, defined as:

$$F = q[E + (v \times B)]$$

Where:

F is the force,

q is the charge of the particle,

E is the electric field,

v is the velocity of the particle, and

B is the magnetic field.

If the equation is set to zero, after some changes is possible to obtain the Hall Effect as:

$$R_H = \frac{E_y}{j_x B_f}$$

Where:

$R_H$  is the Hall coefficient,

$E_y$  is the electric field along the y axis,

$B_f$  is the magnetic field,

$j_x$  is the current density of the carrier electrons along the x axis.

Some applications of these sensors are in the automotive industry, e.g. the closure of the seatbelt system, door locks or acknowledgment of the position or the pedal. Its great advantage in this sector is the immunity from dirt (non-magnetic) and water. Other applications are in integrated circuits, laser printers, disk drives in computers and brushless DC motors.

### 2.2.3. Optic

Another family of force sensors is based on the use of optical technology. These devices are immune to EMI and can work in harsh chemical and radioactive environments. They have a compact size and light weight. Different kinds of operation principles are used, and some of them are described below.

#### Angle of incidence

The principle of operation of these types of sensors is based on a plastic sheet that acts as a light guide. The light is introduced with the angle of incidence needed to cause total reflection at one end of the sheet, propagating through this to the other end. This physical principle is based on Snell's law, defined as:

$$n_1 \sin \theta_1 = n_2 \sin \theta_2$$

Where:

$n$  are the indices of refraction, and

$\theta$  are the angles of incidence and refraction.

The light guided via a light-guide was incident upon one end of the plate. The light is conducted within the plate by total internal reflection if no pressure is applied on the external elastic sheet. Pressure applied onto the sheet causes an optically active contact between the sheet and the plate. Thus the total internal reflection

conditions are changed and the light illuminates the sheet. The sheet scatters the light back in the area of the pressure and the patterns of the pressure area can be observed by a phototransistor array [2] (figure 2-5).

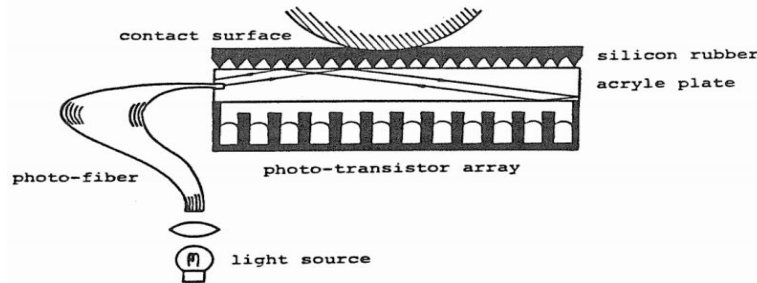


Figure 2-5. Example of an angle of incidence sensor [1]

## Optical fibres

Various methods to detect pressure using optical fibres are known. Wang et al. proposed a pressure sensor that employs the effect of photoelasticity [3].

Urban et al. designed a pressure sensor that relies on Fibre Bragg Grating lateral deformation [4]

This method is based on the deflection of the light in polymer fibre waveguides. Applying a force on the fibre changes the geometry and affects the wave guiding properties and hence induces light loss in the optical fibre (figure 2-6).

The loss of light  $A$  is defined as:

$$A = 10 \cdot \log_{10} \left( \frac{I}{I_0} \right)$$

Where:

$I$  is the intensity of the transmitted light and

$I_0$  is the initial light intensity.

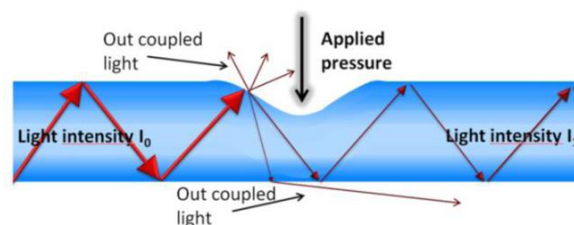


Figure 2-6. Loss of light in a fibre under compression [24]

The detected signal loss can vary from 0.5% to 80%. The fibres have attenuation parameters between 0.16–0.25 dB/cm at 652 nm.

## Fiber Bragg Grating (FBG)

One new type of fiber sensor is the fiber Bragg grating (FBG) sensor or tuned laser. FBG is a portion of optical fiber whose refractive index has periodical changes along its length. It works as a partially reflecting mirror with a narrow ( $<0.2$  nm) spectral peak. The wavelength band passed is determined by the grating period (figure 2-7).

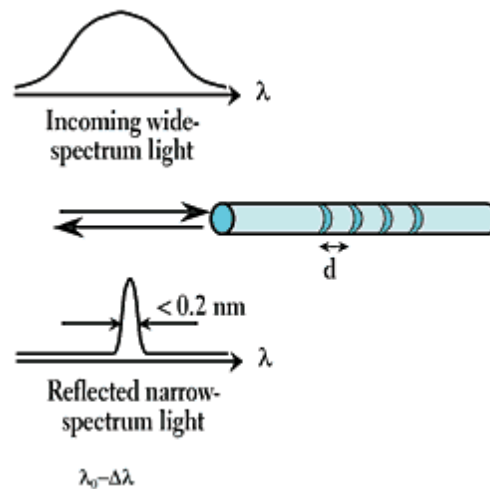


Figure 2-7. Wavelength filtered

Under longitudinal strain, both the period and the peak reflectivity wavelength change. Under tension, the peak wavelength shifts toward longer wavelengths; under compression, it shifts toward shorter wavelengths (figure 2-8).

This wavelength shift depends linearly on strain with a coefficient of  $\sim 1.2$  pm/ $\mu\epsilon$ . Similarly, the wavelength changes with temperature at a rate of 1.3 pm/ $^{\circ}\text{C}$ .

To detect such changes in the peak wavelength, we must either measure the light intensity in a very narrow spectral window, or have a light source with a stable wavelength and narrow line width. In the former case, the input signal can be a broad-spectrum light source, such as superluminescent LEDs, with a narrow optical filter at the detector side whose wavelength is close to the centre of an unstrained FBG's reflectivity peak. In the latter case, the input source can be lasers with stabilized wavelengths, such as temperature-stabilized semiconductor distributed feedback (DFB) lasers or fiber lasers. FBG sensors can measure strain or temperature at the grating's location. For measurements at multiple points (e.g., strain in buildings, bridges, or airplane wings), multiple fibers with FBG sensors must be installed [5].

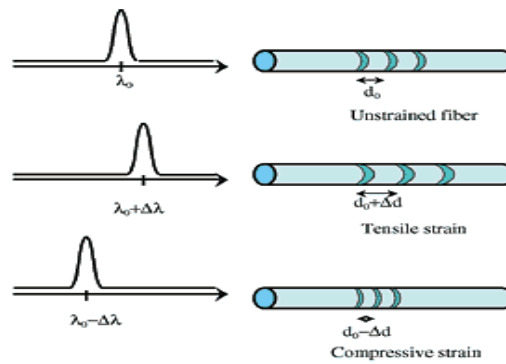


Figure 2-8. Change of  $\lambda$  under tensile stress

The comparison of main features and characterization methods using a selection of multi-dimensional F/T sensors up to the date of the publication are shown in Table 2.1 [6].

Year & Developer	Technology	Size (mm) & n° axes	Sensitivity & Measurement range	Sensing element
1998 & Jin and Mote [7]	Bulk silicon micromachining and wafer-bonding technologies	4.5x4.5x1.2 & 6	1mN (force) and 2mN (moment) & n.a.	Piezoresistive
1999 & Mei et al. [8]	CMOS process, silicon bulk micromachining	4x4x2 & 3	13mV/N in Z-axis and about 2.3mv/N in X- and Z-axis & 0—50 N in Z-axis, ±10N in X and Y axis	Piezoresistive
2012 & Brookhuis, Lammerink [9]	Bulk silicon Micromachining & silicon fusion bonding	9x9x1 (PCB chip) & 3	16 PF/N in Fz and 2.7PF/N mm in Mx and My & 50N in Fz, ±25 N mm in Mx and My	Capacitive
2009 & Takenawa, S. [10]	Four chip inductors, silicone gel, and a neodymium magnet	3.2x2.5 x 2.2 & 3	0.06 N (resolution) & -40 N to 40 N	Inductive
2011 & M. Gobbi et al. [11]	Three spoke structure, standard mechanical machining	40.25x16 x 16 & 6	95% (uncertainty) & 10 kN (Fz), 5 kN (Fx, Fy) and 0.5 kNm (M)	Strain gauge
2004 & Liu, Inoue et al. [12]	Parallel support mechanism & machining	170x105x26.5 & 6	Fx=Fy=20kgf, Fz=100kgf, and Mx=My=Mz=100 Nm	Strain gauge
1990 & Hirose and Yoneda [13]	Three elastomers in a flexed spoke shape & milling and electric discharge machining	Φ76x40 & 6	0.3% & 100 kgf and 300kgfcm for parallel and rotating directions, respectively	Optical
2010 & Jia, Lin, and Liu [14]	Stewart platform & standard mechanical machining	small than Φ160 x 210	linear error and the repeatability error of 1% & 40kN and 5kNm for force and moment	Piezoelectric

Table 2 - Comparisons on the multi-dimensional F/T sensor

## 2.3. Mechanical frame

In order to detect three orthogonal forces and three orthogonal torques at the same time, force sensors are always featured by complicated geometrical structures, which make accurate calculation of strains and deflection difficult or even impossible with current techniques.

Historically, a major problem in developing force sensors is the design of the force-sensing element, which has been done heuristically, dependent on the experience of designers. Nowadays complete finite element simulation software are developed to simulate mechanical efforts. SolidWorks, ProEngineer, CATIA, Autodesk Fusion 360 are some of them.

A critical drawback of the traditional multi-component F/T sensor is the existence of significant measurement couplings among components, especially between component  $M_x$  and component  $F_y$ , component  $M_y$  and component  $F_x$ .

Force causes stresses and displacements of the objects upon it acts. If displacements are blocked, only stresses occur when a force vector is applied on a deformable body. By measuring these stresses, one can obtain the necessary information to determine the acting force. Direct stress measurements are difficult to proceed, they must be evaluated using measurable parameters, such as strain, that vary in response to loading. Many force transducers employ simple elastic elements (monoblock) or combination of elements (e.g. pillars, beams, rings) in assembled constructions. Force application on such a flexible element produces a deflection in this first transducer, which is then measured by a secondary transducer (e.g. strain gauge or LVDT) and converted into a measurable output (i.e. electronic unbalance of a Wheatstone bridge). [15]

Some of the most used are classical columns, classical tubes, cantilever beams and middle bent bars with fixed ends.

### 2.3.1. Classical columns

This is the simplest shape, but also the less sensible. (figure 2-9)

Load Range [N]:  $10 \dots 10^7$

Mechanical sensitivity [ $\mu\text{m}/\text{m}$ ]:  $\frac{F}{E * a * e}$

Where E is the Young's Module,

F the force and,

a and e dimensions.

Electrical sensitivity [ $\varepsilon$ ]: 2.6

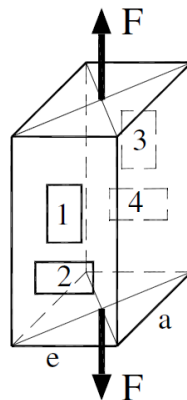


Figure 2-9. Compressed column

Single column load cells are tall and heavy if they are designed for very high loads. Low profile packages can be obtained if the load is divided by three or more columns, each column with its own set of strain gauges. The corresponding gauges from all of the columns are connected in series in Wheatstone bridge. The result is not only a lower profile, but also an improved performance when the cell is off-center or off-axis loaded. Compression type load cells don't suffer from the momentum typically associated with beams, so the deflection measured will be only depend on the weight supported. The relatively small deflection makes these load cell types more sensitive to shock loading, but it is possible to increase the sensitivity, drilling holes near the strain gauges. This produces a longer deformation in the measured area.

### 2.3.2. Classical tubes

This is a variation of the classical column. The idea is to decrease the material under force, therefore increasing the deformation, and making the load cell more sensitive. (figure 2-10)

Load Range [N]: 10..10<sup>6</sup>

Mechanical sensitivity [ $\mu\text{m}/\text{m}$ ]:  $\frac{4 * F}{\pi * E * (D^2 - d^2)}$

Where E is the Young's Module,

F the force and,

D external diameter and

d internal diameter.

Electrical sensitivity [ $\varepsilon$ ]: 2.6



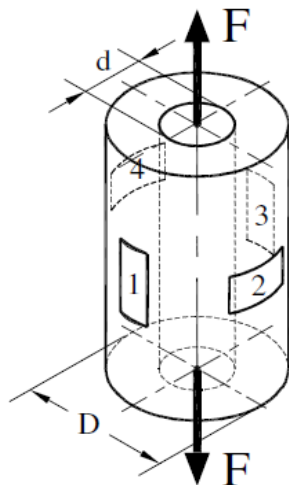


Figure 2-10. Compressed tube

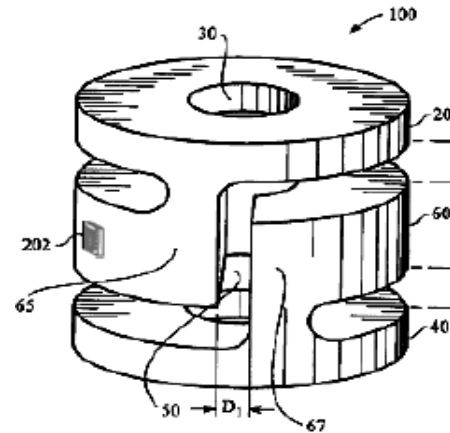


Figure 2-11. Helical load cell

This kind of frame allows a wide range of dimensions depending on the available materials and it is easy to process. The tube is less sensitive to bending, twisting and buckling than the column because can be wider than the column for the same load.

The sensitivity can be increased in many ways. Drilling holes, combinations of two concentric tubes, double tubes having slightly different heights (for different ranges), or helical cuts. (figure 2-11)

### 2.3.3. Cantilever Beams

The cantilever beam has low rigidity, high deflection and it is recommended for low forces, because can be uses from pico- to kilo-newtons, depending on the material and dimensions of the beam. (figure 2-12)

Load Range [N]:  $10^{-2} \dots 10^7$

Mechanical sensitivity [ $\mu\text{m}/\text{m}$ ]:  $\frac{6 * F * l}{E * a * h^2}$

Where E is the Young's Module,

F the force and,

l, h and a are dimensions.

Electrical sensitivity [ $\varepsilon$ ]: 4

Circular or rectangular slotted configurations can be drilled providing increased sensitivity and internal strain uniformity.

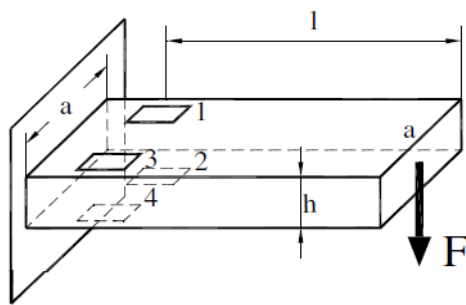


Figure 2-12. Cantilever beam

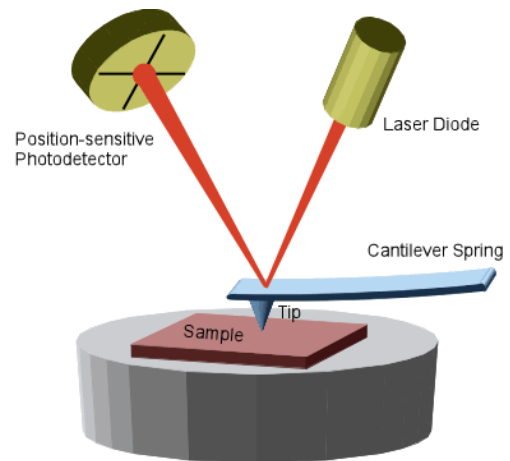


Figure 2-13. Contact mode AFM (<http://www.physik.uni-greifswald.de/>)

Despite cantilever beams have many applications in the high forces range, the main applications are in the field of micro- and nano-Newton. In particular, the called “contact mode Atomic Force Microscope (AFM)”.

The tip of a microcantilever is in contact with the surface. As the surface undulates, the cantilever bends depending on the surface. The cantilever deflection is measured by the reflection of a laser beam, in a four-quadrant photodiode. (figure 2-13)

The beam is centred onto the photodiode. Proportional, Integral and Derivative (PID) control is used to maintain the spot centred while the tip scans across a sample by adjusting the height of the frame where the cantilever is mounted.

#### 2.3.4. Middle bent bars with fixed ends.

This frame is by far the most used in 6DOF force sensors because is easy to build, mainly the four arms frame, also called “Maltese cross”.

Load Range [N]:  $10 \dots 10^4$

Mechanical sensitivity [ $\mu\text{m}/\text{m}$ ]: 
$$\frac{1.5 * F * (2l - L)}{E * a * h^2}$$

Where E is the Young’s Module,

F the force and,

l, L, h and a are dimensions.

Electrical sensitivity [ $\varepsilon$ ]: 4

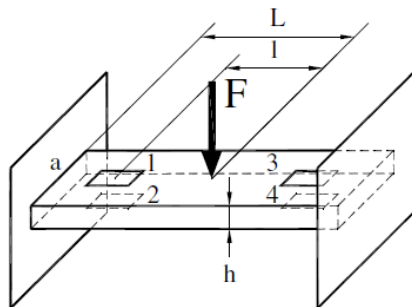


Figure 2-14. Middle bent bars with fixed ends

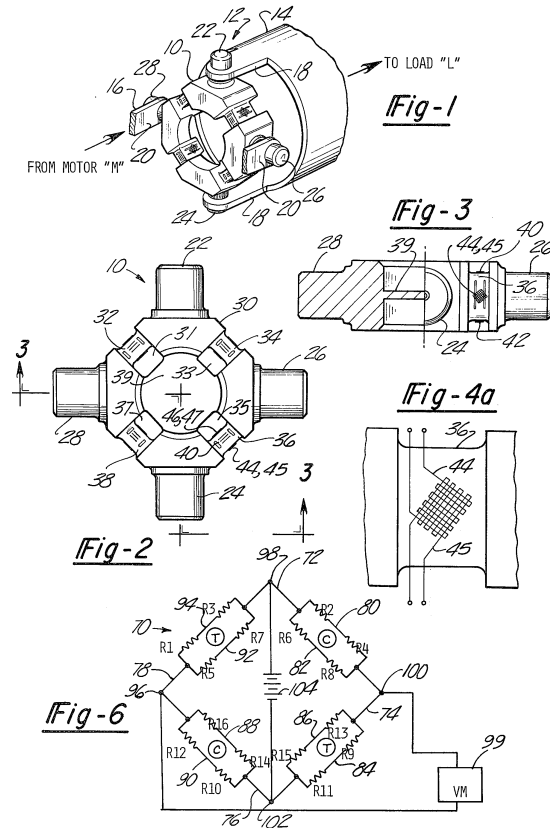


Figure 2-15. Patent US3956930 A

Because the maximum measurable moment  $M$  is too small when compared with the maximum measurable force  $F$ , beams are not symmetrical. (figure 2-14)

In 1974, Ralph S. Shoberg patented a first version of cross-bar type six-axis force sensor [16] with the number US3956930 A (figure 2-15).

In 1975, Watson and Drake presented a six-axis force sensor composed of two rings and three columns to connect them. In 1977, a six-axis force sensor having eight compliant beams was developed at SRI International. Hirzinger et al. designed and developed a control system with a six-axis force sensor mounted on a robot and a sensor ball mounted on the fixed surface for manual manipulation. Hirose and Yoneda developed the six-axis force sensor using the photo sensors with high sensitivity and reproducibility. Since the beginning of the 1980's, several types of six-axis force sensors have been commercially produced by several companies, e.g., Assurance Technologies Inc., Nitta Co., BL-Autotech Co. Recently, Assurance Technologies Inc. developing the mini six-axis force sensor provided in ultra-small packages with a diameter of approximately 15 mm.

This kind of frame has been chosen for this project.

### 2.3.5. Others

There are also other kinds of frames, like the used for a 7DOF (3 DOF for translation, 3 DOF for rotation, and 1 DOF for grasp), made by Seahak Kim, Shoichi Hasegawa, Yasuharu Koike, and Makoto Sato. This model works by sensing the tension of 8 cables in a cube structure [17]. (figure 2-16)

The Stewart Platform, originally proposed for a flight simulator has been suggested for a wide variety of applications, for example a six component force–torque sensor. Dasgupta et al. [18] proposed a Stewart Platform in an isotropic configuration where the sensor is equally sensitive to all directions of applied force–torque. In a Stewart Platform manipulator, the arms are connected to the fixed base and moving platform by universal and spherical joints respectively. In a sensor application, the forces experienced by the arms due to the application of the external load needs to be measured (sensed) as accurately as possible. Typically, the force in the arm is measured in the form of strain and a strain sensing element such as strain gage or LVDT are used.

Stewart Platform can be made of MEMS, and are used for very small applications as force sensors integrated in surgical elements. (figure 2-17)

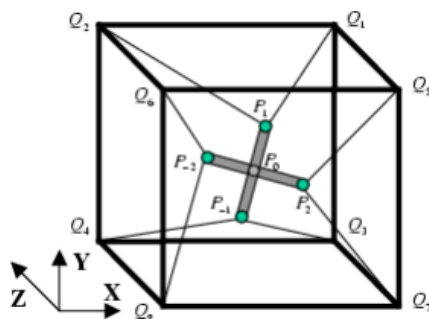


Figure 2-17. Basic structure of SPIDAR-G

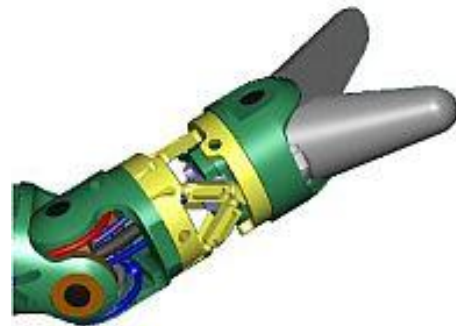


Figure 2-16. Stewart Platform in a surgical tool (in yellow).  
(<http://www.robotic.dlr.de/>)

### 3. Mechanical design

#### 3.1. Introduction

The mechanical work of this project starts with the selection of the type of frame will have the sensor. After this, some work of design and simulation is needed in order to choose the best option for the specifications needed in the measurements.

Post processing is the interface between the design and the process of milling in a CNC machining. Milling simulation is necessary to check if the CNC mill can do all orders programed.

The mechanical work will be finished after the milling of the prototype.

The complete work diagram can be seen below. (figure 3-1)

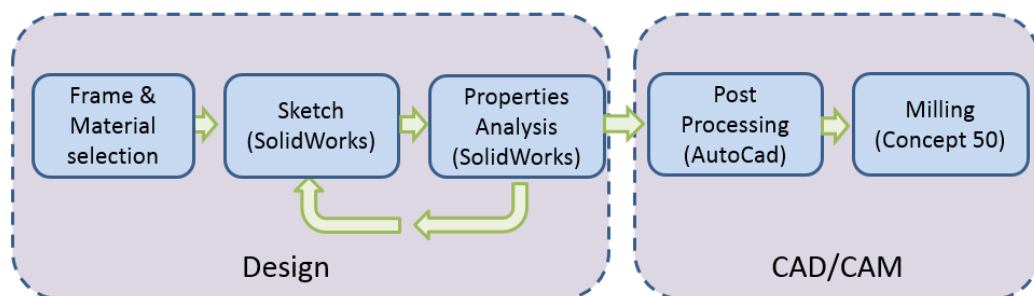


Figure 3-1. Mechanical work diagram

#### 3.2. Frame & Material selection

As it is said before, the design chosen is middle bent bars with fixed ends (figure 3-2). One reason is because is affordable to build, it needs only four strain gauges per arm plus two strain gauges more as a reference. Another reason is because its manufacture is compatible with a basic 3-axis milling tool like the CNC mill we have in ESAII department.

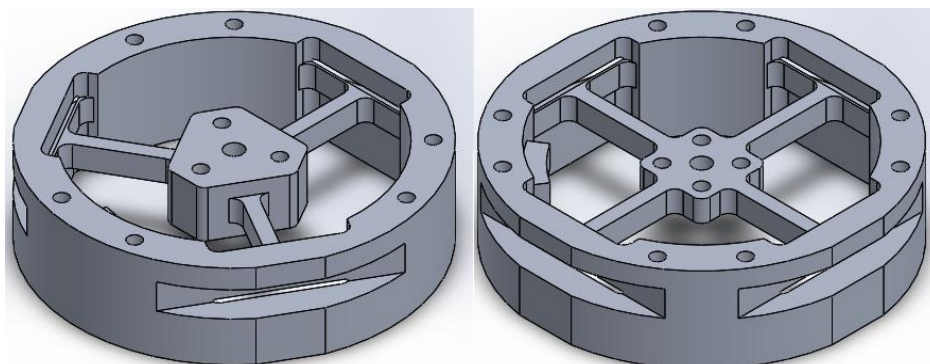


Figure 3-2. Three and four arms middle bent bars with fixed ends frame

There are two options of this type of frame, three or four arms. Advantages and disadvantages are shown in table 3.1.2.1.

	Three legs	Four legs
Economy	Cheaper due to having four strain gauges less	More expensive because it must have more electronic components
Milling	Faster to mill	Slower
Accuracy	More difficult because it have less signals	Redundancy of signals making the final result more significant
Endurance	Less points have to support forces and torques	More supports means more stability
Matrix calculation	Easier and faster to calculate	Slower because it has more elements
Calibration	More difficult to apply forces	Easier because the frame is symmetrical

Table 3 - Advantages and disadvantages of different models

The frame chosen is the one with four arms, also called Maltese cross, mainly because of the redundancy of signals.

This make the matrix of calculus bigger and difficult to work, but on the other hand, the force and torque calculated will be much more accurate.

The material chosen for this work, is the Aluminium alloy 5083. This is a non-heat-treatable 4,5% magnesium alloy (table 4). Like all the 5000-series high magnesium alloys 5083 it achieves a high strength by cold working, and this is important because the force sensor must be elastic, but it must not be warped easily.

Alloy	Si	Fe	Cu	Mn	Mg	Cr	Zn	Ti	Others
5083	0.4%	0.4%	0.1%	0.4 - 1%	4 - 4.9%	0.05- 0.025%	0.25%	0.15%	0.05- 0.15%

Table 4 - Aluminium alloy 5083 Composition

Another reason to choose this alloy, is because its corrosion resistance is excellent in a wide range of atmospheric environments. In fact, it is widely used for ship building.

But at the other hand, machinability of 5083 alloy is poor due to its high strength. Best machinable Aluminium are series 2000 and 6000, but series 5083 have a machinability of 30% in Aluminium Alloys Scale. It means that the mill speed will not be very high, but this is not important in a prototype.

### 3.3. Sketch

There are three mechanical restrictions for the mechanical frame. First, the external dimensions. By now, an ATI Gamma force sensor is used in ESAII laboratory, so the idea is not to have to change nothing at all about the experiments and projects we have. If is possible to make a prototype with the same dimensions, it will be very easy to change the ATI model for the new one.

The second restriction is the forces and torques it can measure. Using analysis and simulation, geometric dimensions of the sensor could be adjusted, and therefore the model will have the specifications needd.

The last restriction, is that the sensor must have a survival load similar to the ATI Gamma.

It is important to keep in mind the way to mill the prototype. Only a 2.5 Axis mill can be used, and 2, 4 and 8 mm in diameter mill drills can be used. Also a T-sharp of 25mm in diameter can be used.

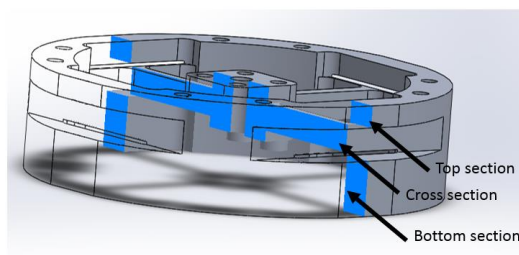


Figure 3-3. Sensor sections

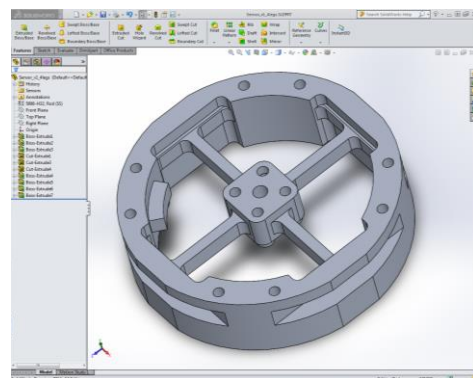


Figure 3-4. SolidWorks 2014

The sketch work is done with the solid modelling computer-aided design (CAD) and computer-aided engineering (CAE) software program called SolidWorks 2014 (figure 3-4)

The sensor is done by three sections (figure 3-3). First section or bottom one (figure 3-6), is the one that will be in contact with the robot. This means that their walls must be thick enough to not flex under forces applied.

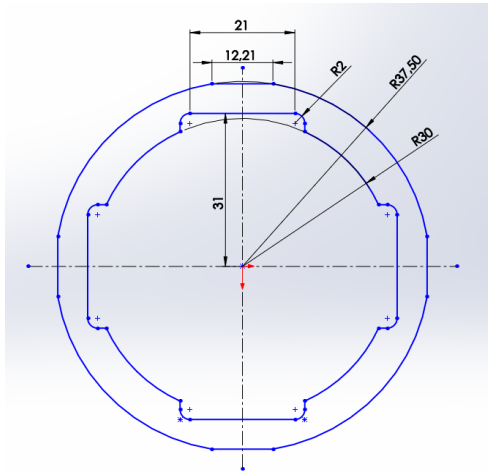


Figure 3-6. Bottom section

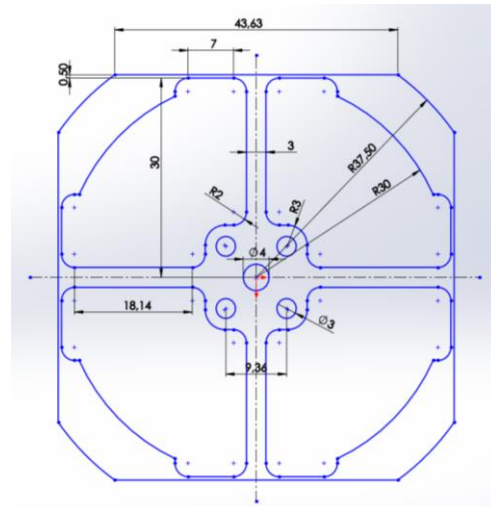


Figure 3-5. Middle section

The total thick of the sensor will be of 20 mm, so this part is extruded with 10mm to ensure that the PCB will have enough space.

The cross section or middle one (figure 3-5), is the one that have the bending arms. Once again, they are symmetrical in four quadrants.

Arms are fixed in the centre part of the sensor, but the other extreme must be as possible as a cantilever. This means that it must be flexible to ensure that the arm is flexed by the force applied. The thick of this part is very critical, if it is very thick, the arm will no flex enough to be measured by the strain gauge. On the other hand, if is too thin, the arm will be too much weak. Different measurements will be simulated in order to obtain the best relationship Signal/Strength.

This section will be extruded with 5 mm, because is the minimal dimension of the mill that we have.

The top layer is exactly the same that the bottom one, but extruded only 4 mm.

Eight holes will be drilled in the external walls in order to fix the sensor to the robot (figure 3-8), four holes will be drilled in the centre part of the sensor to allow to fix an end-effector element. This will be the one that transmits the forces to the sensor.

A centre hole is drilled to allow the calibration process, because a symmetrical force must be applied in both parts of the sensor as will be seen in calibration process.

A fixed support element to glue the reference strain gauges will be milled in the external walls. This must be thick enough to ensure that the reference strain gauges will not move at all. Only temperature displacement will be allowed in this strain gauges. In Dynamic Simulation it will be seen if this element will not flex under external force.



In back part of the sensor holes, a 2 mm spacer will be milled to create a separation between the sensor and the PCB, but at the same time, to have ground contact between them (figure 3-7).

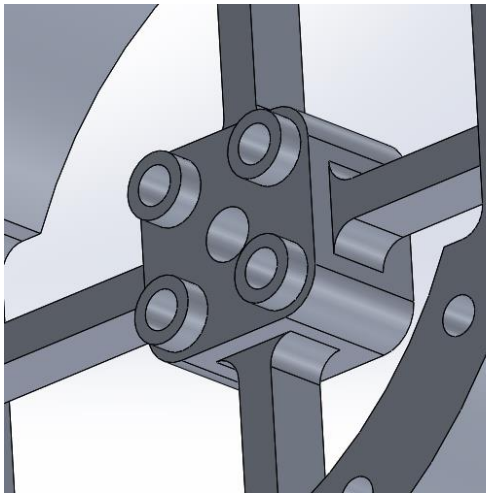


Figure 3-7. Spacer between sensor and PCB

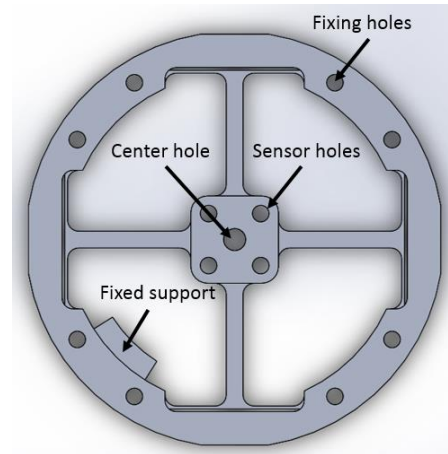


Figure 3-8. Holes and fixed support element

SolidWorks software allows a material Thickness Analysis (table 6). This reveals that the wall between fixings holes and external wall is only 0.748mm (figure 3-9), when angle between holes are 25°. This is not recommended because there are areas sensitive to cracks. After changing the angle dimension to 20°, wall thickness is increased to 1.6mm (figure 3-10).

### Summary

Total surface area analyzed	17436,63 mm <sup>2</sup>
Critical surface area(% of analyzed area)	15699,81 mm <sup>2</sup> (90,04%)
Maximum deviation from target thickness	5,50mm
Average weighted thickness on critical area	2,68mm
Average weighted thickness on analyzed area	2,75mm
Number of critical faces	138 Face(s)
Number of critical features	10
Minimum thickness on analyzed area	0,01mm
Maximum thickness on analyzed area	7,95mm

Table 5 - Thickness Analysis



Figure 3-9. Thick analysis for 25° between fixing holes

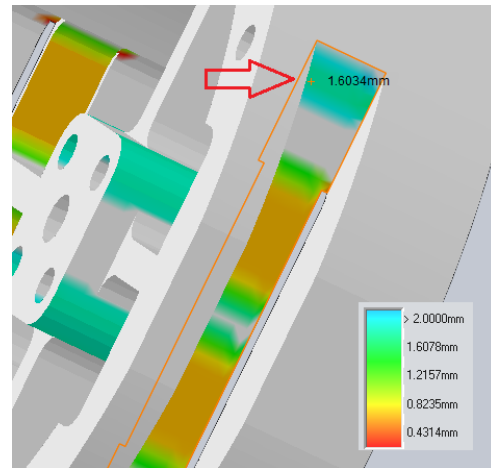


Figure 3-10. Thick analysis for 20° between fixing holes

Another problem revealed with the thickness analysis, is the thickness in compliant beams (figure 3-11). This cannot be fixed because is intrinsic of this frame, but it warns us to have a special care when frame is milled.

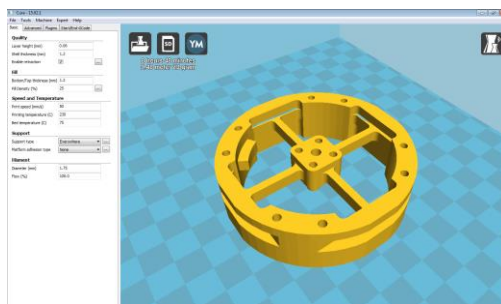


Figure 3-12. Cura Software

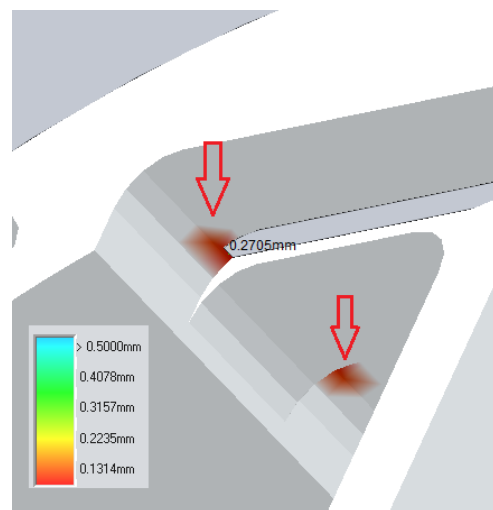


Figure 3-11. Thickness in compliant beams

After the sketch and analysis, the model is post-processed with Cura software (figure 3-12), and then printed with a Prusa i3 printer (figure 3-13).

This is recommended in order to check if all mill tools are compatible with the frame designed.

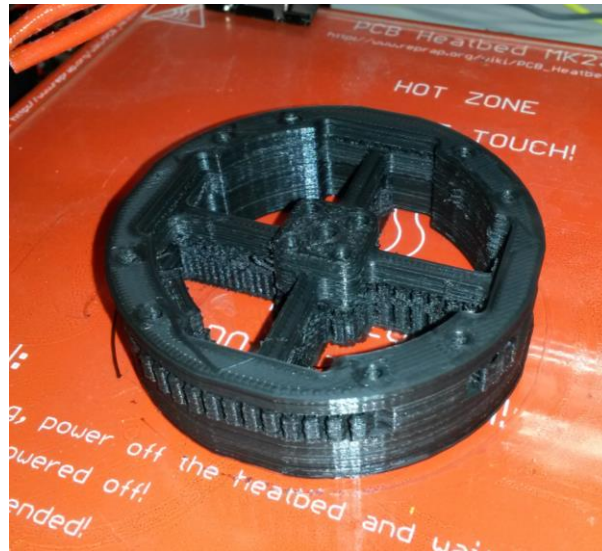


Figure 3-13. 3D plastic model

### 3.4. **Dynamic Simulation**

Dynamic Simulation is done by different reasons:

Mechanical – establishing the optimum measuring range and overall dimensions for universal application of this new one-piece solution. This gives an idea of the elastic elements behaviour under forces applied.

Numerical – iterative FEM computation (2D analysis by ANSYS program based on Plane42 finite elements) for choosing the best axisymmetrical profile, to increase the measurement sensitivity. This allows to change measures and test, until we have the appropriate dimensions to obtain the best displacement/noise as is said before.

Electrical – designing special strain gauges and choosing their optimal positions on the elastic body (tangential versus longitudinal) and Wheatstone bridge connections to improve the measurement accuracy and other metrological characteristics. It is very important to define these paths in the same conditions for all variants of axisymmetrical elastic elements.

The precise numerical computation of maximum stress and maximum displacement having in view the design criteria fulfilment is also of great importance.

In the partial view of the sensor (figure 3-15), it is possible to see four cross elastic beams (i.e., AB, CD, EF, GH) and eight compliant beams (i.e., AQ, AI, HL, HM, DJ, DK, EP, EN).

Parameters  $l_1$ ,  $b_1$ ,  $h_1$  (figure 3-14) are length, width and height of compliant beams, and parameters  $l_2$ ,  $b_2$ ,  $h_2$  are the length, width and height of cross elastic beams, respectively. In most cases,  $b_2$  is half to  $h_2$ .

External forces/torques are applied on the centre square and transmitted to cross elastic beams, that will be deformed.

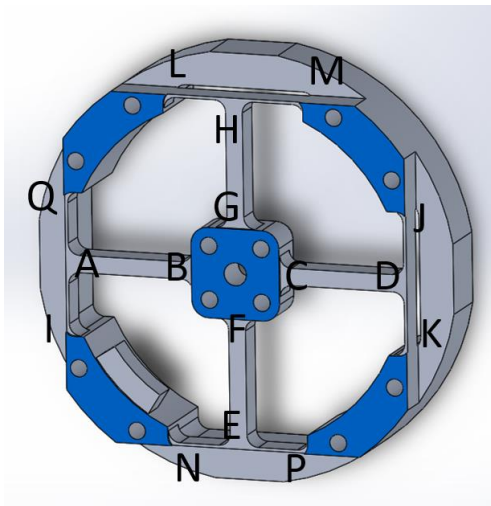


Figure 3-15. Beam sections

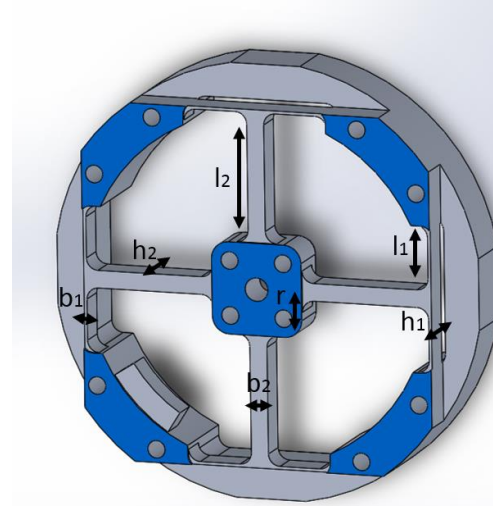


Figure 3-14. Parameters

Compliant beams, which are flexible to external forces/torques too, can be regarded as floating beams. Other parts of the sensor are assumed to be rigid.

Because of the symmetry of the sensor, the deformation under  $F_x$  is similar to  $F_y$ , and the deformation under  $M_x$  is similar to  $M_y$ . As a result, only deformation analysis of the sensor under  $F_x$ ,  $F_z$ ,  $M_x$ ,  $M_z$  will be modelled and simulated.

### 3.4.1. Model Development

The deflection distance of cantilever beam under a load, is directly related to the slope of the deflected shape of the arm under that load and can be calculated by integrating the function that mathematically describes the slope of the arm under that load.

Deflection can be calculated by standard formula:

$$y = \frac{Wx^2}{6EI}(3l - x) \quad (1)$$

Where:

$y$  is the deflection at specified point,

$W$  is the load,

$x$  is the distance between the force point and the fixed point,  
 $E$  is the Young's modulus and  
 $l$  is the beam's longitude.

Stress at specific point can be calculated with:

$$s = \frac{W}{Z}(l - x) \quad (2)$$

Where:

$s$  is the stress and

$Z$  is section modulus of the cross-section of the beam.

These formulas work if it is a pure cantilever, but in this case, the beams have not a floating but a semi floating end. Cross-beams elastic bodies are statically indetermined structures. The responses of cross-beams elastic bodies under forces/torques in different directions involve various complex interactions between cross elastic beams and compliant beams. Deflection characteristics of the above flexural beams under different dimensional forces/torques are analysed by Timoshenko beam theory [19]. It says any cross-section of the beam is treated as an undeformable body that does not allow any displacement other than rigid ones [20].

Thus, the deformation characteristics of the beam are described by two variables, i.e., the translational displacement ( $w$ ) of any cross-section and the angular displacement ( $\psi$ ) of any cross-section, as is expressed in Equation (3).

$$\begin{cases} M_{(x)} = -EI \frac{d\psi(x)}{dx} \\ F_{Q(x)} = kGA \left( \frac{d\omega(x)}{dx} - \psi(x) \right) \end{cases} \quad (3)$$

Where  $x$  denotes the  $x$ -coordinate value of any point in the beam as is shown in figure 3-16 (it also indicates the distance of the point away from the beginning of the beam),  $M$  is the bending moment and  $FQ$  is the shear force,  $A$  represents the cross-sectional area,  $E$ ,  $I$ ,  $k$ ,  $G$  are the elastic modulus, second area moment, shear coefficient and shear modulus, respectively.

If force/torque equations are in equilibrium for the infinitesimal section:

$$\begin{cases} \frac{d}{dx} \left[ C \left( \frac{d\omega(x)}{dx} - \psi(x) \right) \right] = 0 \\ \frac{d}{dx} \left( D \frac{d\psi(x)}{dx} \right) - C \left( \frac{d\omega(x)}{dx} - \psi(x) \right) = 0 \end{cases} \quad (4)$$

Where:

$C = kGA$  and

$D = EI$ .

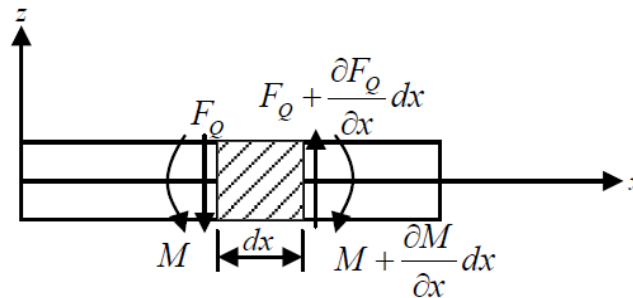


Figure 3-16. Infinitesimal section of a Timoshenko beam

Equation (3) and Equation (4) are two basic formulas of Timoshenko beam theory, from which analytical solutions of  $w(x)$  and  $\psi(x)$  could be calculated when enough boundary conditions are given.

Once the analytical solution of angular displacement  $\psi(x)$  is obtained, the strain value ( $\epsilon$ ) any point in the beam can be calculated in Equation (5).

$$\epsilon(x, z) = -z \frac{d\psi(x)}{dx} \tag{5}$$

Where  $z$  is  $z$ -coordinate value at any point in the beam and it also indicates the distance between the point and the neural plane.

### Model under Fx

If  $F_x$  is applied (figure 3-17), bending occurs on cross elastic beams EF, GH and compliant beams AQ, AI, DJ, DK. Compliant beams HL and HM, EN and EP become two elastic supports of beams EF and GH.

In mechanical model (figure 3-18), node notation with primes (e.g. A') are displaced position respect the original one (e.g. A). Compliant beams HL and HM, EN and EP are simplified as roller supports H and E. Other conjunctions we assume that are rigid joints. Cross elastic beams EF, GH are idealized as cantilever beams and compliant beams AQ, AI, DJ and DK are idealized as cantilever beams. In addition, it can be easily noticed that axial forces are transmitted through cross elastic beams AB and CD. Beams AB and CD we assume also that are rigid bodies, because deformation for compression and tension are negligible compared with bending deformation.

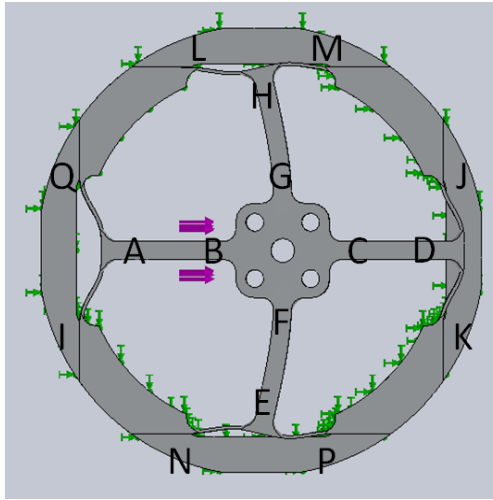


Figure 3-17. Frame deformation under  $F_x$  (force in purple arrows, fixed face in green)

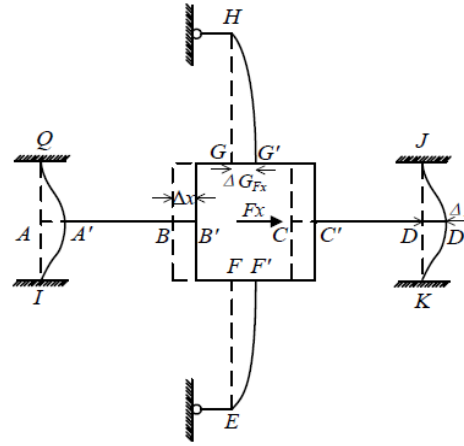


Figure 3-18. Mechanical model under  $F_x$

From equation (4) and observed conditions of beam HG we can obtain:

$$\Delta G_{F_x} = \frac{l_2^3 F_{GF_x}}{3E \left( \frac{b_2 h_2^3}{12} \right)} + \frac{l_2 F_{GF_x}}{kG(b_2 h_2)} \quad (6)$$

Where:

$F_{GF_x}$  is the shear force on cross elastic beam GH.

Deriving equation (4) and observed conditions of beam DJ we can obtain:

$$\Delta D_{F_x} = \frac{l_1^3 F_{DF_x}}{12E \left( \frac{h_1 b_1^3}{12} \right)} + \frac{l_1 F_{DF_x}}{kG(b_1 h_1)} \quad (7)$$

Because the geometric shape of the frame:

$$\Delta x = \Delta G_{F_x} = \Delta D_{F_x} \quad (8)$$

The equation of forces in equilibrium of the square centre is derived as:

$$4F_{DF_x} + 2F_{GF_x} = F_x \quad (9)$$

From Equation (4) and (9), we obtain the strain value at any point on GH beam:

$$\varepsilon_{F_x}(x, z) = -z \left( \frac{F_{GF_x}}{D_2} x - \frac{l_2 F_{GF_x}}{D_2} \right) \quad (10)$$

Where:

$$F_{GFx} = \frac{\frac{l_1^3}{12E \frac{h_1 b_1^3}{12}} + \frac{l_1}{kG b_1 h_1}}{2 \left( \frac{l_1^3}{12E \frac{h_1 b_1^3}{12}} + \frac{l_1}{kG b_1 h_1} \right) + \left( 4 \frac{l_2^3}{3E \frac{h_2 b_2^3}{12}} + \frac{l_2}{kG b_2 h_2} \right)} Fx \tag{11}$$

**Model under Fz**

If Fz is applied (figure 3-19), bending occurs on all four cross elastic beams and compliant beams. All cross elastic beams are simplified as propped-cantilever beams and all compliant beams are simplified as fixed beams.

Δz means the displacement of the square centre (figure 3-20), ΔFz is the displacement of node H in compliant beam HM.

Because the symmetry of the frame, only will be derived equations for beam GH and compliant beam HM.

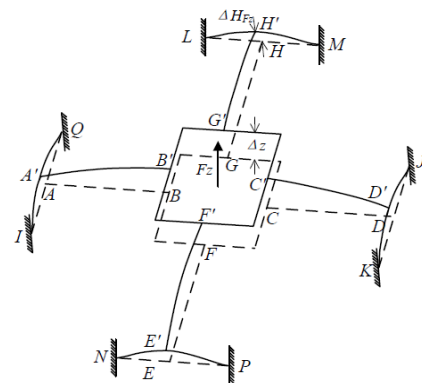
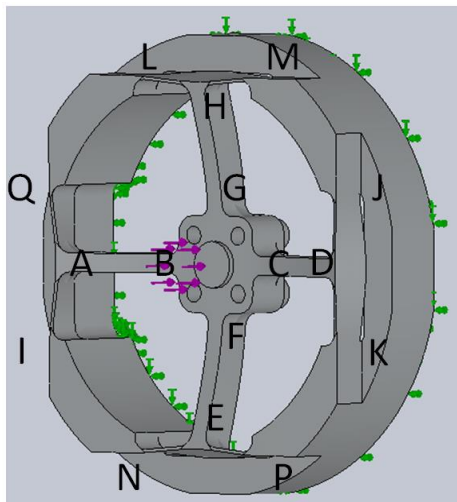


Figure 3-19. Frame deformation under Fz (force in purple arrows, fixed face in green)

Figure 3-20. Mechanical model under Fz

ΔGFz is the displacement distance of the centre square under Fz, and it can be derivate from Equation (4), and boundary conditions of GH beam:

$$\Delta G_{Fz} = - \left( \frac{l_2^3}{3E \left( \frac{b_2 h_2^3}{12} \right)} + \frac{l_2}{kG (b_2 h_2)} \right) F_{GFz} \tag{12}$$



Where:

$F_{GFz}$  is the shear force in GH beam.

From Equation (4) beam HM displacement can also be derived also:

$$\Delta H_{Fz} = - \left( \frac{l_1^3}{12E \frac{b_1 h_1^3}{12}} + \frac{l_1}{kG b_1 h_1} \right) F_{HFz} \quad (13)$$

The equations of forces in equilibrium of the square centre is derived as:

$$Fz = -4F_{GFz} = -8F_{HFz} \quad (14)$$

Displacement of square centre will be:

$$\Delta z = \Delta G_{Fz} + \Delta H_{Fz} \quad (15)$$

And displacement  $\varepsilon_{Fz}$  can be calculated from Equations (4), (5), (13) and (15):

$$\varepsilon_{Fz}(x, z) = -z \left( \frac{Fz}{4E \left( \frac{b_2 h_2^3}{12} \right)} x - \frac{l_2 Fz}{4E \left( \frac{b_2 h_2^3}{12} \right)} \right) \quad (16)$$

### Model under Mx

The deformation of the cross-beams under Mx (figure 3-22), bending deformations occur on beams EF and GH. Torsional deformations occur on beams AB and CD.

Therefore very small rotations and translations in compliant beams AQ and AI, DJ and DK, will be idealized as two fixed supports for beams AB and CD, respectively. Also compliant beams HL and HM, EN and EP are idealized as beams with fixed supports. Consequently, beams EF and GH, nodes H and E can be simplified as roller supports.

Notation  $\Delta\Theta_{Mx}$  (figure 3-21) describes the angle of rotation of the centre with respect x-axis, and  $\Delta H_{Mx}$  describes the displacement of H. Bending beam EF is the same as the case of beam GH, the bending of beam HM is the same as beams HL, EP, EN.

The torsion of beam AB is the same as the torsion of beam CD. Only deformation conditions of beams AB, GH and HM will be considered.

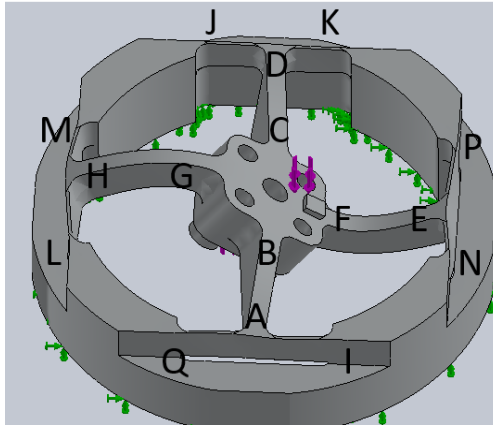


Figure 3-21. Frame deformation under  $M_x$  (force in purple arrows, fixed face in green)

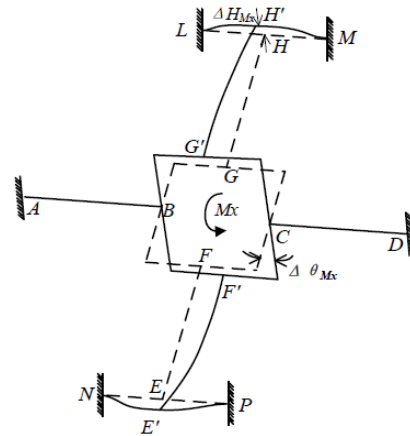


Figure 3-22. Mechanical model under  $M_x$

Torsion angle  $\alpha$  of AB beam can be obtained [21] from:

$$\alpha = \frac{M_{BMx} l_2}{GIt} \quad (17)$$

Where:

$M_{BMx}$  is the torque applied on AB. It is given by the expression:

$$I_t = \beta b^2 h^2$$

and  $\beta$  is the coefficient for rectangular beams that depends on  $b/h$  ratio (table 6) [22].

b/h	1	2	2.5	3	4	5	6	10	$\infty$
$\beta$	0.141	0.229	0.249	0.263	0.281	0.291	0.299	0.312	0.333

Table 6 -  $\beta$  coefficient vs.  $b/h$  ratio

$\Delta r_{Mx}$  can be calculated from Equation (4), obtained from deformed characteristics of beams GH and HM:

$$\Delta r_{Mx} = \frac{3kGb_2h_2E \frac{b_2h_2^3}{12} \Delta H_{Mx} - kGb_2h_2F_{GMx}l_2^3 - 3E \frac{b_2h_2^3}{12} F_{GMx}l_2}{3kGb_2h_2E \frac{b_2h_2^3}{12} (l_2 + r)} \quad (18)$$

Where:

$$\Delta H_{Mz} = -F_{GMx} \left( \frac{l_1^3}{12E \frac{b_1 h_1^3}{12}} + \frac{l_1}{kGb_1 h_1} \right) \text{ and,}$$

$F_{GMx}$  is the force on GH

Deformation of  $Mx$  is:

$$\Delta \theta_{Mx} = \Delta r Mx = \alpha \quad (19)$$

And force/torque equations of equilibrium are:

$$2M_{BMx} + 2M_{GMx} - 2F_{GMx}r = Mx \quad (20)$$

Where:

$M_{GMx}$  is the bending moment on surface top of beam GH, and

$$F_{GMx} = \frac{M_{GMx}}{l_2}$$

Combining Equations (4), (5) and (17) to (20), the strain value of any point on GH beam can be found:

$$\varepsilon Mx(x, z) = -z \left( \frac{F_{MGx}}{E \frac{b_2 h_2^3}{12}} x + \frac{l_2 F_{GMx}}{E \frac{b_2 h_2^3}{12}} \right) \quad (21)$$

$F_{GMx}$  can be obtained from:

$$F_{GMx} = \frac{-3kGb_2 h_2 E \frac{b_2 h_2^3}{12} l_2 (l_2 + r) Mx}{W} \quad (22)$$

Where:

$$W = 3kGb_2 h_2 E \frac{b_2 h_2^3}{12} \left[ 2l_2 (l_2 + r)^2 + Gl \left( \frac{l_1^3}{12E \frac{b_1 h_1^3}{12}} + \frac{l_1}{kGb_1 h_1} \right) \right] + 2Gl \left( kGb_2 h_2 l_2 + 3E \frac{b_2 h_2^3}{12} l_2 \right) \quad (23)$$

### Model under $M_z$

Bending deformations happen on all beams when a  $M_z$  is applied (figure 3-24).

Compliant beams AQ and AI, DJ and DK, EN and EP, HL and HM become four elastic supports of beams AB, CD, EF, GH, respectively. CD beam is taken by example. The right end of beam CD is free to rotate and move along x-axis, but small translations along y-axis. Taking into consideration the strong reaction force perpendicular to beam CD, the reaction moment and force of D along cross beam CD could be ignored.

Hence, the four elastic supports can be simplified as four roller supports, i.e., nodes A, D, E and H in the proposed mechanical model of the elastic body under  $M_z$ . (figure 3-23)

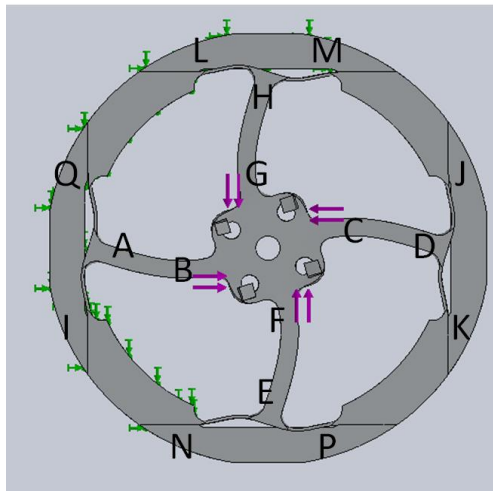


Figure 3-24. Frame deformation under  $M_z$  (force in purple arrows, fixed face in green)

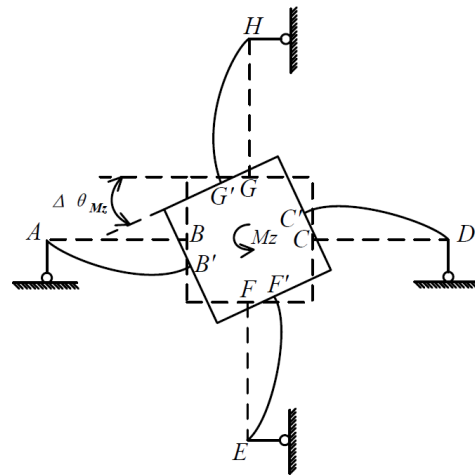


Figure 3-23. Mechanical model under  $M_z$

As a result, four cross elastic beams are idealized as simple cantilever beams. The notation  $\Delta\theta_{M_z}$  is the angle of rotation of the square convex with respect to z-axis in the global coordinate under  $M_z$ .

The force/torque equation in equilibrium under  $M_z$  is:

$$-4F_{GM_z}r - 4M_{GM_z} = M_z \quad (24)$$

Where:

$F_{GM_z}$  is the shear force, and

$M_{GM_z}$  is the bending moment ( $M_{GM_z} = F_{GM_z}l_2$ ).

From Equation (4) and (242):

$$\Delta\theta_{M_z} = \frac{l_2^3 k G b_2 h_2 + 3E \frac{b_2 h_2^3}{12} l_2}{12 k G b_2 h_2 E \frac{b_2 h_2^3}{12} (r + l_2)^2} M_z \quad (23)$$

Then strain distribution over GH can be derived as:

$$\varepsilon_{M_z}(x, z) = -z \left( -\frac{M_z}{4r + 4l_2} - \frac{l_2 - \frac{M_z}{4r + 4l_2}}{E \frac{b_2 h_2^3}{12}} x + \frac{l_2 - \frac{M_z}{4r + 4l_2}}{E \frac{b_2 h_2^3}{12}} \right) \quad (24)$$

### 3.4.2. ANSYS Simulation

Dynamic simulations are necessary to determine the best parameters for the axisymmetrical sections. Each degree of freedom of a node in a finite element mesh constitutes an unknown. In structural analysis, nodal degrees of freedom represent displacement components. Simulations give the influence of different parameters on strain gauge sensitivity, on all sides of the measuring section. A lot of interpretations are possible based on this multitude of data:

- Influence of the axisymmetrical elastic element shape (varying different parameters) on the strain gauge sensitivity.
- Influence of thickness  $h$  of the two connection beams.
- Best combination of conflicting design criteria: strain, stress to determine overload and displacement to determine stiffness.
- Possible correlation between the nominal load and the dimensions of a particular variant, e.g. with square measuring section.
- Optimum strain gauge emplacement solution for a chosen model of axisymmetrical elastic element.

Therefore, there are many parameters to calculate. Square section in beams is a particular case of the rectangle one and offers a multitude of dimensioning possibilities, because of its combined vertical and horizontal influences. For this reason, the dynamic simulation will be used to be sure that strain gauges are at optimal position.

A special attention is necessary to obtain proper strain diagrams on the superior, lateral and inferior sides of the elastic element measuring section, because it is essential to compare these diagrams in order to establish the best strain gauges positioning.

The precise numerical computation of maximum stress and maximum displacement having in view the design criteria fulfilment is also of great importance.

- If a greater strain gauge sensitivity is preferred, then the measuring section is placed horizontally.
- If a smaller displacement is preferred, then the rectangular measuring section is placed vertically.

Increasing progressively the dimensions is possible to increase the applied load.

To resolve dilemma sensitivity vs. stiffness a negotiation of behavior restrictions is necessary. Of course, first priority is the maximum strain at the nominal load. For deciding between strength (maximum stress) and stiffness (minimum displacement) constraints, two new and very different research directions are envisaged, as follows:

Minimum displacement ( $< 0.3$  mm) for axisymmetrical elastic structures is ensured by tubes, but their strain gauge sensitivity is reduced, due to Poisson's coefficient for two of them. The best way to improve their tensometrical sensitivity (up to 25 %) is to "transform" tension / compression in bending after profiling the section.

Maximum admissible stress is supported by complex elastic structures subjected to very large forces (up to 10 MN) if they have pairs of deeper slots with larger radii, inspired by genetic algorithms. Such configurations are obtained starting from very flexible structures, like membranes or N-shaped elastic elements, and strengthening them by vertical ribs, respectively, thickening their sides, so that the displacement is also reduced. [23]

A general procedure for finite element analysis of the force transducers elastic elements do not exist. Designers are working based on their experience and intuition in this multi- and inter-disciplinary field. In this project an standard Finite Elements Analysis (FEA) procedure for axisymmetrical elastic elements of strain gauged force transducers using Solidworks program.

Here two commonly used failure criteria: Von Mises Stress failure Criterion and Maximum Normal stress Criterion are given.

Von Mises stress, also known as Huber stress, is a measure that accounts for all six stress components of a general 3-D state of stress. (figure 3-25)

Von Mises stress  $\sigma_{\text{VonMises}}$ , can be expressed either by six stress components as:

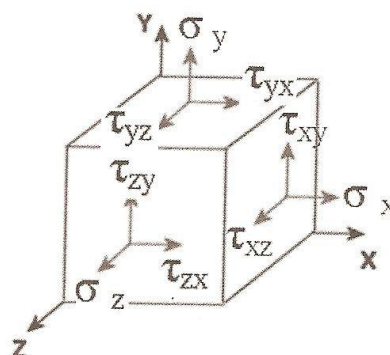


Figure 3-25. Stress in a 3D solid

$$\begin{aligned}\sigma_{VonMises} &= \sqrt{0.5 * [(\sigma_x - \sigma_y)^2 + (\sigma_y - \sigma_z)^2 + (\sigma_z - \sigma_x)^2] + 3(\tau_{xy}^2 + \tau_{yz}^2 + \tau_{zx}^2)} \approx \\ &\approx \sqrt{0.5 * [(\sigma_x - \sigma_y)^2 + (\sigma_y - \sigma_z)^2 + (\sigma_z - \sigma_x)^2]}\end{aligned}\tag{25}$$

As can be seen, von Mises stress is a non-negative, scalar stress measure. Von Mises stress is commonly used to present results because the structural safety for many engineering materials showing elasto-plastic properties can be evaluated.

The maximum von Mises stress failure criterion is based on the von Mises-Hencky theory, also known as the scalar-energy theory or the maximum distortion energy theory. The theory states that a ductile material starts to yield at a location when the von Mises stress becomes equal to the stress limit. In most cases, the yield strength is used as the stress limit.

This criterion predicts failure will occur when  $\sigma$  exceeds the stress limit, usually the ultimate tensile strength. According to the maximum principle stress failure criterion,

the factor of safety (FOS) is expressed as:  $\frac{\sigma_{limit}}{\sigma_{VonMises}}$ .

Where  $\sigma_{limit}$  is the yield strength.

By properly adjusting the angular orientation of the stress cube, shear stresses disappear and the state of stress is represented only by three principal stresses:  $\sigma_1, \sigma_2, \sigma_3$ .

The Maximum Normal Stress Failure criterion is used for brittle materials. Brittle materials do not have a specific yield point. This criterion assumes that the ultimate tensile strength of the material in tension and compression is the same. This assumption is not valid in all cases.

For example, cracks considerably decrease the strength of material in tension while their effect is not significant in compression because the cracks tend to close. (figure 3-26)

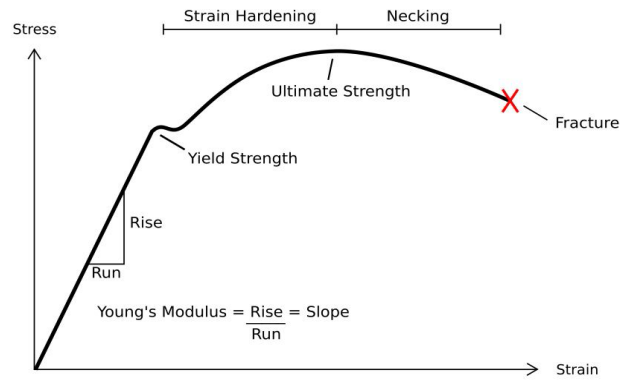


Figure 3-26. Strain vs. Stress

For large and complicated shapes, SolidWorks creates a solid mesh of 13281 elements, where the 91.9% of the elements are smaller than 3mm, in order to do the calculation easier. (figure 3-27)

Full Dynamic Simulation can be seen in APENDIX A.

Next step is to give material properties to the simulator. Parameters of table 8 can be used for Aluminium alloy 5083.

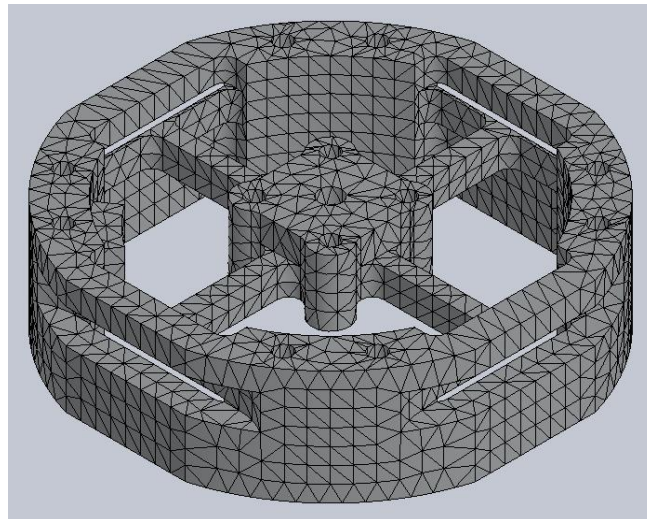


Figure 3-27. Solid mesh of the frame structure



Properties	Data in Metrics	Comments
Density	2.66 g/cm <sup>3</sup>	
Brinell's Hardness	85	500 kg load with 10 mm ball. Calculated value
Ultimate Tensile Strength	317 MPa	
Tensile Yield Strength	228 MPa	
Elongation at Break	16 %	
Modulus of Elasticity	70.3 GPa	In Tension
Compressive Modulus	71.7 GPa	Average of tension and compression.
Poisson's Ratio	0.33	
Fatigue Strength	159 MPa	

Table 7 - Aluminium alloy 5083 Properties (The Aluminum Association, Inc.)

### Simulation under Fx and Fy

As the frame is symmetrical, the same deformation occurs if a force is applied in X axis as in Y axis. Bending occurs only in the beams perpendicular to the force applied as expected. In this case, the force will be applied in X axis.

For a value of force simulated of 10N under Fx, the displacement simulation reveals that maximum displacement of the frame is of 8.96e-3 mm. (figure 3-28)

Von Mises Stress simulation shows that maximum stress is 13 MPa in compliant beams perpendicular to the force applied (figure 3-28). Also it reveals the best position for the strain gauges on beams for Fx and Fy sensing.

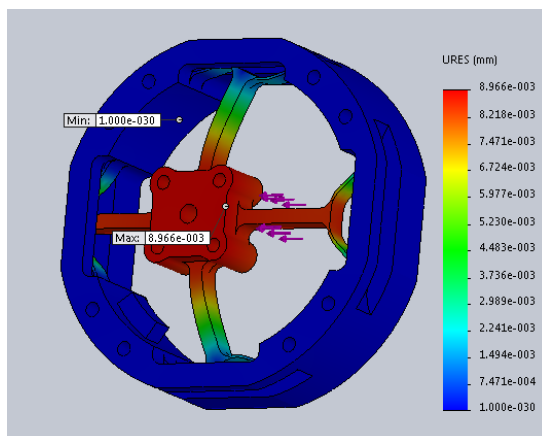


Figure 3-29. Displacement simulation under Fx (Deformation scale: 803)

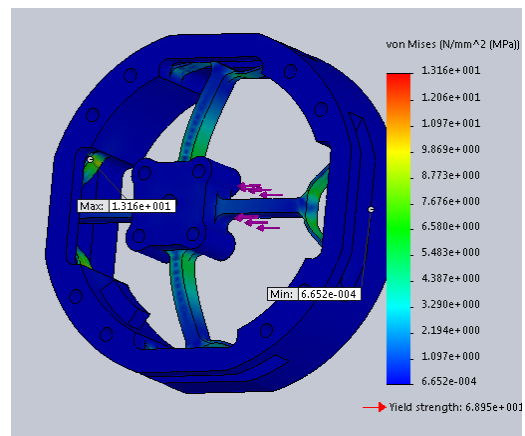


Figure 3-28. Von Mises Stress simulation under Fx (Deformation scale: 803)

First dangerous stress (FOS) appears when a force of 75N is applied (figure 3-29), much higher than specifications required.

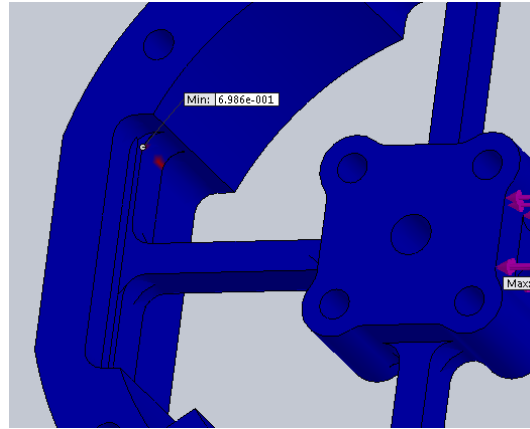


Figure 3-30. Safety factor stress test

### Simulation under Fz

If Fz is applied, bending occurs on all four cross elastic beams and compliant beams as was expected.

The value of force simulated is 10N under Fz.

Displacement simulation reveals that maximum displacement of the frame is of  $4.8e-5$  mm (figure 3-31). Much smaller than in Fx case. This is because the asymmetrical shape of the beams, and because force is applied over the four beams.

Von Mises Stress simulation shows that maximum stress is 4.6 MPa (figure 3-32) Also it reveals the best position for the strain gauges on beams for Fz sensing.

First dangerous stress appears when a force of 175N is applied (figure 3-33), much higher than specifications required.

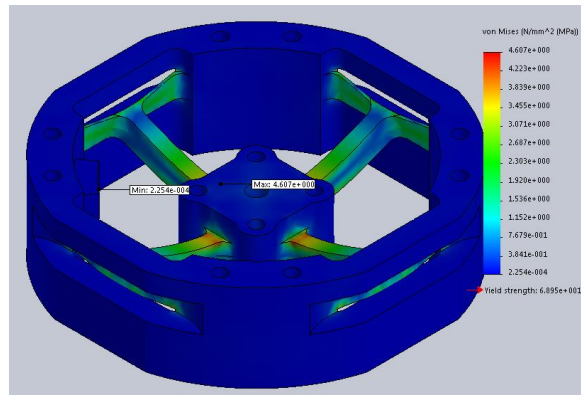


Figure 3-31 Von Mises Stress simulation under Fz (Deformation scale: 1487.28)

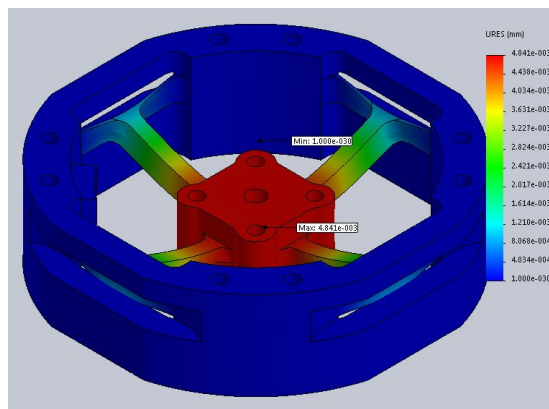


Figure 3-31. Displacement simulation under Fz (Deformation scale: 1487.28)

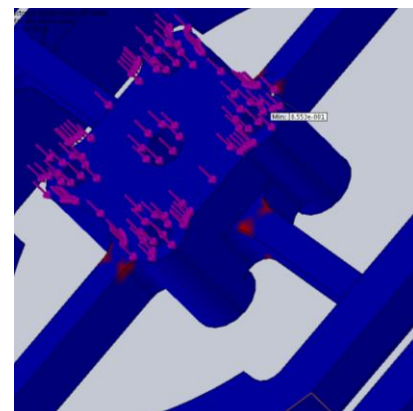


Figure 3-33. Safety factor stress test

### Simulation under Mx and My

As the frame is symmetrical, the same deformation occurs if a moment is applied in X axis as in Y axis. Bending occurs only in the beams in line of the moment applied, and torsion occurs in bendings perpendicular to the moment as expected. In this case, the moment will be applied in X axis. A little modification has been done to the frame, in order to apply two forces to create the moment.

The total value of force simulated is 10N on central cube.

Displacement simulation reveals that maximum displacement of the frame is of  $9.45e-4$  mm (figure 3-34).

Von Mises Stress simulation shows that maximum stress is 2.07 MPa (figure 3-35). Also it reveals the best position for the strain gauges on beams for Mx and My sensing.

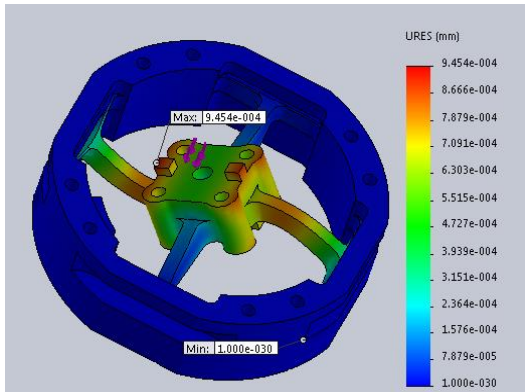


Figure 3-34. Displacement simulation under Mx (Deformation scale: 8799)

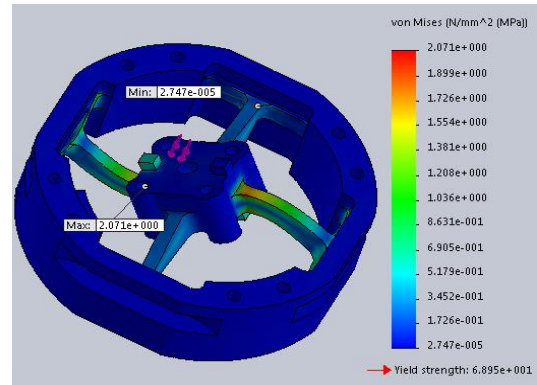


Figure 3-35 Von Mises Stress simulation under Mx (Deformation scale: 8799)

### Simulation under Mz

Bending occurs in the four beams. A little modification has been done to the frame, in order to apply two forces to create the moment. The total value of force simulated is 10N on central cube.

Displacement simulation reveals that maximum displacement of the frame is of 9.5e-4mm (figure 3-36).

Von Mises Stress simulation shows that maximum stress is 1.6 MPa (figure 3-37) Also reveals the best position for the strain gauges on beams for Mz sensing.

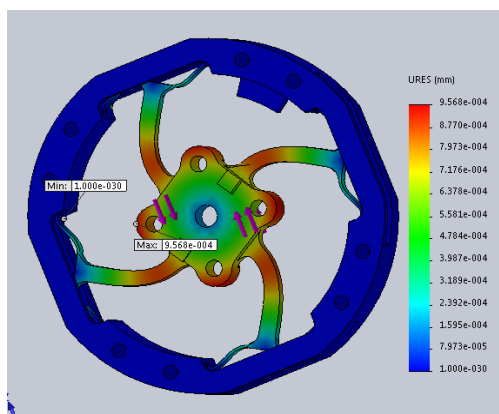


Figure 3-36. Displacement simulation under Mz (Deformation scale: 8130.3)

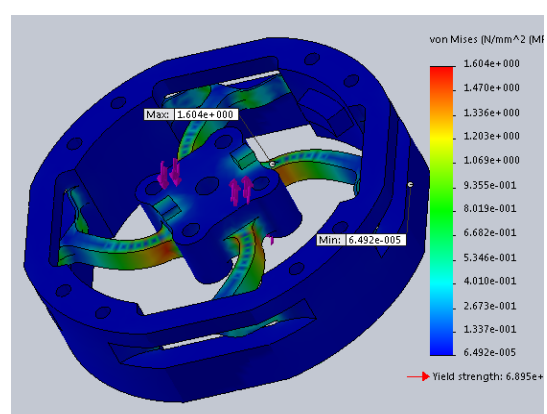


Figure 3-37. Von Mises Stress simulation under Mz (Deformation scale: 8130.3)

### 3.5. Post Process

After dynamic simulation, the frame must be programmed in G code in order to the machining mill processing. In the first part of this process, a SolidWorks plugin in evaluation period has been used (figure 3-38).

Once the pockets are defined, this plugin calculates the necessary paths, in function of the mills we have.

In this case, a flat of 8mm, 4mm, a centre drill and a 20mm T shape mill.

It is also possible to run a simulation of the milling process.

Every different mill tool has at least one program, because the mill we are going to use have not automatic change of tool.

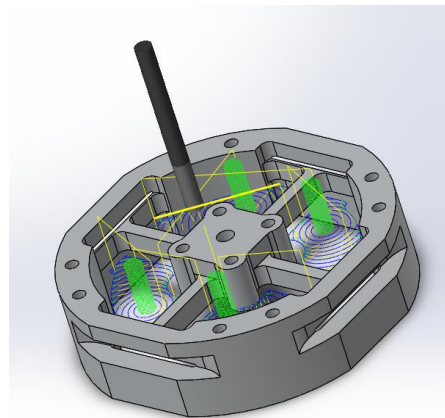


Figure 3-38. SolidWorks CAM  
Post Process

In table 8, it can be seen the different programs used for this project. All these programs can be seen in APPENDIX B.

Program Name	Mill tool type	Program description
%200	Centre drill	Defines the position of drills - Face A
%201	2.7mm drill	M3 threat holes - Face A
%202	6 mm drill	Positioners holes - Face A
%203	8mm flat mill	Interior roughing - Face A
%204	8mm flat mill	Exterior roughing - Face A
%205	T-shape mill	Side slot mill - Face A
%206	4mm flat mill	Finishing mill - Face A
%300	Centre drill	Face B
%301	2.7mm drill	Face B
%302		

Table 8 - Program descriptions

The frame must be milled from both sides, then, a second part of the post process must be done to calculate the position of the frame positioners. This part has been done with AutoCAD software. (figure 3-39)

General G code must be tested in the mill machine, because every machine have its own commands. In this case it is a Siemens Sinumerik 820 model. (figures 3-40 and 3-41)

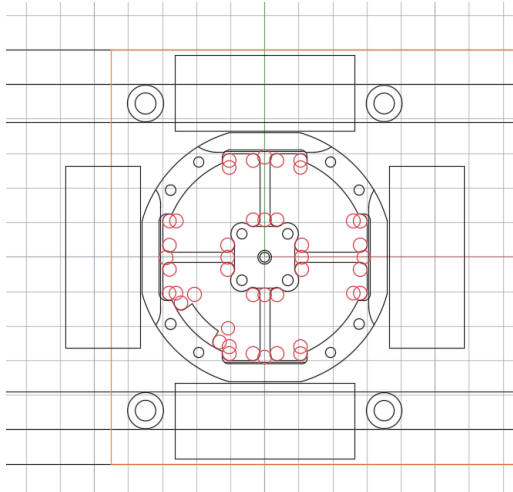


Figure 3-39. AutoCAD Post Process



Figure 3-40. Sinumerik 820 Program

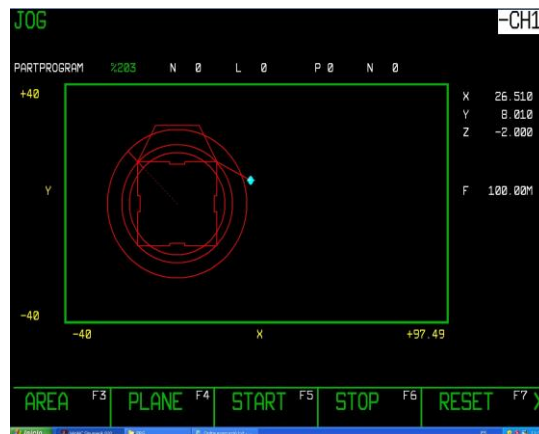


Figure 3-41. Sinumerik 820 Simulation

### 3.6. Milling

The mill used is the educational model EMCO ConceptMill 55 (figure 3-42).

The frame is made out of a solid block of aluminium, and the first program to run is the one that uses the centre drill (figure 3-43) to position where the drills will make the holes (figure 3-44).

There are three different diameter drills in this side of the frame. The smallest one of 2.4 mm will be used to thread the PCB over the frame. Six holes of 6mm in diameter will be used to centre the frame to the aluminium block to mill the other side of the frame. And the last type of drills will be used to help in the milling of the frame.

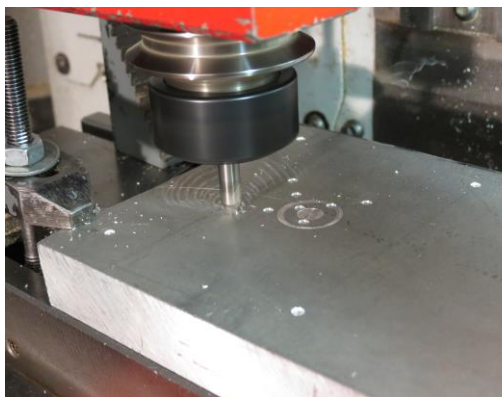


Figure 3-43. Centre drill



Figure 3-44 2.4mm drill

Next mill is the 8mm in diameter flat end mill (figure 3-45). This is used to do the main job because is big in diameter but not very precise.

Due to the shape of the frame, a T shape 25mm mill (figure 3-46) is used to mill the compliant beams.

To finish this side of the frame, a 4mm in diameter flat end mill (figure 3-47).



Figure 3-45. 8mm flat end mill



Figure 3-46. 8mm flat end mill

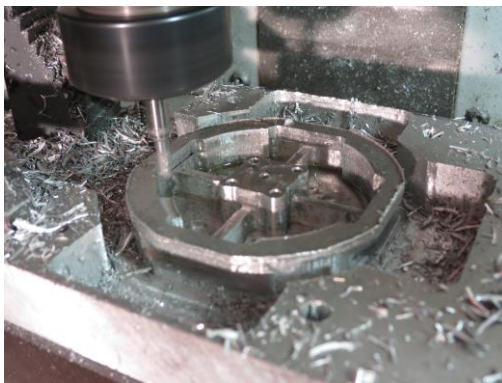


Figure 3-47. 4mm flat end mill

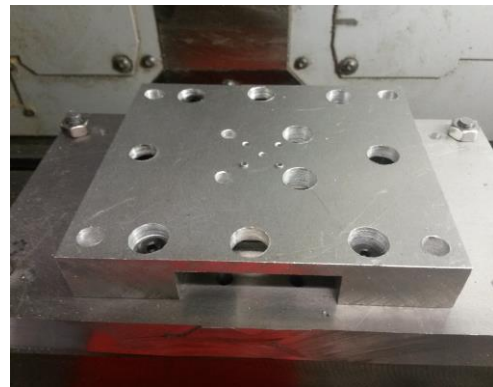


Figure 3-48. Frame in known position

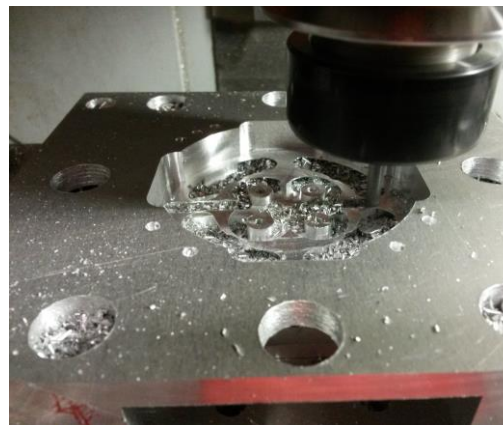


Figure 3-49. 4mm flat end mill

The other side of the frame must be milled in the same position of the first side. To ensure that is in the correct position, calibrated holes have been made in the first side as has been explained before. If drills are made in the same position in the aluminium block, the frame can be screwed in a known position (figure 3-49).

As in the first side, centre drill, 8mm and 4mm flat end mills (figure 3-47) are used to finish the mechanical work frame (figure 3-50).



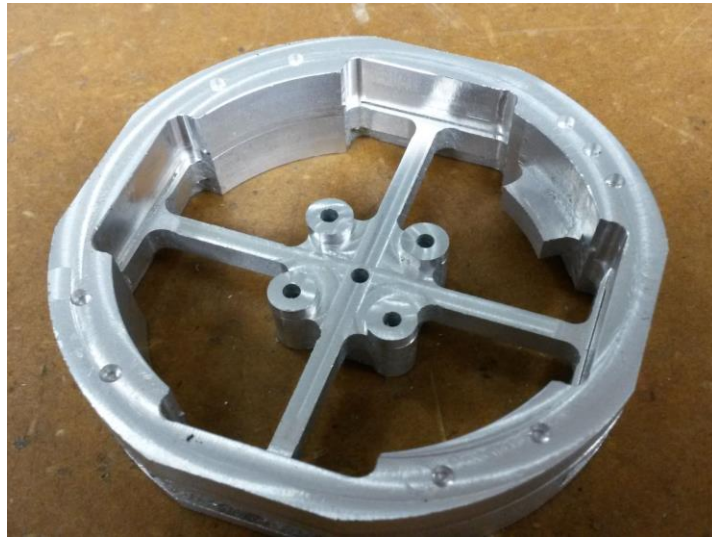


Figure 3-50. Mechanical work finished

## 4. Electronics design

### 4.1. Introduction

The electronic part of this project starts with the selection of the type circuit that will be used. After this, some simulations and prototype tests will be implemented before the final design of the PCB.

Work will be finished after checking that the PCB is properly working.

The complete work diagram can be seen next. (Figure 4-1)

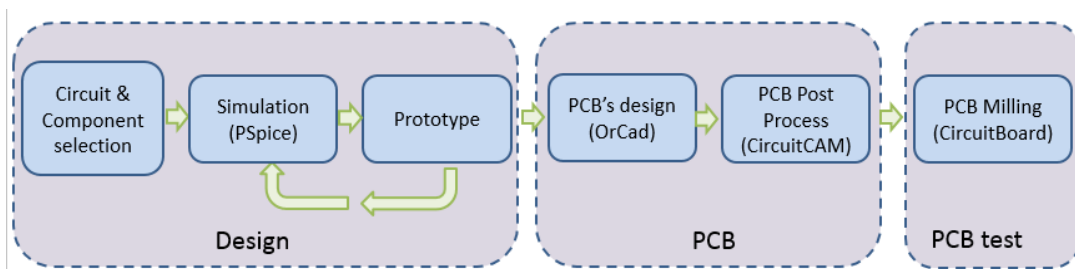


Figure 4-1. Electronic work diagram

### 4.2. Circuit & Component selection

When a force is applied to an elastic structure, the length of that structure is modified. Strain gauges are sensitive to this change of dimension, so, being glued on the deformed structure, their resistance change under the applied load. By measuring this resistive change one can measure the strain. The best method to measure these small changes of resistance is generally through a Wheatstone bridge arrangement [15]. (Figure 4-2)

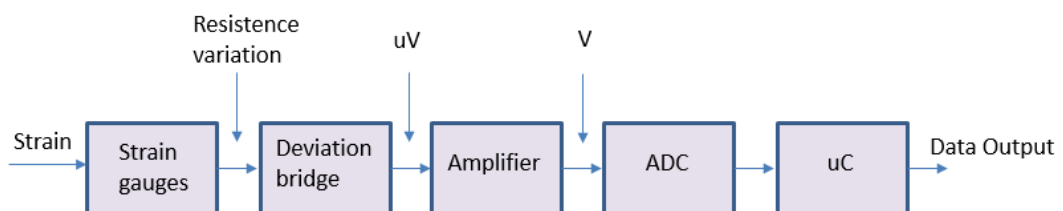


Figure 4-2. General structure of a force measurement chain

There are three specifications used as the primary selection criteria for simultaneous sampling data acquisition devices: speed, resolution, and number of channels. Many architectures are used within data acquisition devices that can affect how are interpreted these specifications with respect to the application. It is important to pay close attention because the analog input architecture used to achieve simultaneous sampling across multiple channels affects how often input channels can be sampled as well as the accuracy of the data acquisition device itself.

The two most common simultaneous sampling architectures are SSH and multi-analog-to-digital converter (multi-ADC) (figure 4-3). The SSH architecture is a derivative of the multiplexed architecture, the most common architecture used in mid- to high-channel-count data acquisition devices. Multiplexed devices use one common amplifier and ADC to sample many input channels, resulting in a time delay between contiguous samples. Time delay can be minimized, but it is limited by the performance of the ADC/amplifier combination. To achieve simultaneous sampling with a multiplexed architecture, the data acquisition device must contain SSH circuitry for each input channel before the ADC/amplifier. This SSH circuitry can be either designed on the data acquisition device or purchased in addition to the data acquisition device in the form of signal conditioning. [25]

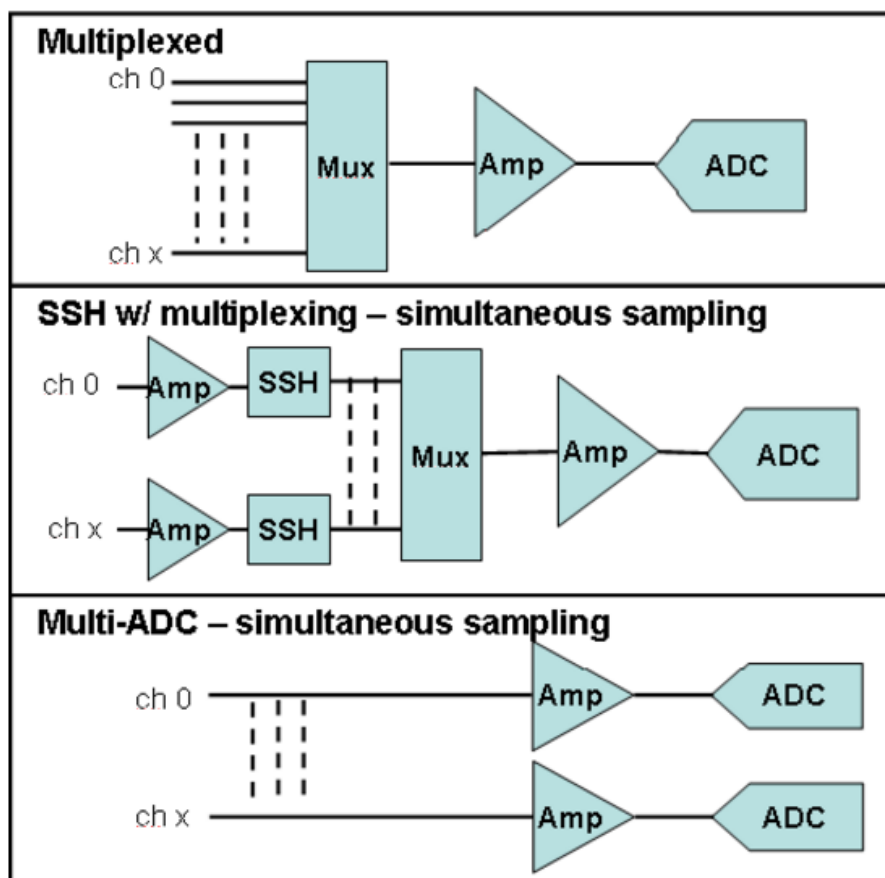


Figure 4-3. Different simultaneous sampling circuits

The multi-ADC architecture delivers higher sample rates per channel, better dynamic accuracy, and less complexity. This architecture does not require a

multiplexer to route all incoming signals to a single ADC nor does it require additional SSH circuits to achieve simultaneous sampling. The absence of multiplexers and SSH circuits greatly simplifies the signal path on the data acquisition device. This simplification permits the optimization of both DC measurements and dynamic measurements while maintaining a low cost per channel. The multi-ADC architecture is flexible, offering the capability to sample multiple incoming signals independently or simultaneously. In addition, the input sample rate is not divided among the number of inputs.

#### 4.2.1. Circuit topology

Due the type of sensor, eight bridge circuits must be sensed in real time, due the nature of the continuous change of force vector. As much higher the frequency we want to detect, much more critical is the sampling time of the variables.

In order to know the variable sampling rate, we must calculate as follows:

$$T_{\_sample} = \frac{1}{f_{\_sample}} \quad (26)$$

Where:

$T_{\_sample}$  is the period of sampling frequency and

$f_{\_sample}$  is the frequency of desired sampling rate

$$T_{\_lsb} = \frac{T_{\_sample}}{2} * \frac{1}{2^{n\_ADC}} \quad (27)$$

Where:

$T_{\_lsb}$  is the time of change for a bit and

$n\_ADC$  is the number of ADC bits.

From Equation (26) and (27):

$$T_{\_lsb} = \frac{1}{2 * f_{\_sample} * 2^{n\_ADC}} \quad (28)$$

As the specifications in table 1 of section 1.1 gives a minimum frequency of 100Hz and a data byte of 10 or 12 bits, the setting time must be of 4.882us for 10 bytes and 1.22us for 12 bytes. This will be the maximum time to do the conversion of the eight bridges to be considered as a conversion in real time.

The option of the use of the microcontroller ADC is not possible, because the time for a channel conversion for an Atmel328 is of 6us [26].

If an 8 bits microcontroller is used, the maximum SPI data transfer is about 4 MHz. For a circuit of an external multiplexed ADC, where two bytes are needed (12 bites ADC), and the time to transfer the 8 channels conversion is:

$$\left\{ \begin{array}{l} 16 \text{ bits} * 8 \text{ channels} = 144 \text{ clocks} \\ 4 \text{ Mhz} \rightarrow T = \frac{1}{4 \text{ Mhz}} = 0.25 \mu\text{s} \end{array} \right\} \rightarrow 144 \text{ clocks} * 0.25 \mu\text{s} = 36 \mu\text{s}$$

Although the price is higher than in the multiplexed option, the architecture of eight amplifiers working in parallel and a multiplexed ADC is chosen for this project because of the better dynamic accuracy (figure 4-4). This is much faster because the chip stores the data conversion in an internal buffer, and then it is transmitted when all conversions are done.

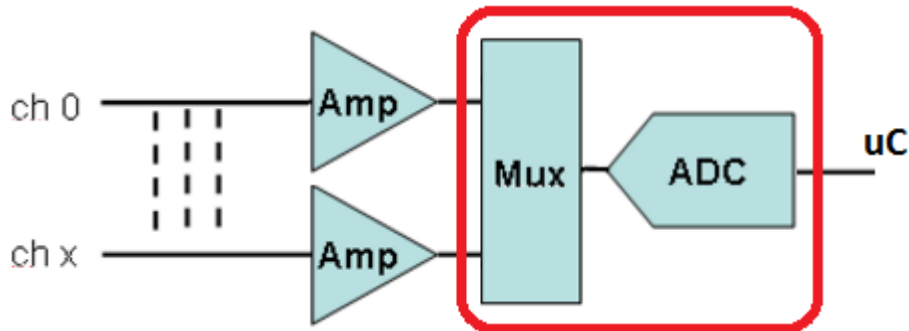


Figure 4-4. Parallel amplifiers and an in circuit multiplexed ADC

#### 4.2.2. Strain gauges

Several restrictions must be kept in mind when a strain gauge is chosen. First of all are the dimensions. As the arm dimension is 3 mm wide, the strain gauge must be smaller. Second restriction is the material where the strain gauge must be glued. In this case the frame is made of aluminium. This is important because different gauges have different thermal expansion factor. For aluminium it is  $23.4 * 10^{-6} / ^\circ\text{C}$ .

The range covers strain gages with nominal resistances of 120, 350, 600 and 700  $\Omega$ . The lowest is the resistance, the highest is the immunity to electrical noise. On the other hand, higher will be the current, the higher will be the self-heating. But in this case it is not important because the bridge will be powered with a very high duty cycle.

The strain sensitivity  $k$  of a strain gauge is the proportionality factor between the relative changes of the resistance and the strain. Strain sensitivity is a figure without dimension and is generally called gauge factor (GF).

The gauge factor  $GF$  is defined as:

$$GF = \frac{\Delta R / R_g}{\varepsilon} \tag{29}$$

Where:

$\Delta R$  is the change in resistance caused by strain,

$R_g$  is the resistance of the undeformed gauge, and

$\varepsilon$  is the strain.

For example, if we assume a gauge with  $GF = 2.0$  and a resistance of  $120 \Omega$ , the resistance change when it is subjected to a strain of 5 microstrain (equivalent of  $3.515 \text{ kg/cm}^2$ ).

$$\Delta R = GF * \epsilon * R = 2 * 5E-6 * 120 = 0.001\%$$

In addition to the challenges of placement location (figure 4-5), there is also the issue of placement orientation uncertainty and error described as:

$$\epsilon'_{xx} = \epsilon_{xx} * \cos^2 \theta + \epsilon_{yy} * \sin^2 \theta + 2 * \left( \frac{\gamma_{xy}}{2} \right) \sin \theta \cos \theta \quad (30)$$

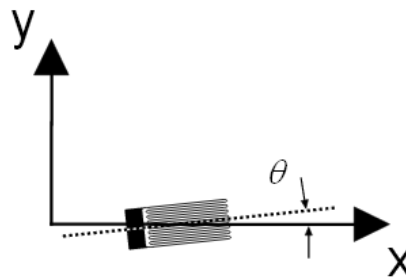


Figure 4-5. Gauge misalignment

This problem can be solved by software calibration.

#### 4.2.3. Wheatstone bridge

The Wheatstone Bridge circuit is nothing more than two simple series-parallel arrangements of resistances connected between a voltage supply terminal and ground producing zero voltage difference between the two parallel branches when balanced. In the circuit shown below it is apparent that the bridge can be imagined as two ballast circuits (composed of  $R_1, R_2$  and  $R_3, R_4$ ) connected so that the initial steady state voltages are cancelled in the measurement of  $e$ . (figure 4-6). [27]

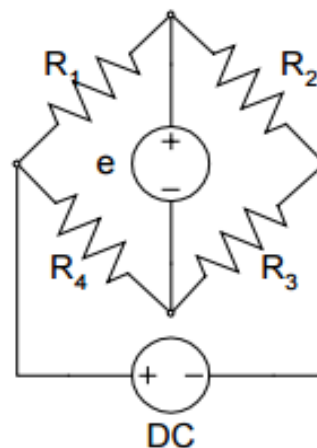


Figure 4-6. Wheatstone Bridge

The output voltage can be written as the difference between two ballast circuits as:

$$e = \left[ \frac{R_2}{R_1 + R_2} - \frac{R_3}{R_3 + R_4} \right] * E = \frac{R_2 * R_4 - R_1 * R_3}{(R_1 + R_2) * (R_3 + R_4)} * E \quad (31)$$

Where E is the voltage used to excite the gauge.

An initial steady state voltage exists unless the numerator above is zero. Such a configuration with zero output voltage is termed as a “Balanced Bridge” and is provided when:

$$R_2 * R_4 = R_1 * R_3 \quad (32)$$

This relationship is not of direct concern here but it is interesting to note that if three of the four resistances are known, the fourth can be determined by rationing the values obtained at balance. For the present, however, we are concerned with the output produced by small changes in the resistance of the bridge arms. If we consider infinitesimal changes in each resistor then  $R_i \rightarrow R_i + dR_i$ , we can compute the differential change in the output voltage, e, as:

$$de = \left[ \frac{R_1 * R_2}{(R_1 + R_2)^2} \left( \frac{dR_1}{R_1} - \frac{dR_2}{R_2} \right) + \frac{R_3 * R_4}{(R_3 + R_4)^2} \left( \frac{dR_3}{R_3} - \frac{dR_4}{R_4} \right) \right] * E \quad (33)$$

If the bridge is balanced so that:

$$R = R_1 = R_2 = R_3 = R_4$$

Using this in the above equation for de yields:

$$de = \frac{1}{4} * \left[ \frac{dR_1}{R_1} - \frac{dR_2}{R_2} + \frac{dR_3}{R_3} - \frac{dR_4}{R_4} \right] * E \quad (34)$$

We can use Equation (29) to express de in terms of the strains as:

$$de = \frac{GF}{4} * [\varepsilon_1 - \varepsilon_2 + \varepsilon_3 - \varepsilon_4] * E$$

Where  $\varepsilon_i$ , is the strain in the gauge placed in the i-th arm of the bridge. Since the bridge is initially balanced, this is the only output and we have the desired result that:

$$e = \frac{GF}{4} * [\varepsilon_1 - \varepsilon_2 + \varepsilon_3 - \varepsilon_4] * E \quad (35)$$

This is the basic equation relating the Wheatstone Bridge output voltage to strain in gauges placed in each arm.

Fluctuations in ambient and operating temperatures produce the most undesired effects which generally are dealt with strain measuring circuitry. The problems arise primarily from two mechanisms: (1) changes in the gauge resistivity with temperature and (2) temperature induced strain in the gauge element.

For example, the value, 260, for an isoelastic material is equivalent (using the definition of GF from Equation (29) and GF=3.5) to an apparent strain:

$$\varepsilon = \frac{\Delta R / R_g}{GF} = \frac{260}{3.5} = 74 \text{ microstrain/}^\circ\text{C}$$

The output is directly proportional to the excitation voltage and to the Gauge Factor. Increasing either will improve measurement sensitivity. But the thermally induced resistance changes in the lead wires and strain gauges may also be significant.

Power generated within a gauge in a Wheatstone Bridge is given as:

$$P_g = E * i$$

Where  $i$  is the current.

Due to the symmetry of the Wheatstone Bridge it is easy to show that one half of the total current flows through any arm and that one half of the power supply voltage develops across it. Thus with  $E$  and  $i$  defined as the Wheatstone Bridge supply voltage and total bridge current:

$$P_g = \frac{E}{2} * \frac{i}{2} = \frac{1}{4} * E * i \quad (36)$$

But since the net bridge resistance is done by 9 pair of strain gauges, it follows that:

$$i = \frac{E}{R_{\text{bridge}}} = \frac{E}{\frac{2 * R_g}{9}} = \frac{9 * E}{2 * R_g} \quad (37)$$

Using Equations (36) and (37):

$$P_g = \frac{1}{4} * E * \frac{9 * E}{2 * R_g} = \frac{9 * E^2}{8 * R_g} \quad (38)$$

Power density is given by:

$$\rho = \frac{P_g}{A_g} = \frac{P_g}{L_g * W_g} \quad (39)$$

Where

$L_g$  is the gauge grid length,

$W_g$  is the gauge grid width, and

$P_g$  is the gauge power dissipation.

Thus the maximum excitation voltage is given by:

$$E_{\text{max}} = 2\sqrt{\rho * L_g * W_g * R_g} \quad (40)$$



Where  $\rho$  is the power density

In this case, thick aluminium can be specified as 0.31 Watts/cm<sup>2</sup>.

So, the maximum voltage used for the bridge excitation is:

$$E_{\max} = 2\sqrt{\rho * L_g * W_g * R_g} = 2\sqrt{0.31 \frac{W}{cm^2} * 0.6cm * 0.25cm * 120\Omega} = 4.724V$$

The simplest method of eliminating temperature effects is to mount a strain gauge on a piece of structure that is not loaded and it does not deform. Then any strain reported by this gauge can be assumed to be entirely due to thermal drift, and this strain can be subtracted from nearby gauge readings. This assumes that all gauges are subjected to the same temperatures, and that all respond similarly to temperature variations.

From Equation (35) it can be deduced that a quarter bridge circuit can be calculated as:

$$e = \frac{GF}{4} * [\varepsilon_1] * E \quad (41)$$

To reflect the changes in bridge performance by adding one or more additional active arms, a bridge factor, K, will be added so that the new bridge equation is:

$$e = k * \frac{GF}{4} * [\varepsilon_1] * E \quad (42)$$

For example, a quarter-bridge has a value, K=1, while a bridge in which all arms contribute equally and additively, K=4. Practical values lay somewhere in between.

A common example might be a truss element which is designed to carry axial load. In this case application of a single strain gauge oriented in the axial direction on the bar would appear to be sufficient. However, several problems arise. First, there is the problem of what to do about the other 3 arms of the Wheatstone Bridge, but second, it is not always so easy to assume that a single gauge will correctly sense only the axial strain in the bar. For example, while the stress state may be uniaxial (consist of only a single nonzero stress), the strain state is not, and there are significant lateral strains that the gauge could sense, especially if it is not accurately aligned. Moreover, any slight bending in the member (due to initial eccentricities, for example) or other irregularities might cause the axial strain to vary across the cross section of the bar.

Table 9 shown below summarizes some of the most common situation that might be encountered.

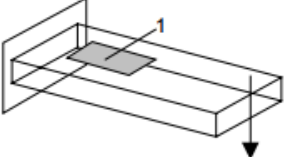
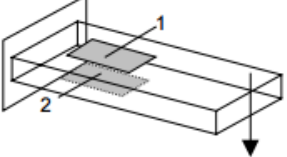
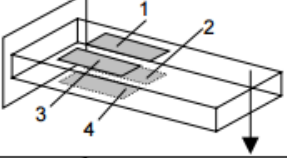
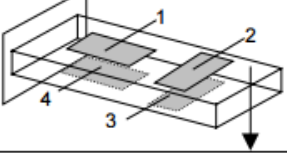
No.	K	Configuration	Notes
F-1	1		Also responds equally to axial strains; must use dummy gage in an adjacent arm (2 or 4) to achieve temperature compensation
F-2	2		Half-bridge; rejects axial strain and is temperature compensated; dummy resistors in arms 3 & 4 can be in strain indicator.
F-3	4		<b>Best:</b> Max sensitivity to bending; rejects axial strains; temperature compensated.
F-4	2(1+v)		Adequate, but not as good as F-3; compensates for temperature and rejects axial strain.

Table 9 - Bridge Configurations for uniaxial members

The configuration chosen for the project is the F-4, also called half bridge. Where gauges 1 and 4 are the sensitive ones, and 2 and 3 are the dummy ones for temperature compensation.

As have been explained before, this frame has four arms and eight bridges. But four gauges are not used per bridge, only a pair of dummy gauges will be used, and all bridges will share it (figure 4-7). This way strain gauges and excitation current are saved.

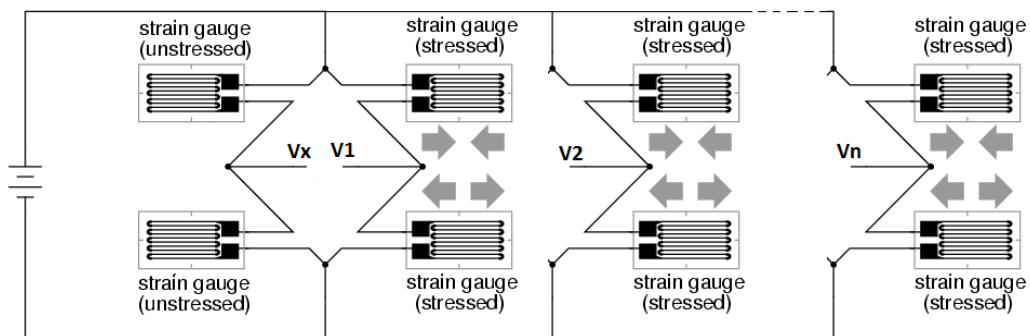


Figure 4-7. A pair of dummy gauges shared by eight half bridges

A careful procedure must be taken to glue the strain gauges,

The components being bonded must be carefully cleaned to eliminate dirt, grease, and oxide layers. Thorough preparation is a basic requirement to achieve good adhesion.

Roughness of the surface is important in addition to the cleanliness at the measuring point. This increases the active surface available for bonding at a microscopic level. Sand-blasting is typically used for this purpose such as with a simple emery paper with an appropriate grain size between 180 and 300.

Strain gauges can be applied using cold or hot curing adhesives. In experimental stress analysis, fast-acting adhesives (superglues) are commonly used as they cure very rapidly at room temperature [29].

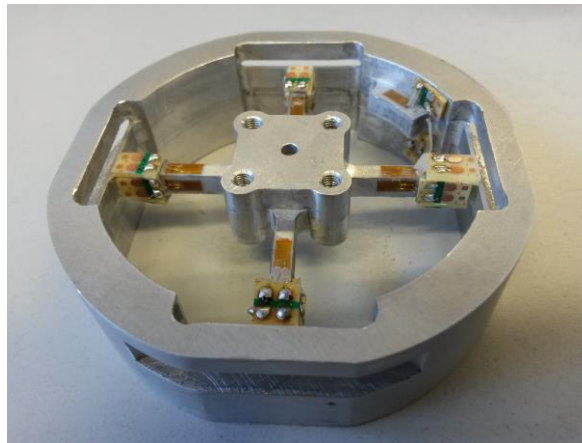


Figure 4-8. Strain gauges glued in the frame

In figure 4-8, the eight pair of strain gauges and the dummy ones are shown.

As it is said in this section, self-heating is a big problem to maintain the bridge balanced. To minimize this problem, the lowest excitation voltage is used. In this case, a voltage regulator reduces and stabilizes the supply voltage to 4V. The NCV4274 (figure 4-9) is a 400mA, adjustable and fixed output voltage, low dropout linear regulator. The device includes pass element, error amplifier, band-gap reference, current limit and thermal shutdown circuitry.

A switch has been added to turn on the Wheastone Bridge power supply. This is especially important because, the bridge is not necessary excited the most of the time

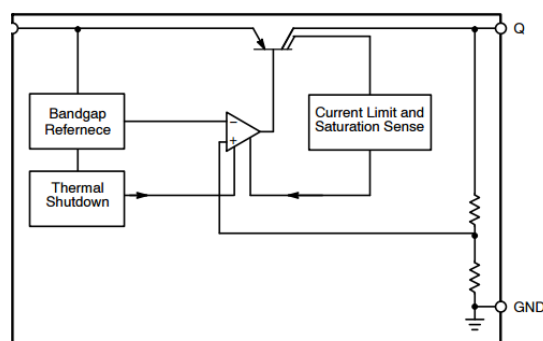


Figure 4-9. NCV4274 Block diagram

#### 4.2.4. Bridge balancing

It has been assumed that the Wheatstone Bridge circuit was initially balanced with all equal resistances [27]. In reality, this is not the case due to inherent irregularities even in the most accurate strain gauges and dummy resistances. As a result, the bridge output voltage,  $E$ , is not zero and it may show an initial unbalance as much as 0.1% of  $E$ . This may actually surpass the true strain-induced signal in many cases. Fortunately, there is a relatively simple and straightforward method for eliminating this unbalance without adversely affecting the basic bridge circuit. It simply consists of some method to add or subtract resistance in any arm in order to satisfy the balance requirement:

$$R_1 * R_3 = R_2 * R_4$$

The adjustment may be made singly in one arm or relatively (differentially) in two or more arms. A small resistance is shown added in series with  $R_i$  (figure 4-10) to increase the arm resistance. The problem here is that this approach can only be used to increase the left hand side of the above balance equation; thus one must know in advance which arm(s) have the lowest resistance.

A second problem is that the added balance resistance must be extremely small in order not to unbalance the bridge in the opposite direction. The magnitude of this added balance resistance can be determined from the Wheatstone bridge equation.

In a typical situation, the unbalance output voltage is a few millivolts for an excitation voltage of five or ten volts. For example, given  $e_o = 0.005$  V and  $E=5$ V:

$$\frac{\Delta R_1}{R_1} = 4 * \frac{0.005}{5} = 0.00025 = 0.025\%$$

And for a 120  $\Omega$  gauge;

$$\Delta R_1 = 0.00025 * 120\Omega = 0.03\Omega$$

This is a very small resistance and is in fact, comparable in magnitude to the contact resistance between mating connectors in a circuit cable. In strain gauge bridges, this approach is not practical. On the other hand, a much larger resistance can be added in parallel with an arm to reduce its effective resistance and therefore to balance the bridge (figure 4-11).

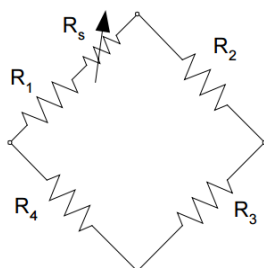


Figure 4-10. Serial resistor

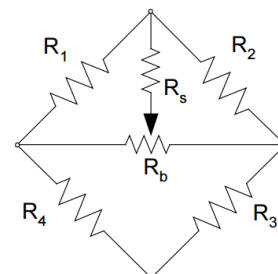


Figure 4-11. Parallel

To avoid modifying manually the circuit, a digital resistor is implemented in the circuit to balance the bridge. In this case, the AD5171 Digital Potentiometer (RDAC) is used (figure 4-12).

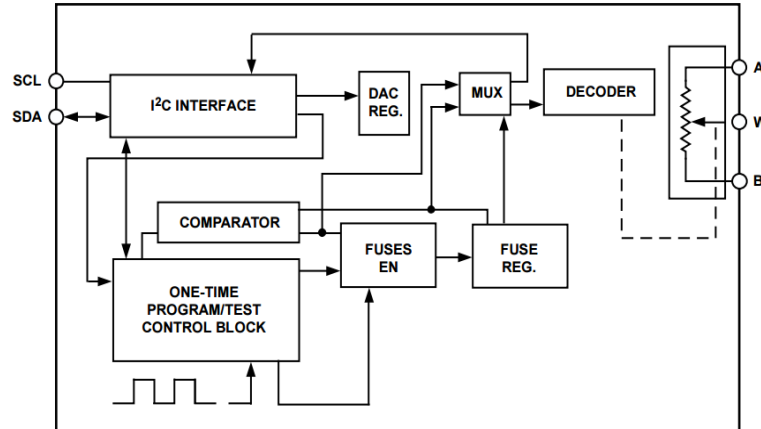


Figure 4-12. Detailed Functional Block Diagram of AD5171

The AD5171 is a 64-position, one-time programmable (OTP) digital potentiometer that uses fuse link technology to achieve the memory retention of the resistance setting function. OTP is a cost-effective alternative over the EEMEM approach for users who do not need to reprogram new memory settings in the digital potentiometer. This device performs the same electronic adjustment function as most mechanical trimmers and variable resistors. The AD5171 is programmed using a 2-wire I2C bus. It allows unlimited adjustments before permanently setting the resistance value. During the OTP activation, a permanent fuse blown command is sent after the final value is determined, freezing the wiper position at a given setting.

The nominal resistance ( $R_{AB}$ ) of the RDAC has 64 contact points accessed by the wiper terminal W, plus Terminal B contact if  $R_{WB}$  is considered. The 6-bit data in the RDAC latch is decoded to select one of the 64 settings. Assuming that a 10 k $\Omega$  part is used, the first connection of the wiper starts at Terminal B for Data 0x00. Such a connection yields a minimum of 60  $\Omega$  resistance between Terminal W and Terminal B due to the 60  $\Omega$  wiper contact resistance. The second connection is the first tap point, which corresponds to 219  $\Omega$  ( $R_{WB} = 1 \times R_{AB}/63 + R_W$ ) for Data 0x01, and so on. Each LSB data value increase moves the wiper up the resistor ladder until the last tap point is reached at 10,060  $\Omega$  ( $63 \times R_{AB}/63 + R_W$ ). The general equations determining  $R_{WB}$  and  $R_{WA}$  are:

$$R_{WB}(D) = \frac{D}{63} * R_{AB} + R_W ; R_{WA}(D) = \frac{63-D}{63} * R_{AB} + R_W \quad (43)$$

Where:

D is the decimal equivalent of the 6-bit binary code,

$R_{AB}$  is the end-to-end resistance,

$R_W$  is the wiper resistance contributed by the on-resistance of the internal switch.

As this potentiometer is used to balance the bridge (figure 4-13), we must calculate the parallel effect of both resistances as:

$$V_w(D) = \frac{E}{\left(\frac{63-D}{63} * R_{AB} + R_W + R_A \parallel R_g\right) + \left(\frac{D}{63} * R_{AB} + R_W + R_B \parallel R_g\right)} * \left(\frac{D}{63} * R_{AB} + R_W + R_B \parallel R_g\right) \tag{44}$$

Where:

Rg is the resistance of a strain gauge, and

E is the excitation voltage of the Wheatstone Bridge.

For an excitement of 4V and a Rg=120, the difference between maximum and minimum is:

$$V_w(D = 0) = 2.005879V$$

$$V_w(D = 63) = 1.99399V$$

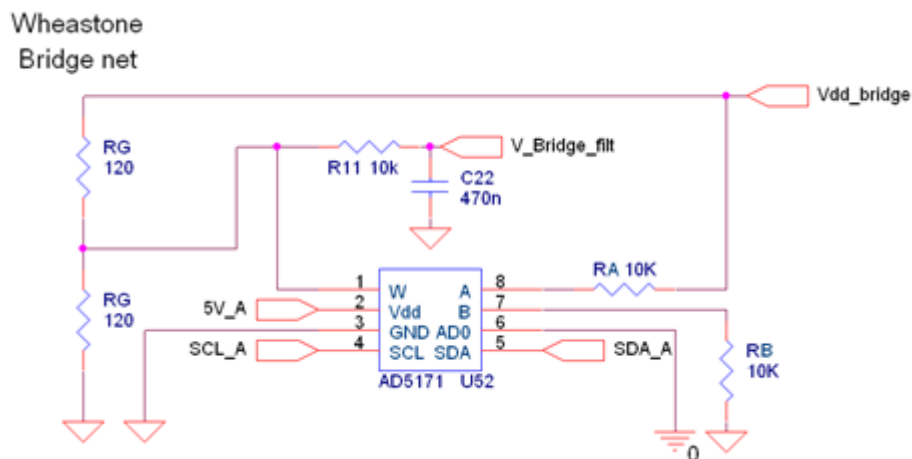


Figure 4-13. Balancing circuit schema

In this circuit there are also a 1<sup>st</sup> order LPF done with R11 and C22, with a cut-off frequency of 33Hz.

### 4.2.5. Instrumentation Amplifier

The best way to amplify the output signal of a Wheatstone bridge is an instrumentation amplifier.

An instrumentation amplifier is a type of differential amplifier that has been outfitted with input buffer amplifiers, which eliminate the need for input impedance matching and thus make the amplifier particularly suitable for use in measurement and test equipment. Additional characteristics include very low DC offset, low drift, low noise, very high open-loop gain, very high common-mode rejection ratio, and very high input impedances. Instrumentation amplifiers are used where great accuracy and short and long-term stability of the circuit are required.

In this case, the amplifier chosen is the AD8293G160 (figure 4-15). It is a low cost, low noise and rail-to-rail output amplifier, with a fixed gain of 160.

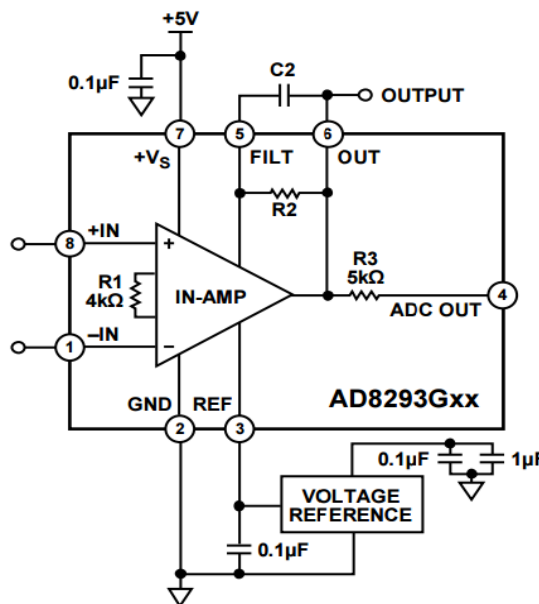


Figure 4-14. AD8293G160 typical use

The output voltage is set as:

$$V_{out} = V_{ref} + \left( \frac{2 * 320k}{4k} \right) (V_{inp} - V_{inn})$$

Other important characteristics are a low offset voltage of 20 µV (AD8293G160B), an offset voltage drift of 0.3µV/°C, a voltage noise of only 0.7 µV p-p (0.01 Hz to 10 Hz), and single supply voltage operation.

The output of the AD8293G160 can be filtered to reduce switching ripple. Two filters can be used in conjunction to set the filter frequency. In the circuit chosen, two 50Hz filters are used in conjunction to form a 30Hz bandwidth. Because the filter resistors are integrated in the AD8293G160, only external capacitors are needed to set the filter frequencies.

The following equation results in the C2 value needed to set a 50Hz primary filter.

$$C_2 = \frac{1}{50\text{Hz} * 2 * \pi * 320\text{k}\Omega} = 9.95\text{nF}$$

Adding an external capacitor, C3, and measuring the output from ADC OUT further reduces the correction ripple. The internal 5 kΩ resistor, labelled R3 in figure 4-14, forms a low-pass filter with C3. This low-pass filter is the secondary filter. Set to 50 Hz, the secondary filter equation for C3 is as follows:

$$C_3 = \frac{1}{50\text{Hz} * 2 * \pi * 5\text{k}} = 636.9\text{nF}$$

A 0.1μF surface-mount capacitor is connected between the supply lines. This capacitor is necessary to minimize ripple from the correction clocks inside the IC. For single-supply operation, a 0.1μF surface-mount capacitor is connected from the supply line to GND.



### 4.2.6. Amplifier

Because of the low level signal at the output of the instrumentation amplifier, a second amplifier has been implemented in the circuit. In this case it is used an OPA336 (figure 4-15).

OPA336 series microPower CMOS operational amplifiers are designed for battery-powered applications. They operate on a single supply operation as low as 2.1V. The output is rail-to-rail and swings to within 3mV of the voltage supplies with a 100kΩ load. The common-mode range extends to the negative supply ideal for single-supply applications. Single, dual, and quad versions have identical specifications for maximum design flexibility. In addition to small size and low quiescent current (20μA/amplifier), they feature low offset voltage (125μV max), low input bias current (1pA), and high open loop gain (115dB). Dual and quad designs feature completely independent circuitry for lowest crosstalk and freedom from interaction.

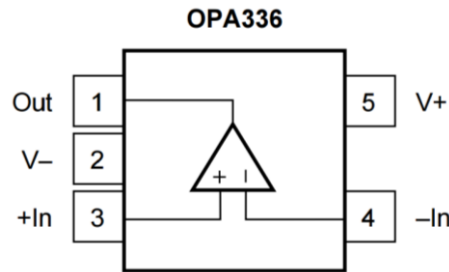


Figure 4-15. OPA336

The configuration chosen is a non-inverted amplifier with a single pole LPF (figure 4-16).

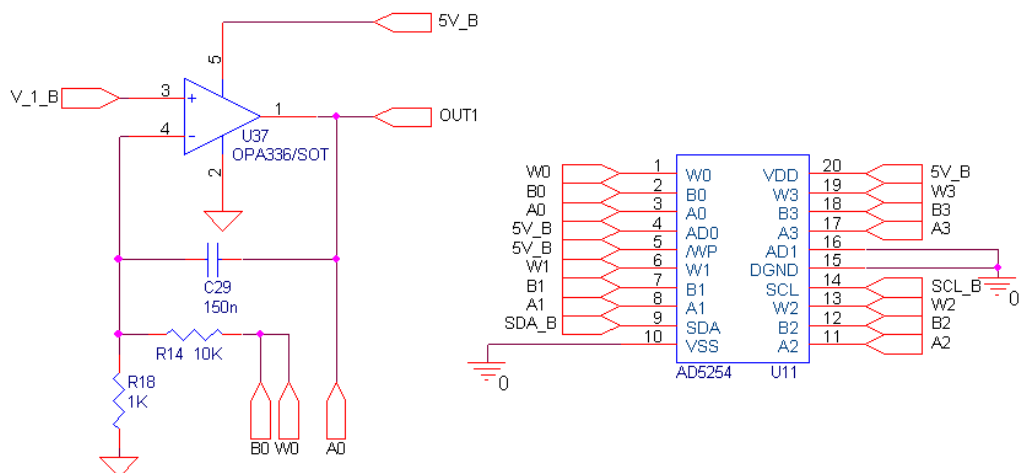


Figure 4-16. OPA336 in non-inverter configuration and variable gain

Because we want the maximum signal at different force range, we have a digital resistor AD5254 added to the feedback resistor. This allows adjusting the gain as:

$$A_v = 1 + \frac{R_{14} + Rab + R_w}{R_{18}}$$

Where Rab is the resistance of the digital potentiometer and

Rw is the Wiper resistance (200Ω @3V supply for the AD5254).

The cut-off frequency for the filter also varies from 106 to 53Hz, because is defined as:

GainCu

The AD5254 (figure 4-17) are quad-channel, I2C non-volatile memory, digitally controlled potentiometers with 256 positions. These devices perform the same electronic adjustment functions as mechanical potentiometers, trimmers, and variable resistors. The parts versatile programmability allows multiple modes of operation, including read/write access in the RDAC and EEMEM registers, increment/decrement of resistance, resistance changes in ±6 dB scales, wiper setting read back, and extra EEMEM for storing user-defined information, such as memory data for other components, look-up table, or system identification information.

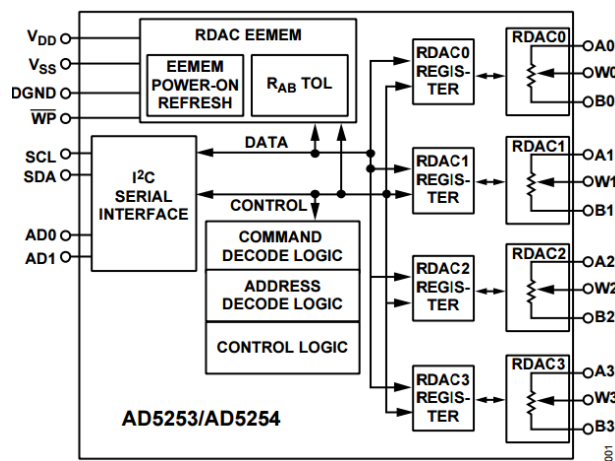


Figure 4-17. AD5254 functional block diagram

In this case, as the digital resistance is 10k, the gain goes from 11,2 to 21,2 in 256 steps. This means that between steps, there is a difference of 0.039 in gain.

#### 4.2.7. Digital Communications

Although the force sensing is analogical, several devices need digital communications. Because of the small area of PCB, it is not possible to use parallel communications, and two different serial protocols are used, I2C and SPI depending on their characteristics.

I2C needs 2 lines and that's it, while SPI formally defines at least 4 signals, and more if you add slaves (figure 4-18). Some unofficial SPI variants only need 3 wires, which are a SCLK, a SS and a bi-directional MISO/MOSI line. Still, this implementation would require one SS line per slave. SPI requires additional work, logic and/or pins if a multi-master architecture has to be built on SPI. The only problem of I2C when building a system is a limited device address space on 7 bits, which is overcome with the 10-bits extension.

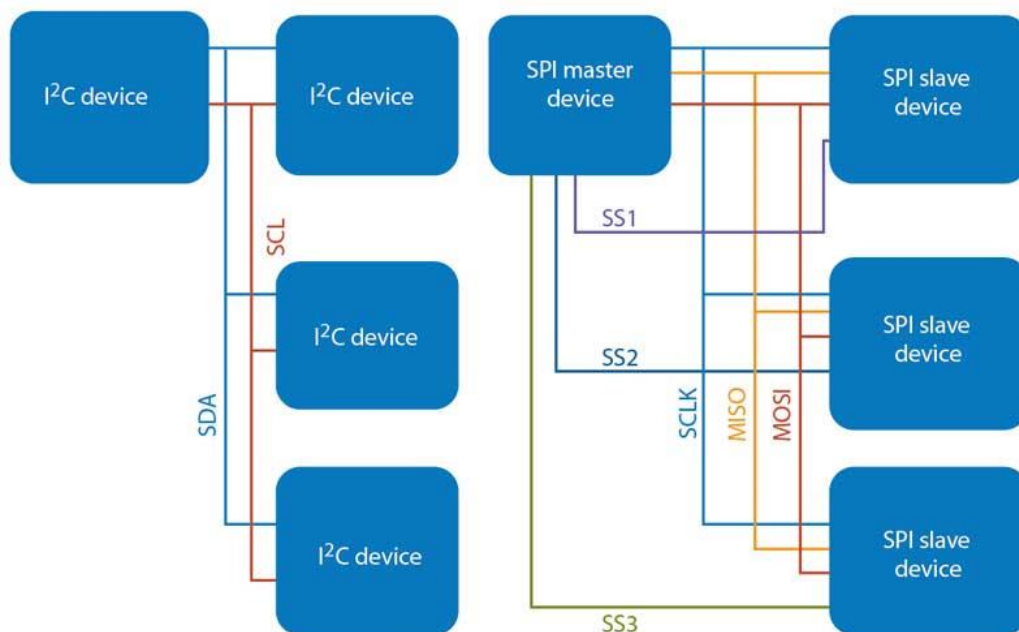


Figure 4-18. I2C vs. SPI protocols

If data must be transferred at high speed, SPI is clearly the protocol of choice, over I2C. SPI is full-duplex; I2C is not. SPI does not define any speed limit; implementations often go over 10 Mbps. I2C is limited to 1Mbps in Fast Mode+ and to 3.4 Mbps in High Speed Mode – this last one requiring specific I/O buffers, not always easily available.

In our case, or calibration process is not indispensable to use high speed, thus I2C protocol is used because the small PCB area, but for force sensing operation, speed is prioritized, so SPI protocol is better.

Pullup resistors need to be connected from the I2C lines to the supply line to enable communication. The pullup resistors pull the line high when it is not driven low by the open-drain interface. The value of the pullup resistor is an important design consideration for I2C systems as an incorrect value can lead to signal loss.

A strong pullup (small resistor) prevents the I2C pin of an IC from being able to drive low. The Vol (Output Voltage Level) valid level that can be read as a valid logical “low” by the input buffers of an IC determines the minimum pullup resistance.

$R_p(\min)$  is a function of VCC, Vol (max), and Iol:

$$R_p(\min) = \frac{V_{cc} - Vol(\max)}{I_{ol}}$$

The maximum pullup resistance is limited by the bus capacitance (Cb) due to I2C standard rise time specifications. If the pullup resistor value is too high, the I2C line may not rise to a logical “high” before it is pulled low. The response of an RC circuit to a voltage step of amplitude VCC, starting at time  $t = 0$  is characterized by time constant RC. Thus the maximum pullup resistance is a function of the maximum rise time (tr):

$$R_p(\max) = \frac{tr}{(0.8473 * C_b)}$$

The maximum number of nodes is limited by the address length, and also by the total bus capacitance of 400 pF, which restricts practical communication distances to a few meters, but in this case, if every device has an average capacitance of 10pF, the total capacitance of the line is far away from the maximum.

The maximum rise time (tr) for fast mode ( $f(scl)=400Khz$ ) is 300ns.

So, the maximum  $R_p$  will be:

$$R_p(\max) = \frac{tr}{0.8473 * C_b} = \frac{300ns}{0.8473 * 100pF} = 3.54k\Omega$$

And the minimum  $R_p$  for a supply of 5V, Vol of 0.4V and the standard 3mA as Iol:

$$R_p(\min) = \frac{V_{cc} - Vol(\max)}{I_{ol}} = \frac{5V - 0.4V}{3mA} = 1533\Omega$$

Therefore, we can select any available resistor value between 1533 $\Omega$  and 3.54k $\Omega$ . The value of the pullup resistor can be selected based on the trade-off between the power consumption and speed.

Pullup resistors of 1800  $\Omega$  have been chosen because is the commercial value more similar and greater than 1533  $\Omega$ .

#### 4.2.8. ADC

As it is explained in section 4.2.1, an independent ADC is necessary to achieve the bandwidth of the specification. And it as is explained in section 4.2.7, the SPI protocol is the best election for this device.

Most ADC applications [33] today can be classified into four broad market segments: (a) data acquisition, (b) precision industrial measurement, (c) voice band and audio, and (d) “high speed” (implying sampling rates greater than about 5 MSPS). A very large percentage of these applications can be filled by successive-approximation (SAR), sigma-delta ( $\Sigma$ - $\Delta$ ), and pipelined ADCs. (Figure 4-19)

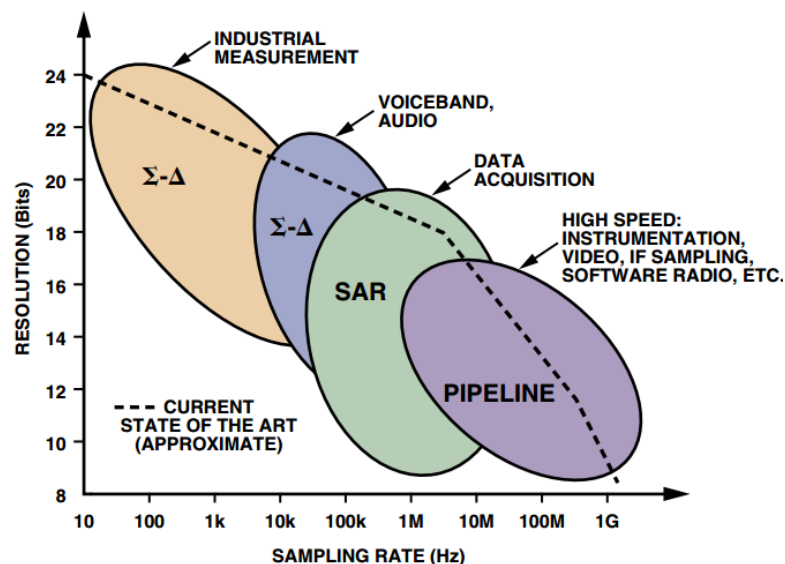


Figure 4-19. ADC architectures, resolution vs. sampling

##### - Successive-Approximation ADCs for Data Acquisition

The successive-approximation ADC is by far the most popular architecture for data-acquisition applications, especially when multiple channels require input multiplexing. In order to process rapidly changing signals, SAR ADCs have an input sample-and-hold (SHA) to keep the signal constant during the conversion cycle. The conversion starts with the internal D/A converter (DAC) set to midscale. The comparator determines whether the SHA output is greater or less than the DAC output, and the result (the most-significant bit (MSB) of the conversion) is stored in the successive-approximation register (SAR) as a 1 or a 0. The DAC is then set either to 1/4 scale or 3/4 scale (depending on the value of the MSB), and the comparator makes the decision for the second bit of the conversion. The result (1 or 0) is stored in the register, and the process continues until all of the bit values have been determined. At the end of the conversion process, a logic signal (EOC, DRDY, BUSY, etc.) is asserted. The acronym, SAR, which actually stands for successive-approximation register—the logic block that controls the conversion process—is universally understood as an abbreviated name for the entire architecture.

- Sigma-Delta ( $\Sigma$ - $\Delta$ ) ADCs for Precision Industrial Measurement and Instrumentation

Modern  $\Sigma$ - $\Delta$  ADCs have virtually replaced the integrating-type ADCs (dual-slope, triple-slope, quad-slope, etc.) for applications requiring high resolution (16 bits to 24 bits) and effective sampling rates up to a few hundred hertz. High resolution, together with on-chip programmable-gain amplifiers (PGAs), allows the small output voltages of sensors—such as weigh scales and thermocouples—to be digitized directly. Proper selection of sampling rate and digital filter bandwidth also yields excellent rejection of 50Hz and 60Hz power-line frequencies.  $\Sigma$ - $\Delta$  ADCs offer an attractive alternative to traditional approaches using an instrumentation amplifier (in-amp) and a SAR ADC.

- Pipelined ADCs

The pipelined analog-to-digital converter (ADC) has become the most popular ADC architecture for sampling rates from a few mega samples per second (MSPs) up to 100MSPs. Resolutions range from eight bits at the faster sample rates up to 16 bits at the lower rates. These resolutions and sampling rates cover a wide range of applications, including CCD imaging, ultrasonic medical imaging, digital receivers, base stations, digital video (for example, HDTV), xDSL, cable modems, and fast Ethernet. The analog input, is first sampled and held steady by a sample-and-hold (S&H), while the flash ADC in stage one quantizes it to three bits. The 3-bit output is then fed to a 3-bit DAC (accurate to about 12 bits), and the analog output is subtracted from the input. This "residue" is then gained up by a factor of four and fed to the next stage (Stage 2). This gained-up residue continues through the pipeline, providing three bits per stage until it reaches the 4-bit flash ADC, which resolves the last 4LSB bits. Because the bits from each stage are determined at different points in time, all the bits corresponding to the same sample are time-aligned with shift registers before being fed to the digital-error-correction logic. Note when a stage finishes processing a sample, determining the bits, and passing the residue to the next stage, it can then start processing the next sample received from the sample-and-hold embedded within each stage. This pipelining action is the reason for the high throughput.

The choice has been the MAX11628 ADC with a successive – approximation architecture. This is the architecture of choice for nearly all multiplexed data acquisition systems, as well as for many instrumentation applications. The SAR ADC is relatively easy to use, has no pipeline delay, and is available with resolutions to 18 bits and sampling rates up to 3 MSPS.

The MAX11628 (figure 4-20) is a serial 12-bit analog-to-digital converter (ADCs) with an internal reference. This device feature on-chip FIFO, scan mode, internal clock mode, internal averaging, and AutoShutdown™. The maximum sampling rate is 300ksps using an external clock. The MAX11628 have 8 input channels. This 12-bit ADCs have internal track and hold (T/H) circuitry supporting single ended inputs. Data is converted from analog voltage sources in a variety of channel and data-acquisition configurations.

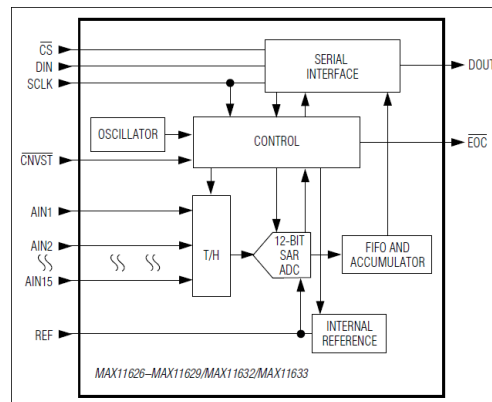


Figure 4-20. MAX11628 block diagram

The MAX11628 feature a serial interface compatible with SPI/QSPI and MICROWIRE devices. For SPI/QSPI, ensure the CPU serial interface runs in master mode so it generates the serial clock signal. Select the SCLK frequency of 10MHz or less, and set clock polarity (CPOL) and phase (CPHA) in the  $\mu$ P control registers to the same value. The MAX11628 operate with SCLK idling high or low, and thus operate with CPOL = CPHA = 0 or CPOL = CPHA = 1. Set CS low to latch input data at DIN on the rising edge of SCLK. Output data at DOUT is updated on the falling edge of SCLK. Results are output in binary format. Serial communication always begins with an 8-bit input data byte (MSB first) loaded from DIN. A high-to-low transition on CS initiates the data input operation. The input data byte and the subsequent data bytes are clocked from DIN into the serial interface on the rising edge of SCLK. Bits 5 and 4, CKSEL1 and CKSEL0, respectively, control the clock modes in the setup register. Choose between four different clock modes for various ways to start a conversion and determine whether the acquisitions are internally or externally timed. Select clock mode 00 to configure CNVST/AIN\_ to act as a conversion start and use it to request the programmed, internally timed conversions without tying up the serial bus. In clock mode 01, use CNVST to request conversions one channel at a time, controlling the sampling speed without tying up the serial bus. Request and start internally timed conversions through the serial interface by writing to the conversion register in the default clock mode 10. Use clock mode 11 with SCLK up to 4.8MHz for externally timed acquisitions to achieve sampling rates up to 300ksps. Clock mode 11 disables scanning and averaging. See Figures 4–7 for timing specifications and how to begin a conversion. These devices feature an active-low, end-of-conversion output. EOC goes low when the ADC completes the last requested operation and is waiting for the next input data byte (for clock modes 00 and 10). In clock mode 01, EOC goes low after the ADC completes each requested operation. EOC goes high when CS or CNVST goes low. EOC is always high in clock mode 11.

As we use 8 channels, and this device has the CNVST/AIN\_ used as analog input, it is necessary to operate in Clock Mode 10 Timing (figure 4-21).

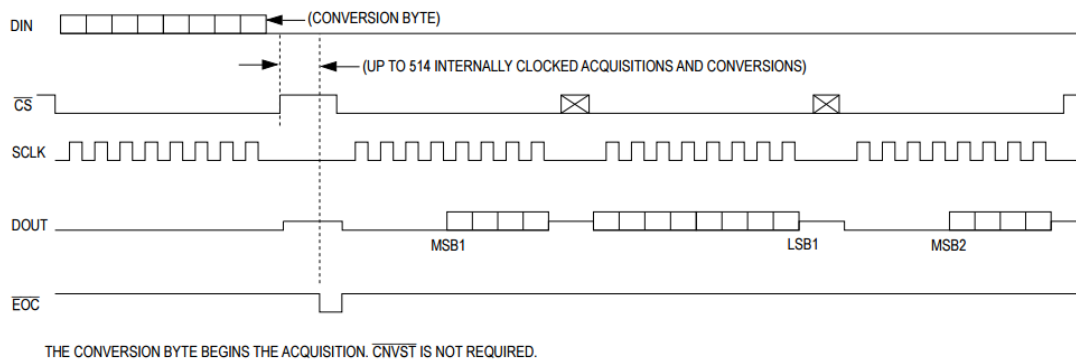


Figure 4-21. Clock Mode 10 Timing

In Clock Mode 10, the wake-up, acquisition, conversion, and shutdown sequences are initiated by writing an input data byte in the conversion register, and they are performed automatically using the internal oscillator. This is the default clock mode upon power-up. See Figure 6 for Clock Mode 10 timing. The scan initiates by writing a byte to the conversion register. The MAX11628 then powers up, scans all requested channels, stores the results in the FIFO, and shuts down. After the scan is complete, EOC is pulled low and the results are available in the FIFO. EOC stays low until CS is pulled low again.

This circuit has the ability of taking some samples per channel, doing an internal averaging, and sending a single result. Write to the averaging register to configure the ADC to average up to 32 samples for each requested result, and to independently control the number of results requested for single-channel scans. The number of averaging samples are 1, 4, 8, 16 or 32.

The acquisition time,  $t_{ACQ}$ , is the maximum time needed for a signal to be acquired, plus the power-up time. It is calculated by the following equation:

$$t_{ACQ} = 9 \times (RS + RIN) \times 24pF + t_{PWR} \quad (45)$$

where,

$RIN$  is the input impedance with a value of  $1.5k\Omega$ ,  $RS$  is the source impedance of the input signal,

and  $t_{PWR} = 1\mu s$ , the power-up time of the device.

The varying power-up times are detailed in the explanation of the clock mode conversions. When the conversion is internally timed,  $t_{ACQ}$  is never less than  $1.4\mu s$ , and any source impedance below  $300\Omega$  does not significantly affect the ADC's AC performance. A high-impedance source can be accommodated either by lengthening  $t_{ACQ}$  or by placing a  $1\mu F$  capacitor between the positive and negative analog inputs.

Applying these values, and assuming that the output impedance of the operational amplifier is very low with respect to the input impedance of the ADC, and also assuming that the device is powered-up, the time of acquisition is:



$$t_{ACQ} = 9 \times 1.5k\Omega \times 24pF = 0.324 \mu s$$

The conversion time for each scan is based on several factors: conversion time per sample, samples per result, results per scan, and if the external reference is in use. It is used the following formula to calculate the total conversion time for an internally timed conversion:

$$\text{Total Conversion Time} = t_{CNV} \times n_{AVG} \times n_{RESULT} + t_{RP} \quad (46)$$

Where,

$$t_{CNV} = t_{ACQ} (\text{max}) + t_{CONV} (\text{max}).$$

$$n_{AVG} = \text{samples per result (amount of averaging).}$$

$n_{RESULT}$  = number of FIFO results requested; determined by the number of channels being scanned or by NSCAN1, NSCAN0.

$t_{RP}$  = internal reference wake-up; set to zero if internal reference is already powered up or external reference is being used.

In this case, using the internal clock of 4 MHz (3.5  $\mu s$ ) and assuming again that the device is powered-up, the Total Conversion Time is:

$$\begin{aligned} \text{Total Conversion Time} &= (t_{ACQ} (\text{max}) + t_{CONV} (\text{max})) \times n_{AVG} \times n_{RESULT} = \\ &= (0.324 \mu s + 3.5 \mu s) \times n_{AVG} \times 8 = 30.592 \mu s \times n_{AVG} \end{aligned}$$

Despite the MAX11628 have an internal reference (4.096V), is too much high for our circuit, then an external reference voltage is needed.

The ISL60002 (figure 4-22) FGA voltage references are very high precision analog voltage references fabricated in Intersil's proprietary Floating Gate Analog (FGA) technology and feature low supply voltage operation at ultra-low 350nA operating current. Additionally, the ISL60002 family features guaranteed initial accuracy as low as  $\pm 1.0mV$  and 20ppm/ $^{\circ}C$  temperature coefficient. The initial accuracy and temperature stability performance of the ISL60002 family, plus the low supply voltage and 350nA power consumption, eliminates the need to compromise thermal stability for reduced power consumption, making it an ideal companion to high resolution, low power data conversion systems.

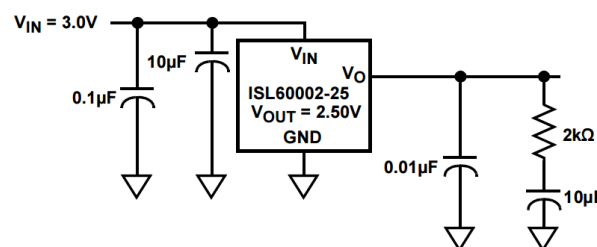


Figure 4-22. ISL60002 noise reduction network

#### 4.2.9. Micro Controller

The microcontroller selected for this project is the ATmega328 (figure 4-23) because it has a very good power consumption versus processing speed ratio.

Other interesting features are [30]:

- Advanced RISC Architecture
  - 131 Powerful Instructions
  - Most Single Clock Cycle Execution
  - 32 x 8 General Purpose Working Registers
  - Fully Static Operation
  - Up to 20 MIPS Throughput at 20MHz
  - On-chip 2-cycle Multiplier
- High Endurance Non-volatile Memory Segments
  - 32KBytes of In-System Self-Programmable Flash program Memory
  - 1KBytes EEPROM
  - 2KBytes Internal SRAM
  - Write/Erase Cycles: 10,000 Flash/100,000 EEPROM
- Peripheral Features
  - Two 8-bit Timer/Counters with Separate Prescaler and Compare Mode
  - One 16-bit Timer/Counter with Separate Prescaler, Compare Mode, and Capture Mode
    - Real Time Counter with Separate Oscillator
  - Two Master/Slave SPI Serial Interface
  - One Programmable Serial USART
  - One Byte-oriented 2-wire Serial Interface (Philips I2C compatible)
  - Programmable Watchdog Timer with Separate On-chip Oscillator
  - Interrupt and Wake-up on Pin Change
  - Power-on Reset and Programmable Brown-out Detection
    - Internal Calibrated Oscillator
    - External and Internal Interrupt Sources
  - Six Sleep Modes: Idle, ADC Noise Reduction, Power-save, Power-down, Standby, and Extended Standby
  - 23 Programmable I/O Lines
- Operating Voltage:
  - 1.8 - 5.5V
- Power Consumption at 1MHz, 1.8V, 25°C

- Active Mode: 0.2mA
- Power-down Mode: 0.1µA
- Power-save Mode: 0.75µA (Including 32 kHz RTC)

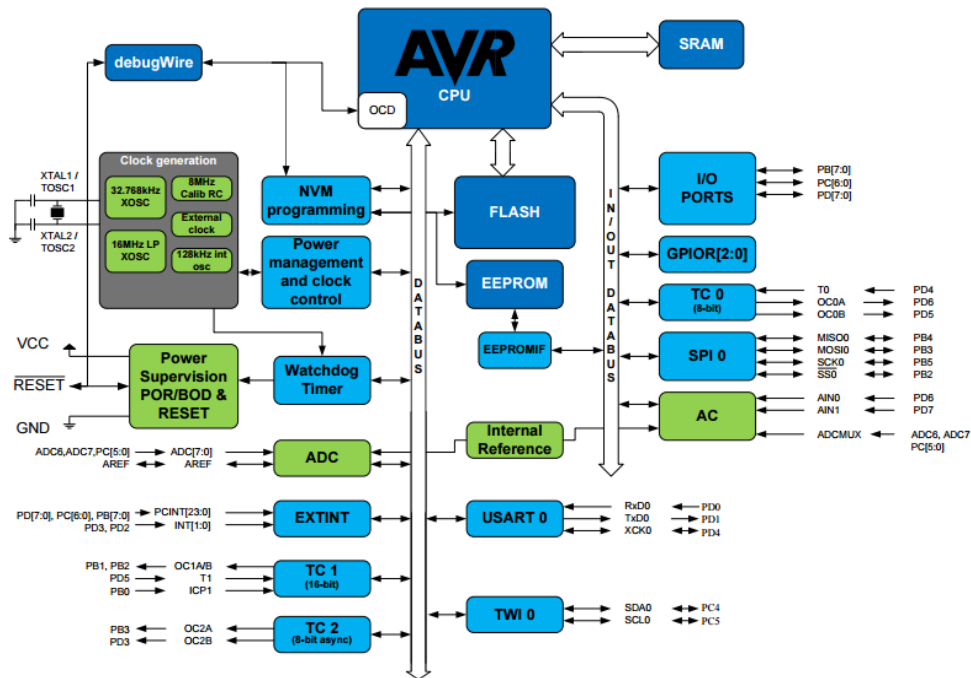


Figure 4-23. ATmega328 block diagram

To avoid the design of another PCB, we are going to use a commercial board. In this case is the Arduino mini v5 (figure 4-24).

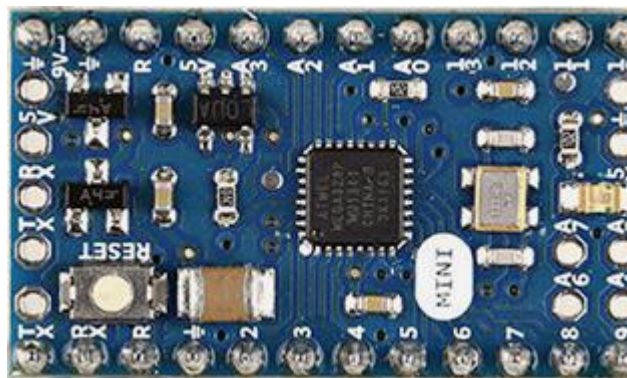


Figure 4-24. Arduino mini v5 board

It has 14 digital input/output pins, 8 analog inputs, and a 16 MHz crystal oscillator. It can be programmed with the USB Serial adapter or other USB or RS232 to TTL serial adapter.

The ATmega328 on the Arduino Mini comes preburned with a bootloader that allows you to upload new code to it without the use of an in-system-programmer. The bootloader communicates using the original STK500.

You can also bypass the bootloader and program the ATmega328 with ICSP (In-Circuit Serial Programming). In this case, we are going to program it by the use of a cable (figure 4-25) that translates the USB communication to serial. This cable have a FT232 chip integrated in its connector.



Figure 4-25. USB to serial cable converter

Another advantage of the use of a commercial Arduino board is the possibility of the use on the Arduino IDE. The open-source Arduino Software (IDE) makes easy to write code and upload it to the board.

It is also possible to use the libraries already done. Libraries provide extra functionality for use in sketches, e.g. working with hardware or manipulating data. Because libraries are uploaded to the board with the sketch, they increase the amount of space it takes up. Some libraries are included with the Arduino software. Others can be downloaded from a variety of sources or through the Library Manager.

#### 4.2.10. Sensors

In order to calibrate the Wheatstone bridge, some sensors has been incorporate in the circuit.

- Low voltage

As is said before, the bridge ADC is a very fast and 12 bits precision chip. But to check if the voltage is correct, the 10 bits ADC of the microcontroller is far enough.

The circuit to monitor this voltage is formed by resistors R33 and R34 as is shown in figure 4-26.

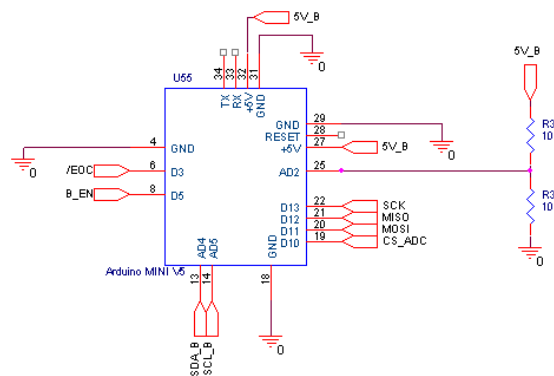


Figure 4-26. Low voltage sensor

- Temperature

Because the bridge is sensing over an aluminium frame, it is sensible to temperature due to metal expansion. To know the temperature is basic to calibrate the force sensor. In this case, the temperature sensor implemented is the MCP9800 by Microchip Technology Inc.'s (figure 4-27).

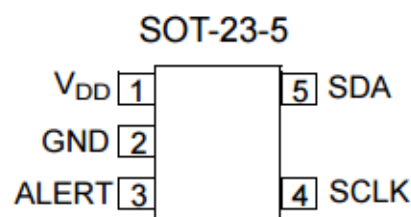


Figure 4-27. Temperature sensor

Microchip MCP9800/1/2/3 family of digital temperature sensors converts temperatures between  $-55^{\circ}\text{C}$  and  $+125^{\circ}\text{C}$  to a digital word. They provide an accuracy of  $\pm 1^{\circ}\text{C}$  (maximum) from  $-10^{\circ}\text{C}$  to  $+85^{\circ}\text{C}$ . The MCP9800/1/2/3 family comes with user-programmable registers that provide flexibility for temperature sensing applications. The register settings allow user-selectable 9-bit to 12-bit temperature measurement resolution, configuration of the power-saving Shutdown and One-shot (single conversion on command while in Shutdown) modes and the specification of both temperature alert output and hysteresis limits. When the

temperature changes beyond the specified limits, the MCP9800/1/2/3 outputs an alert signal. The user has the option of setting the alert output signal polarity as an active-low or active-high comparator output for thermostat operation, or as temperature event interrupt output for microprocessor-based systems. This sensor has an industry standard 2-wire, I2C with the address: 0x48. [31]

- Inclination

With respect to the calibration process, the orientation of the sensor is basic as will be explained in the Calibration section. Then, an inclination sensor has been implemented. The chosen device is the 3-axis NXP Semiconductors MMA8451Q (figure 4-28).

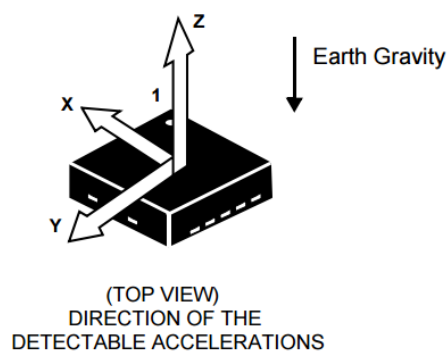


Figure 4-28 3-axis accelerometer

The MMA8451Q is a smart, low-power, three-axis, capacitive, micromachined accelerometer with 14 bits of resolution. This accelerometer is packed with embedded functions with flexible user programmable options, configurable to two interrupt pins. Embedded interrupt functions allow for overall power savings relieving the host processor from continuously polling data. There is access to both low-pass filtered data as well as high-pass filtered data, which minimizes the data analysis required for jolt detection and faster transitions. The device can be configured to generate inertial wakeup interrupt signals from any combination of the configurable embedded functions allowing the MMA8451Q to monitor events and remain in a low-power mode during periods of inactivity. The MMA8451Q is available in a 16-pin QFN, 3 mm x 3 mm x 1 mm package. [32]

As the package is QFN type, an Adafruit commercial board has been incorporated (figure 4-29) at the PCB board.

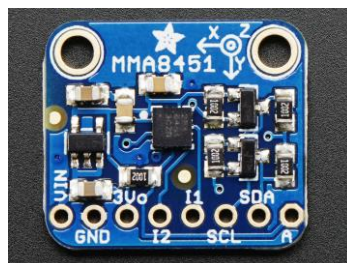


Figure 4-29. Adafruit module

#### 4.2.11. Supply

Once all the components are known (Table 10), it is possible to calculate the current consumption that the sensor will draw from the USB port.

Component	Current per component	Nº of Devices	Total per device
ISL60002	350 nA	1	350 nA
LED's	10 mA	3	30 mA
MAX11628	50 mA	1	50 mA
AtMega328	0.2 mA	1	0.2 mA
Voltage divisor	0.25 mA	1	0.25 mA
MMA8451	0.165 mA	1	0.165 mA
OPA336	20 $\mu$ A	8	160 $\mu$ A
AD5254	5 $\mu$ A	2	10 $\mu$ A
AD8293G	1 mA	8	8 mA
MCP4728	800 $\mu$ A	2	1.6 mA
AD5171	10 $\mu$ A	1	10 $\mu$ A
ADG802	1 nA	1	1 nA
Bridge @4V	150 mA	1	150mA
NVC4274	20 mA	1	20 mA
MCP9800	200 $\mu$ A	1	200 $\mu$ A
<b>TOTAL</b>			<b>260.595 mA</b>

Table 10 – Current consumption

As the USB standard specifications allows to supply until 500 mA, there is no problem to use it for this force sensor.

#### 4.2.12. Timing

Assuming that the force sensor is already power-up and the DAC's are in working condition, the time consumed by every device is:

- Wheastone bridge excitement

To excite the Wheastone Bridge it is necessary to switch on the switch bridge, and this takes 35ns.

There are low pass filters at the instrumentation amplifiers (figure 4-30) to avoid the interference of high frequency signals. This filters are tuned to 150Hz because the required cut off frequency is 100Hz as is said in section 1.1. Then the values of these capacitors and resistors are 220nF and 4700  $\Omega$  respectively.

Using the formula  $V_c = V * (1 - e^{-\frac{t}{R \cdot C}})$ , the time to rise from 0 to 99% of the output of this low pass filters, is 4.761ms. This value will not be taken into account for maximum samples per second performance.

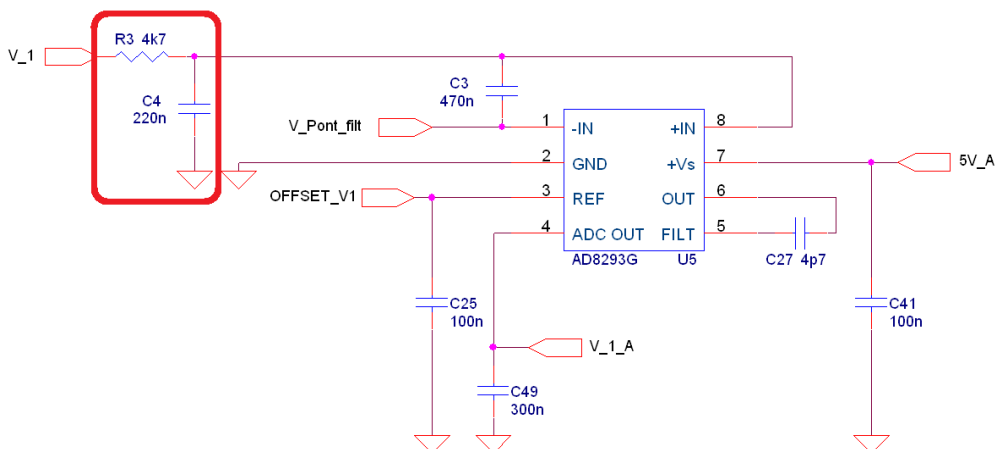


Figure 4-30. Low pass filter input



- Bridge reading

For the bridge reading, it is necessary four different parts as it is shown in figure 4-21.

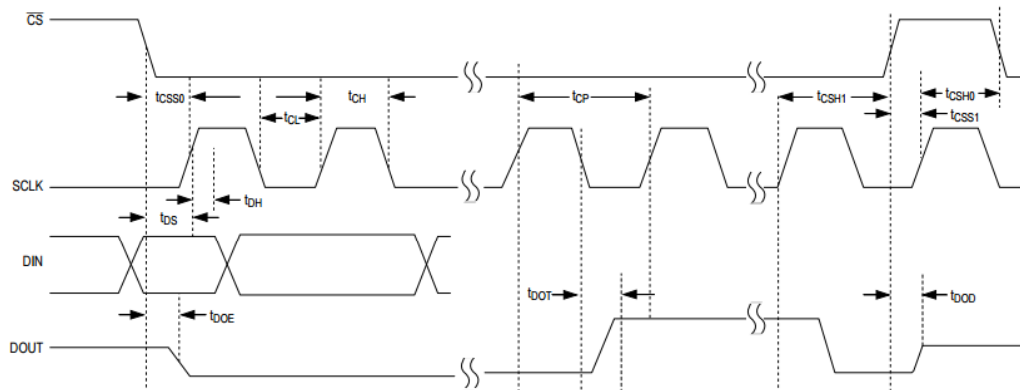
In Clock Mode 10 Timing, it is necessary fall the /CS pin, and this takes 40ns (figure 4-31), secondly, it is sent a Conversion byte, and this takes 2µs for sending 8 bits at a frequency of 4Mhz.

As it is explained in section 4.6.2, the reading time of the 8 channels is 30.592µs without sampling averaging.

Then, to send the reading data, it is necessary to rise and fall the /CS pin between bytes, which is 80ns.

The total time is:

$$T_t = \text{fall CS} + \text{Conversion byte} + \text{Conversion time} + \text{fall CS} + 16 * (\text{send byte} + \text{rise CS} + \text{fall CS}) = 40\text{ns} + 2\mu\text{s} + 30.592\mu\text{s} + 40\text{ns} + 16 * (2\mu\text{s} + 40\text{ns} + 40\text{ns}) = 491.552\mu\text{s}$$



PARAMETER	SYMBOL	CONDITIONS	MIN	TYP	MAX	UNITS
SCLK Clock Period	t <sub>CP</sub>	Externally clocked conversion	208			ns
		Data I/O	100			
SCLK Pulse Width High	t <sub>CH</sub>		40			ns
SCLK Pulse Width Low	t <sub>CL</sub>		40			ns
SCLK Fall to DOUT Transition	t <sub>DOT</sub>	C <sub>LOAD</sub> = 30pF			40	ns
CS Rise to DOUT Disable	t <sub>DOD</sub>	C <sub>LOAD</sub> = 30pF			40	ns
CS Fall to DOUT Enable	t <sub>DOE</sub>	C <sub>LOAD</sub> = 30pF			40	ns
DIN to SCLK Rise Setup	t <sub>DS</sub>		40			ns
SCLK Rise to DIN Hold	t <sub>DH</sub>		0			ns
CS Low to SCLK Setup	t <sub>CSS0</sub>		40			ns
CS High to SCLK Setup	t <sub>CSS1</sub>		40			ns
CS High After SCLK Hold	t <sub>CSH1</sub>		0			ns
CS Low After SCLK Hold	t <sub>CSH0</sub>		0		4	µs
CNVST Pulse Width Low	t <sub>CSPW</sub>	CKSEL = 00		40		ns
		CKSEL = 01		1.4		µs
CS or CNVST Rise to EOC Low (Note 8)		Voltage conversion			7	µs
		Reference power-up			65	

Figure 4-31. MAX11628Timing diagram

### -Matrix process

The maximum number of multiplications to resolve by the transformation matrix, is 8 reads per 6 constants, so 48 multiple of floats is the worst case. With a small program (Table 11) is possible to measure the time that the microcontroller takes to do a float multiplication, and this time is  $7.112\mu\text{s} * 48 = 341.376\mu\text{s}$ .

```

Serial.print(F(" multiply float      : "));
f1 = 3.24;
f2 = 1.25;
delay(70); // Allow the Serial text to be transmitted
m=millis();
for (i=0; i<2; i++)
{
  for (j=0; j<10000; j++)
  {
    f1 *= f2;   f1 *= f2;   f1 *= f2;   f1 *= f2;
    f1 *= f2;   f1 *= f2;   f1 *= f2;   f1 *= f2;
    f1 *= f2;   f1 *= f2;   f1 *= f2;   f1 *= f2;
    f1 *= f2;   f1 *= f2;   f1 *= f2;   f1 *= f2;
    f1 *= f2;   f1 *= f2;   f1 *= f2;   f1 *= f2;
  }
}
n=millis();
d = ((float)n - (float)m) / ((float)i * (float)j);
d *= 1000.0;
d -= overhead;
d /= 20.0;
Serial.print (d,3);
Serial.println (F(" us"));

```

Table 11 – Float multiplication speed test program

### -Serial transmission

To transfer three forces and three torques at 12 bites per value, it is necessary to send 72 bits, and at a baud rate of 115200 bits/s that is the maximum for this microcontroller, it is necessary to wait  $625\mu\text{s}$ .

So, the total time needed to read the bridge and send the results, is  $1457.924\mu\text{s}$  that means that it is possible to have a sampling rate of 685 samples per second, almost 7 times the sample speed required in the sensor specifications.

#### 4.2.13. PCB

The schematics (Annex A) and the PCB (Annex B) has been designed with OrCad\_v10.5 software and CircuitCAM, and milled with a LPKF PCB mill.

Due to the small space of the sensor and the number of components, it has not been possible to do it in just one PCB. Then, two layers PCB's have been designed, named as A and B (figure 4-32), that are attached in tandem configuration.

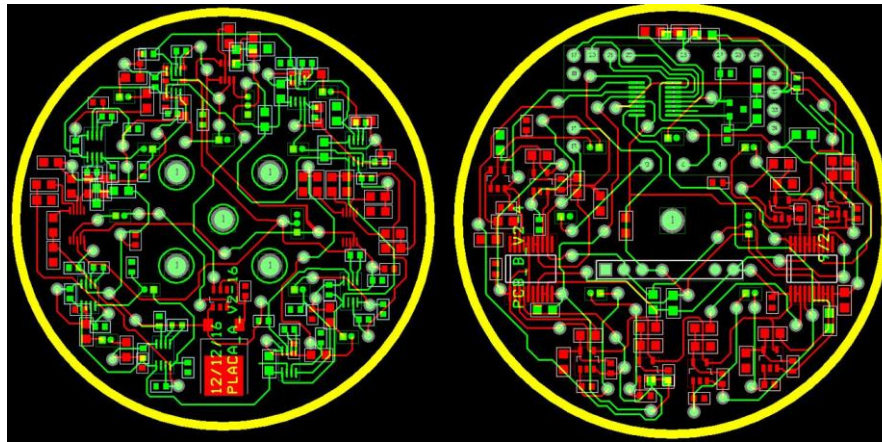


Figure 4-32. PCB A and B

To avoid soldering QFN components, two more commercial PCB's (microcontroller and the inclination sensor) have been attached too over the other ones (figure 4-33).

Ground analog and digital nets have been separated in PCB ground sections with only one star point connecting the two ground systems. For lowest noise performance, the ground return to the star ground's power supply is low impedance and as short as possible. Digital signal traces are far away from sensitive analog and reference inputs. High-frequency noise in the power supply (VDD) could influence the proper operation of the ADC's fast comparator, so VDD is decoupled to the star ground by a network of two parallel capacitors, 0.1 $\mu$ F and 4.7 $\mu$ F, located as close as possible to the ADC MAX11628 power supply pin.

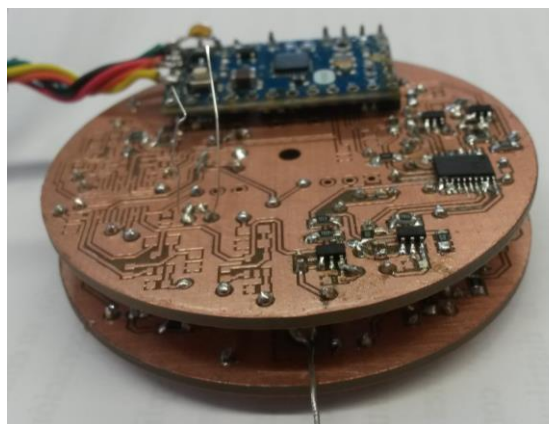


Figure 4-33. PCB's attachments

## 5. Software program

### 5.1. Introduction

To test the force sensor a very basic software is used. As can it be seen in figure 5-1, the flowchart starts initializing the digital communications with two standard libraries. Then there are three functions specifically made for this project. First a device test is done to check if every device has communication, next, a function to initialize and calibrate the two DACs, and after that, a function that initializes and calibrates the RDAC of the bridge balancing, and also, initializes the RDAC of the gain amplifier.

Depending if the sensor is in calibration or operation mode, two different programs are executed. In calibration mode, precision is preferred to speed, and different sensors are read and data is transmitted to the PC to perform the calibration process. In operation mode, the matrix calculation to transform raw read data to force units is also done.

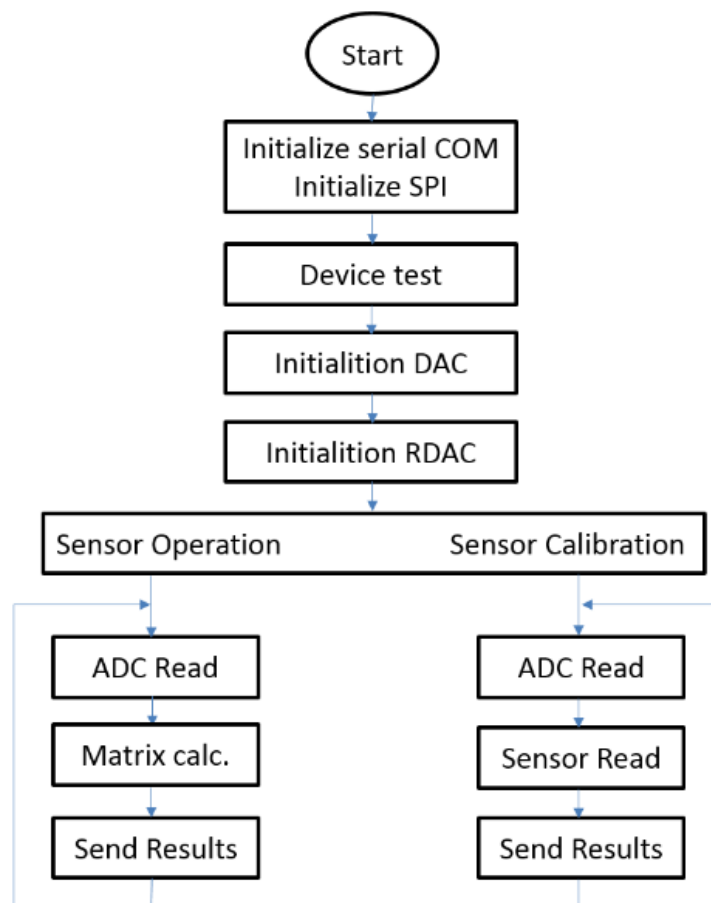


Figure 5-1. Software Flowchart

## 5.2. Functions

### - Start

First at all, the different libraries must be included in the main program. This libraries are for I2C communication, DAC's MCP4728, SPI protocol communication, temperature sensor MCP 9800, and orientation sensor.

```
#include <Wire.h>           // initialize I2C communication protocol
#include "mcp4728.h"        // initialize DACs library
#include <SPI.h>            // initialize SPI communication protocol
#include orientation sensor // initialize orientation sensor library
```

### - Initialization of serial COM

A library provided by the Arduino IDE is used to initialize the serial COM to a baud rate of 115200 bits per second (baud).

```
Serial.begin (115200); // initialize serial interface to PC
```

### - Initialization of SPI

It is necessary to set the SPI clock divider relative to the system clock, and this is done also with an Arduino IDE library. On AVR based boards, the dividers available are 2, 4, 8, 16, 32, 64 or 128. The default setting is SPI\_CLOCK\_DIV4, which sets the SPI clock to one-quarter the frequency of the system clock (4 Mhz for the boards at 16 MHz as the used one).

```
SPI.begin();
SPI.setClockDivider (SPI_CLOCK_DIV4); // SPI speed: CLK DIV4
```

### - Device test

First test is to check if every I2C device has a properly communication by sending a communication request. These devices and addresses are AD5171 in 0x2C, MCP9800 in 0x48, two MCP4728 in 0x60 and 0x61 and AD5254 in 0x2F.

```
Wire.beginTransmission(0x2C); // Calling to the AD5171 I2C address
error = Wire.endTransmission(); // Receiving answer from AD5171
if (error == 0) { // If answer is 0, everything is OK
  Serial.print("AD5171 OK\n"); // Showing that AD5171 is communicating
}
else if (error==4) { // If answer is 4, there is an error
  Serial.print("AD5171 ERROR\n"); // Showing that there is an error on AD5171
}
```

The second device test, is to check the two DACs MCP4728. This test checks the registers of the output voltages, the gain, the power down setting and the value. This is done for every channel and for volatile and nonvolatile EEROM registers.

```
Serial.print("Device ID = ");
Serial.println(dac1.getId(), DEC); // serial print of Identification Device value
Serial.println("DAC Vref Gain PowerDown Value");
for (int channel=0; channel <= 3; channel++) { // check every single channel
  Serial.print("DAC"); // volatile registers
  Serial.print(channel,DEC);
  Serial.print(" ");
  Serial.print(dac1.getVref(channel),BIN); // Vref value
  Serial.print(" ");
  Serial.print(dac1.getGain(channel),BIN); // Gain value
  Serial.print(" ");
  Serial.print(dac1.getPowerDown(channel),BIN); // Power Down setting
  Serial.print(" ");
  Serial.println(dac1.getValue(channel),DEC); // DAC channel value
  Serial.print("EEPROM"); // nonvolatile registers
  Serial.print(channel,DEC);
  Serial.print(" ");
  Serial.print(dac1.getVrefEp(channel),BIN); // Vref value
  Serial.print(" ");
  Serial.print(dac1.getGainEp(channel),BIN); // Gain value
  Serial.print(" ");
  Serial.print(dac1.getPowerDownEp(channel),BIN); // Power Down setting
  Serial.print(" ");
  Serial.println(dac1.getValueEp(channel),DEC); // DAC channel value
}
```

To check that the temperature sensor is working properly, the sensor reads it and shows the temperature data. Two bytes are requested for full resolution temperature sensor.

```

Wire.beginTransmission(0x48);    // transmit to I2C
Wire.write(0b00000000);         // sends one byte.
Wire.endTransmission();         // stop transmitting
Wire.requestFrom(I2C_address, 2); // request 2 bytes from address.
while(Wire.available())         // slave may send less than requested
{
  int temp1 = Wire.read();       // receive a byte as integer
  int temp2 = Wire.read();       // receive a byte as integer
  int a = temp1 <<1;             // bitshift 1 to the left to allow for 9bit data from temp
//sensor
int b = temp2 >>7;               //bitshift 7 to the right to allow for 9 bit data from temp
//sensor
int tempRaw = a|b;              // define int rawtemp as the combination of integer a and b
// 0.5 = 2^-1 since T = C x 2^n where c is the binary code value, and n is
// dependent on //resolution used. tempC is temperature in Celsius
float tempC = tempRaw * 0.5 ;

```

A commercial library has been used for orientation sensor.

```

accel.update();

Serial.print("x:");

Serial.print(accel.x());

Serial.print(" y: ");

Serial.print(accel.y());

Serial.print(" z: ");

Serial.println(accel.z());

```

#### - Initialization of DACs

Because there are two DACs, and there are no address pin, the I2C address must be changed by writing the optional address in a MCP4728 register. Once we have two different addresses, the two DACs must be addressed correctly in the library as Device ID 0 and 1.

Then, VDD, Gain, Vref and PowerDown registers must be set.

```

mcp4728 dac0 = mcp4728(0); // instantiate mcp4728 object, Device ID = 0
mcp4728 dac1 = mcp4728(1); // instantiate mcp4728 object, Device ID = 1
dac1.begin();                // initialize i2c interface
dac1.vdd(5000);              // VDD(mV) for correct conversion between LSB and Vout
dac1.setGain(0, 0, 0, 0);    // gain of internal voltage reference (0 = gain x1)
dac1.setVref(1,1,1,1);      // internal voltage reference (2.048V)

```

```
dac1.setPowerDown(0, 0, 0, 0); // set Power-Down (0 = Normal)
```

#### - Initialization of RDACs

As the RDAC is a read only device, the communication is very fast. We only have to write the I2C address and the value. The AD5171 has only 64 steps, so 31 is the medium value.

```
Wire.beginTransaction (byte(0x2C)); // transmit to device 0x2C
Wire.write(byte(0x00)); // sends instruction byte
Wire.write(31); // sends potentiometer value byte
```

For the AD5254, the number of steps is 256. But in this case, as every device have 4 resistor channels, first we have to indicate which one we have to change, and this is done with the instruction byte. Then we can send the value required.

```
Wire.beginTransaction (byte(0x2F)); // transmit to device 0x2F
Wire.write( byte(0x00)); // sends instruction byte (channel)
Wire.write( byte(0xFF)); // sends potentiometer value byte
```

#### - ADC Reading

In Figure 4-21, it is shown the timing for analog reading of the ADC. To communicate with a SPI device, first we have to clear the CS pin of the desired chip. In this case it is done by port manipulation because is much faster than a C instruction. Then two bytes can be read, and after setting the CS bit, the two read bytes must be operated to obtain a full resolution result.

```
PORTB &= B11111011; // Reading CH0
SPI.transfer((canal_0>>8) & 0xff); // Clear pin CS to 0
msb0 = SPI.transfer(canal_0 & 0xff) & B00001111; // Send data
lsb0 = SPI.transfer(0x00); // Reading msb byte
PORTB |= B00000100; // Reading lsb byte
v_ch1=msb0 <<8 | lsb0; // Sets pin CS to 1
// OR instruction
```



#### - Sensor Reading

To show the values of the temperature and orientation sensors, we use the same instructions as in device test explained before.

#### - Matrix calculations

Every force and torque is calculated multiplying the channels that changes when the force/torque is applied, with a matrix that results from the calibration.  $M_{x_x}$  are the values of the calibration matrix.

```
FX = (sensorValue0 * M_1_1) + (sensorValue1 * M_1_2);
```

#### - Send results

All results are sent from sensor to PC via serial communication.

```
Serial.print("F_X: ");  
Serial.print(Force_X);
```

## 6. Results

### 6.1. Introduction

After receiving signals from a sensor, these signals need to be processed. The acceptable and accurate process of these signals requires: (a) full knowledge regarding the operation of the sensors and nature of signals, (b) posteriori knowledge regarding the received signals, and (c) information about the dynamic and static characteristics of the sensing systems [34].

Static characteristics are those that can be measured after all transient effects have been stabilized to their final or steady state values. Static characteristics relate to issues such as how a sensor's output change in response to an input change, how selective the sensor is, how external or internal interferences can affect its response, and how stable the operation of a sensing system can be

A sensing system response to a dynamically changing measurand can be quite different from when it is exposed to time invariable measurand. In the presence of a changing measurand, dynamic characteristics can be employed to describe the sensing system's transient properties. They can be used for defining how accurately the output signal is employed for the description of a time varying measurand. These characteristics deal with issues such as the rate at which the output changes in response to a measurand alteration and how these changes occur.

The reason for the presence of dynamic characteristics is the existence of energy-storing elements in a sensing system. They can be produced by electronic elements such as inductance and capacitance, mechanical elements such as vibration paths and mass, and/or thermal elements with heat capacity. The most common method of assessing the dynamic characteristics is by defining a system's mathematical model and deriving the relationship between the input and output signal. Consequently, such a model can be utilized for analysing the response to variable input waveforms such as impulse, step, ramp, sinusoidal, and white noise signals.

In this project, only static characteristics will be tested due the lack of instruments and installations. Furthermore, only the channels referred to the Z axis has been tested due to the amount of measures. All other channels behaviour is similar to the tested ones.

Data received by the computer, has been processed with Microsoft Excel.

## 6.2. Setup

In order to do the force/torque measurements, different setups must be used. For Z (figure 6-1), X and Y forces (figure 6-2), a weight must be placed aligned with each axis of the sensor.

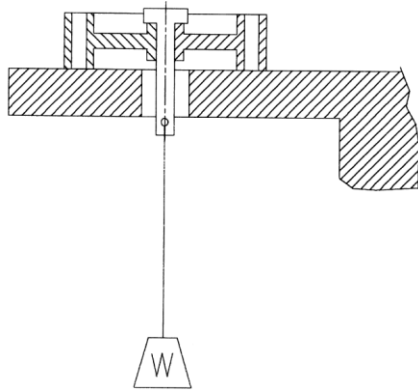


Figure 6-1. Z force setup

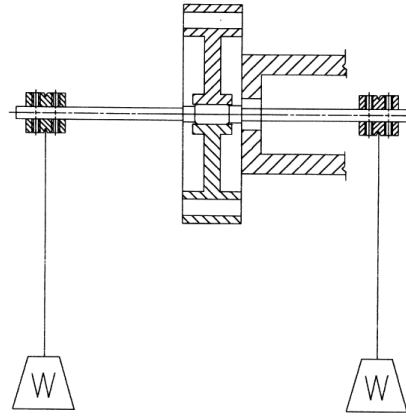


Figure 6-2. X and Y force setup

For this test we have used 8 different weights of 146, 364, 790, 1114, 1656, 2020 and 2161 grams, which corresponds to 1.43, 3.56, 7.74, 10.91, 16.22, 19.79 and 21.17 Newtons respectively.

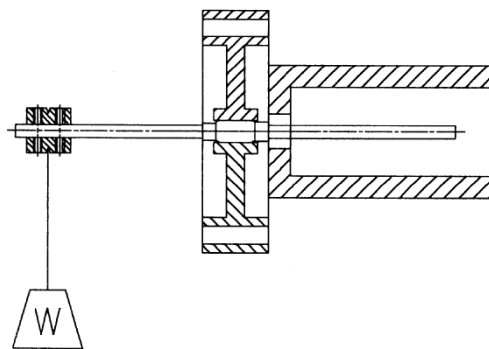


Figure 6-3. X and Y torque setup

For X and Y (figure 6-3) and Z (figure 6-4) torque measurements, the weight is hanged at one side of the sensing elements. The measurement of the weights and the distance where they are situated, are critical in the final results.

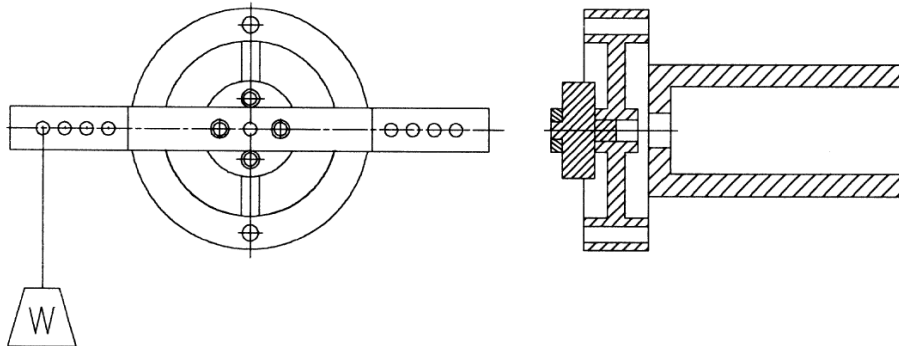


Figure 6-4. Z torque setup

### 6.3. Sensor characterization

#### 6.3.1. Channel response

The first test is to check if every channel is working properly. Once the sensor is working, the signal of every channel has a similar voltage thanks to the auto-offset done with the DAC's. But to show that the sensor is working properly, a manual offset has been added to see every channel response (Figure 6-5).

The colour/channel code for next figures are: Blue = CH0, Red = CH1, Green = CH2, Yellow = CH3, Magenta = CH4, Grey = CH5, Cyan = CH6 and Black = CH7.

The following tests has been made with a total gain of 666, and no averaging results.

First analysis is to test the response of the channels. In this case, a weight of 1Kg (a force of 9.8N) has been hanged, and suddenly removed. First test is in Z axis. In figure 6-6, four channels are changing notoriously: cyan, yellow, black and green.

Then, the same test is done over Y axis (Figure 6-7), where the changing channels are the grey and the pink. And finally, is done over the X axis (Figure 6-8), where blue and red channels are changing.

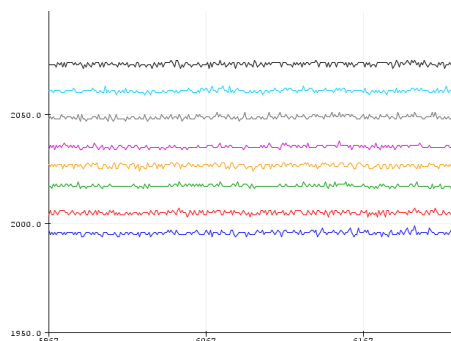


Figure 6-5 Channels outputs

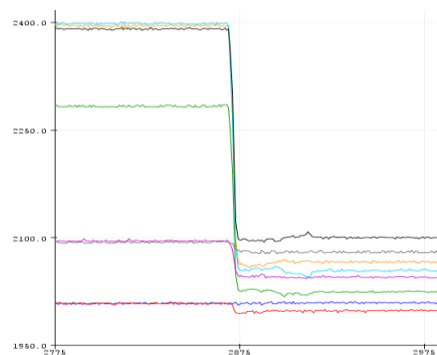


Figure 6-6 force in Z axis

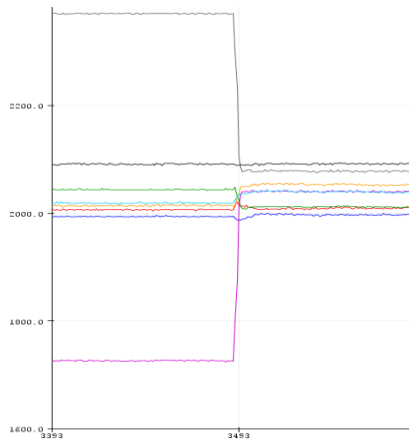


Figure 6-7 force in Y axis

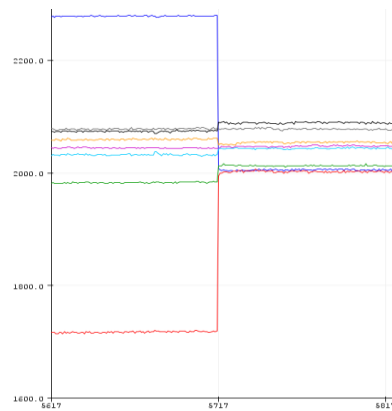


Figure 6-8 force in X axis

From this graphs, we can conclude that the sensing deformation is very selective depending on the direction of the force. Only the channels that must vary their value do it, and the other ones remain in the initial value. The mechanical design and strain gauges implementations are corrects. We also can see that the values are very stable along the time.

### 6.3.2. Accuracy

Accuracy of a sensing system represents the correctness of its output in comparison to the actual value of a measurand. To assess the accuracy, either the system is benchmarked against a standard measurand or the output is compared with a measurement system with a superior accuracy. This characteristics can be only evaluated after the sensor calibration which will be done in next section.

### 6.3.3. Precision

Precision represents the capacity of a sensing system to give the same reading when repetitively measuring the same measurand under the same conditions. The precision is a statistical parameter and it can be assessed by the standard deviation (or variance) of a set of readings of the system for similar inputs. This test (figure 6-9) has been made with 4000 samples of each. This test has been made with an averaging of 100 samples per channel.

Channel 2 and 5 (green and grey colour) have a precision higher than channel 1 (red colour). This can be due to the noise of this channel.

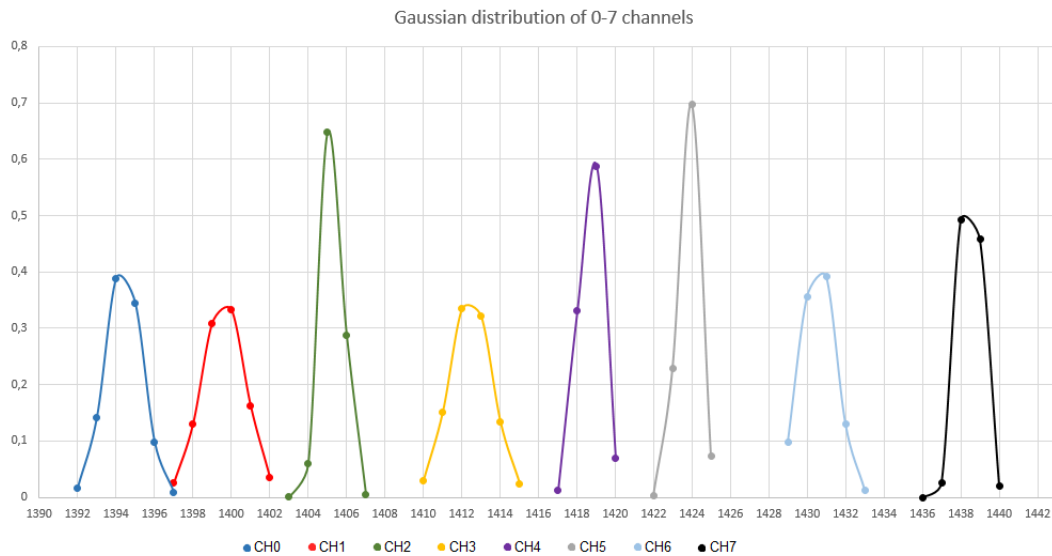


Figure 6-9 Precision Gaussian distribution

Although all channels have different precision, we can conclude that even the channel 3 (in yellow) it only has a variation of two bits with respect the real value. This difference in channel precision can be caused by some imperfections in the sensor milling or in the bonding of the strain gauges. This is not important because all the values will be compensated after the calibration.

### 6.3.4. Repeatability

When all operating and environmental conditions remain constant, repeatability is the sensing system’s ability to produce the same response for successive measurements. Repeatability is closely related to precision. Both long-term and short-term repeatability estimations can be important for a sensing system.

This test has been made by applying a 9.8 N force in Z axis (channel 2), taking 50 samples, taking out the force and taking 50 more samples. This is repeated for 4 times with a time between series of samples of 1 minute to stabilize the force (figure 6-10).

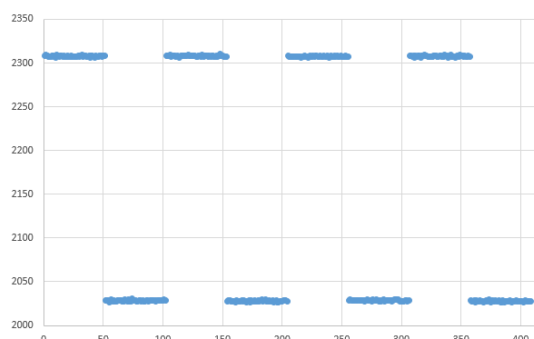


Figure 6-10. Repeatability test

The Gaussian distribution can be seen in figure 6-14. Left chart is with no load, and the right one is with an applied force of 9.8N.

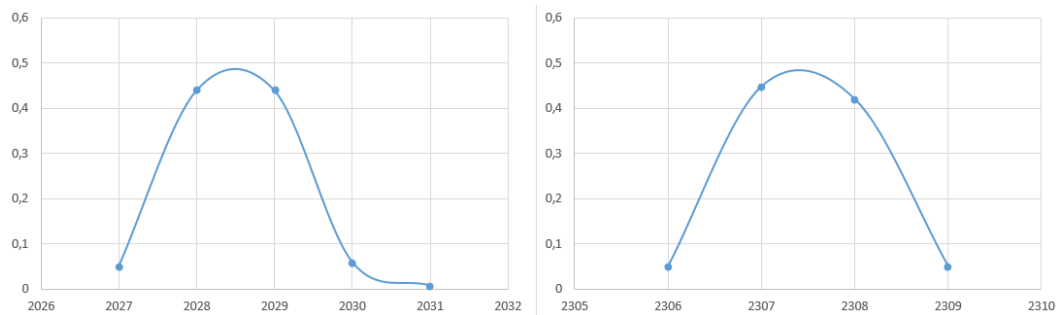


Figure 6-11. Repeatability Gaussian distribution

From figure 6-11 we can see that the Gaussian distribution is similar than the test done with static force, this means that the repeatability is very good. The same force gives the same value in the sensor, even if the force is varied along the time.

### 6.3.5. Drift

Drift is observed when a gradual change in the sensing system’s output is seen, while the measurand actually remains constant. Drift is the undesired change that is unrelated to the measurand. It is considered a systematic error, which can be attributed to interfering parameters such as mechanical instability, temperature instability, contamination, or the sensor’s materials degradation. It is very common to assess the drift with respect to a sensor’s baseline, which is the output value when the sensor is not exposed to a stimulus. Logically, the baseline should remain constant for a sensor with no drift.

In the test (figure 6-12) it has been taken one measurement every 3 minutes for a period of 12 hours. The four channels implied in Z force are in yellow, blue, green and red, and in black we can see the room temperature value. To avoid noise, every sample in the graph, is the average of 24 samples. The oscillations of the graph, can be caused by temperature changes in the room during the test. It started at 18pm, and finished at 6am of the next day, and as it is shown in the graph, the channels values raise while the temperature room falls. Once the sensor is calibrated with the temperature sensor, this oscillations will be mainly suppressed.

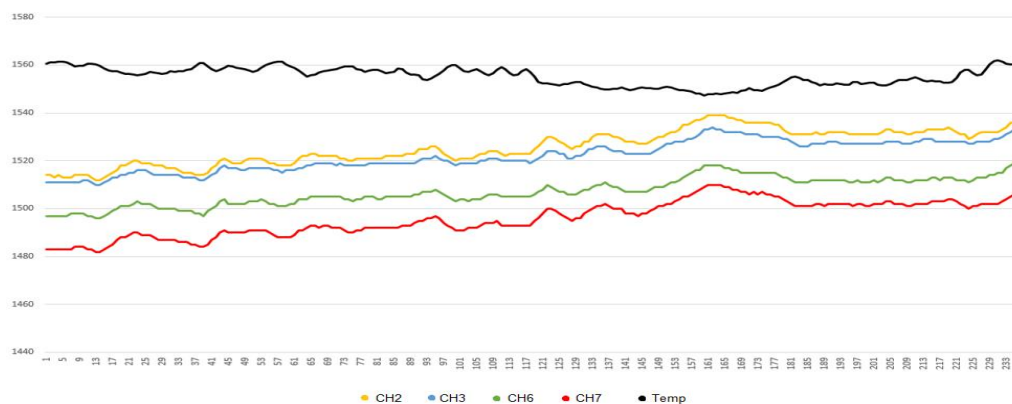


Figure 6-12 Drift test

### 6.3.6. Noise

The unwanted fluctuations in the output signal of the sensing system, when the measurand is not changing, are referred to as noise. The standard deviation value of the noise strength is an important factor in measurements. The mean value of the signal divided by this value gives a good benchmark, as how readily the information can be extracted. As a result, signal-to-noise ratio (S/N) is a commonly used figure in sensing applications. It is defined as S/N ratio, where S is the power of the signal, and N is the power of the noise.

As it is shown in figure 6-13 (left), the average voltage of this channel is 1.63V, and

the average noise is about 10mV. Then, the S/N is  $20 \log \frac{1.63V}{10mV} = 44.24dB$ .

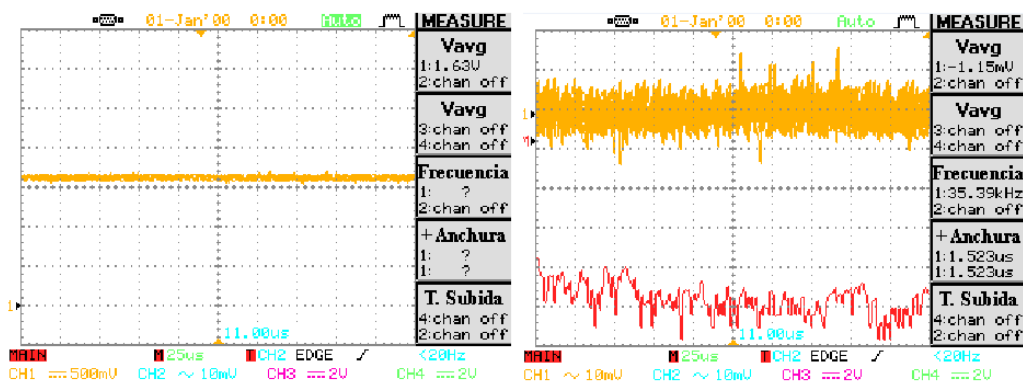


Figure 6-13 Noise test

Noise can be caused by either internal or external sources. Electromagnetic signals such as those produced by transmission/reception circuits and power supplies, mechanical vibrations, and ambient temperature changes are all examples of external noise, which can cause systematic error. In figure 6-13 (right), we can notice that the FFT of the noise (red line in right figure), has no fundamental frequency.

The input-inferred noise could be reduced by placing a higher-order low pass filter on the outputs or by reducing the bandwidth of the filter. Of course, one of the penalties for placing a higher-order filter at the outputs is an increase in the number of external components required on the printed circuit board. Likewise, one of the penalties of reducing the filter bandwidth is the increase in the startup/response time of the outputs. In this project, a first order low pass filter has been implemented as is explained in chapter 4.2.6.

To reduce the noise level is possible decreasing the number of bits in the ADC. In figure 6-14 is shown the Gaussian distribution of three group of samples, ADC of 10 bits in blue, ADC of 11 bits in red and ADC of 12 bits in yellow. This test has been done with a pack of 2500 samples.



Another advantage of reducing the number of bits, is that the time of conversion is also shorter: 6us for 10 bits, 16us for 11 bits and 33us for 12 bits.

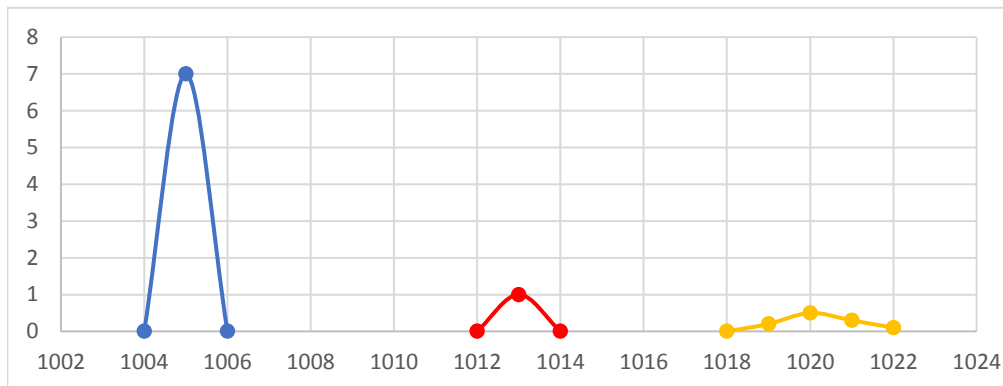


Figure 6-14 Noise vs. N\_bits

Another technique that can be used to reduce noise is over-sampling and averaging. In most applications, digital data from the sensor are used in computations or in control functions. The optimal sampling rate will depend on the particular application. In figure 6-15 we can see the Gaussian distribution for an averaging of 24 samples in blue colour, 8 samples in red, and no averaging in yellow colour.

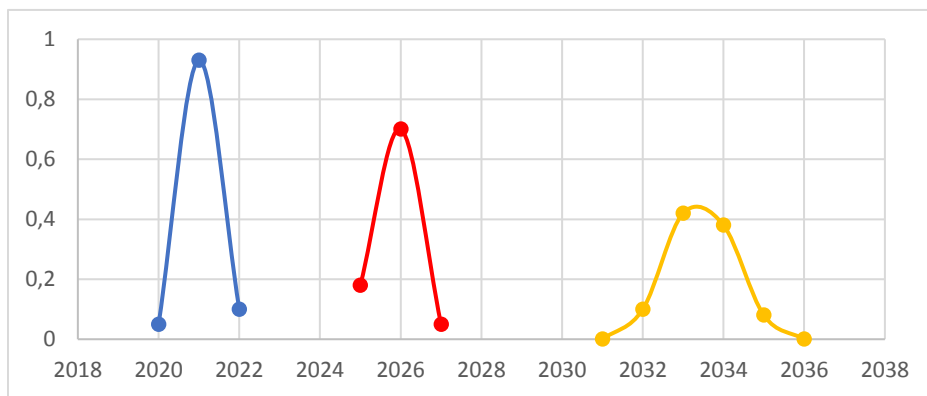


Figure 6-15 Noise vs. Averaging

Oversampling involves sampling a signal using a sampling frequency that is significantly higher than the Nyquist frequency. If multiple samples (N) are taken of the same quantity with a random noise signal, then averaging those samples reduces the noise by a factor of  $1/\sqrt{N}$ .

### 6.3.7. Resolution

Resolution (or discrimination) is the minimal change of the measurand that can produce a detectable increment in the output signal. Resolution is strongly limited by noise in the signal.

When the sensor is working at an ADC resolution of 12 bits, the resolution in X, Y and Z axis is 50mN

### 6.3.8. Measurement Range

The maximum and minimum values that can be measured with a sensing system are called the measurement range, which is also called the dynamic range or span. This range results in a meaningful and accurate output for the sensing system. All sensing systems are designed to perform over a specified range. Signals outside of this range may be unintelligible, cause unacceptably large inaccuracies, and may even result in irreversible damage to the sensor.

Because the noise affects to 1 bit, the minimum detectable force for 2 bits is 98mN, and to avoid the damage of the sensor, the maximum force applied is 21.18N.

### 6.3.9. Response and Recovery Time

When a sensing system is exposed to a measurand, the time it requires to reach a stable value is the response time. It is generally expressed as the time at which the output reaches a certain percentage (for instance, 95 %) of its final value, in response to a step change of the input. The “recovery time” is defined conversely.

As this force sensor arms act as a bending spring, the response and recovery time of the material is much faster than the time required to read the strain gauges values, that is as fast as 1457.924 $\mu$ s as explained in section 4.2.12.

### 6.3.10. Linearity

The closeness of the calibration curve to a specified straight line shows the linearity of a sensor. Its degree of resemblance to a straight line describes how linear a system is.

Only the +z axis measurement has been done. For this test we have used 8 different weights of 146, 364, 790, 1114, 1154, 1656, 2020 and 2161 grams, which in figure 6-16 are situated in X axis converted to Newtons. While in Y axis are the results of the ADC.

As it can be seen, there are four channels that responds to the force applied in Z axis, while the other four, are only slightly affected.

The value of the response characteristics of each channel are shown in the figure 6-16.

From figure 6-16, we have calculated the coefficient of determination (denoted as  $R^2$ ) to have a real value of the linearity.

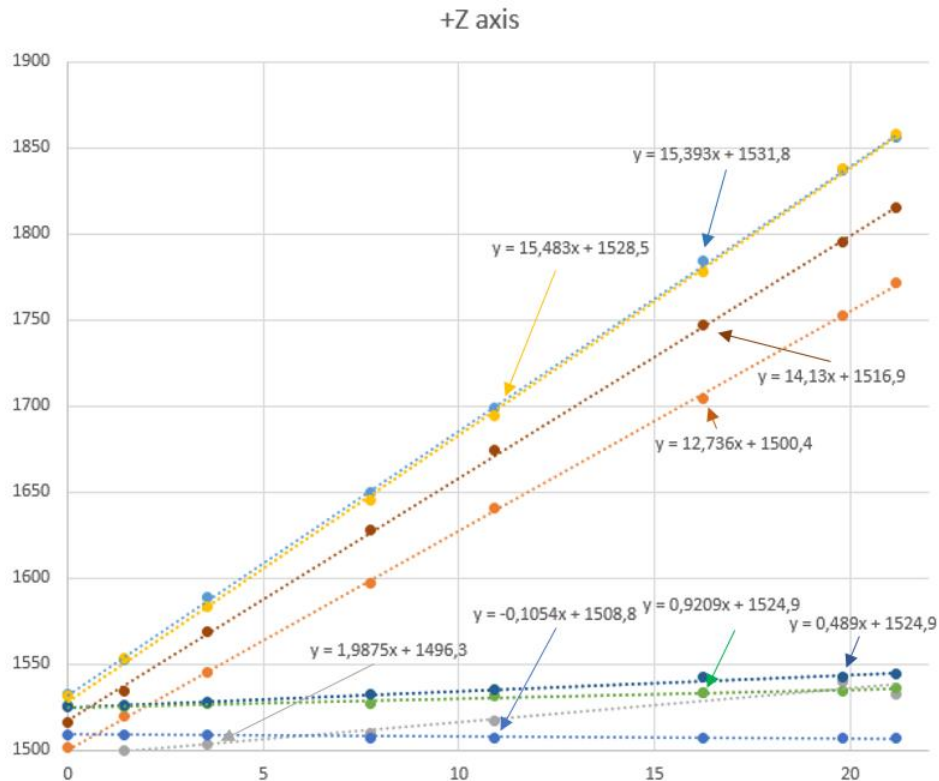


Figure 6-16 Calibration curve in +Z axis

$R^2$  is a statistic that gives some information about the goodness of fit of a model. In regression, the  $R^2$  coefficient of determination is a statistical measure of how well the regression line approximates the real data points. An  $R^2$  of 1 indicates that the regression line perfectly fits the data.

For the channels used for Z axis force sensor, the  $R^2$  are:

$$y = 15,48x + 1528 \Rightarrow R^2 = 0,9993$$

$$y = 15,39x + 1532,1 \Rightarrow R^2 = 0,9998$$

$$y = 14,13x + 1517,2 \Rightarrow R^2 = 0,9996$$

$$y = 12,73x + 1500,5 \Rightarrow R^2 = 0,9997$$

And for the channels that are not affected by the Z axis force, the  $R^2$  are:

$$y = 0,48x + 1525 \Rightarrow R^2 = 0,9485$$

$$y = 0,92x + 1525,1 \Rightarrow R^2 = 0,9796$$

$$y = 1,98x + 1496,4 \Rightarrow R^2 = 0,957$$

$$y = -0,1x + 1508,8 \Rightarrow R^2 = 0,687$$

Except for the last value, the  $R^2$  are very close to 1, so it means that the linearity of each channel is very high.

### 6.3.11. Sensitivity

Sensitivity is the ratio of the incremental change in the sensor's output ( $\Delta y$ ) to the incremental change of the measurand in input ( $\Delta x$ ). The slope of the characteristic curve in figure 6-16, can be used for the calculation of sensitivity.

An ideal sensor has a large and preferably constant sensitivity in its operating range. It is also seen that the sensor eventually reaches saturation, a state in which it can no longer respond to any change. This depends on the mechanical properties of the material used.

As it has been explained before, this sensor have different gain values, but only a value of 667 has been tested.

From figure 6-16, we can see that the incremental change are 15.16x, 15.09x, 13.85x and 12.48x for the sensitive channels, and 0.48x, 0.91x, 1.95x and -0.1x for the insensitive channels.

### 6.3.12. Hysteresis

Hysteresis is the difference between output readings for the same measurand, depending on the trajectory followed by the sensor. Hysteresis may cause false and inaccurate readings.

This test has been performing by applying force to Z axis in positive and negative direction alternatively as can be shown in figure 6-17.

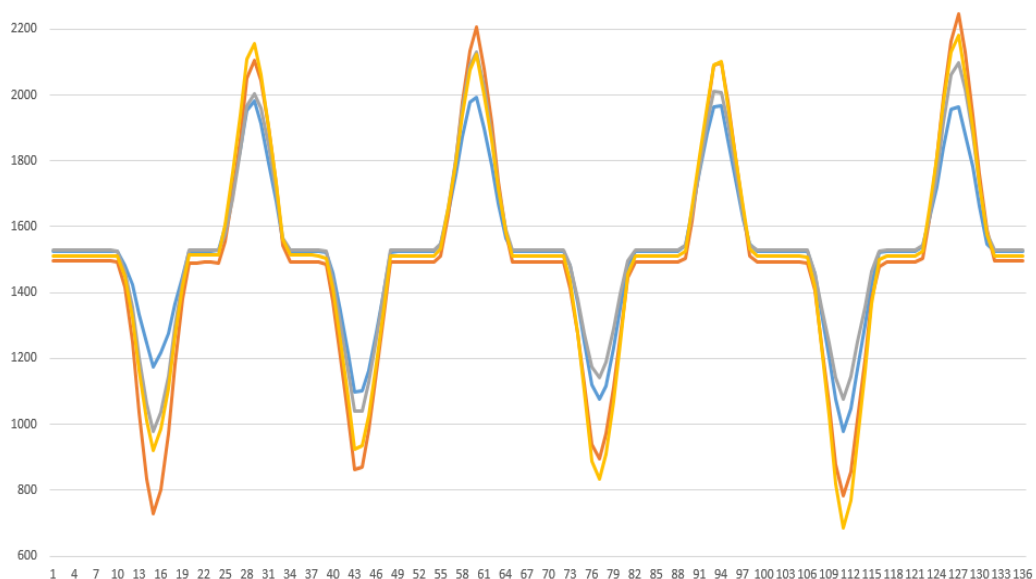


Figure 6-17 Hysteresis test on Z axis

Then, the positive and negative results are deleted, and only the results with no force applied values are left. On figure 6-18 is possible to see that there are not significant difference in values when the forces are released in both directions. So, no hysteresis is present in this sensor in the Z axis.

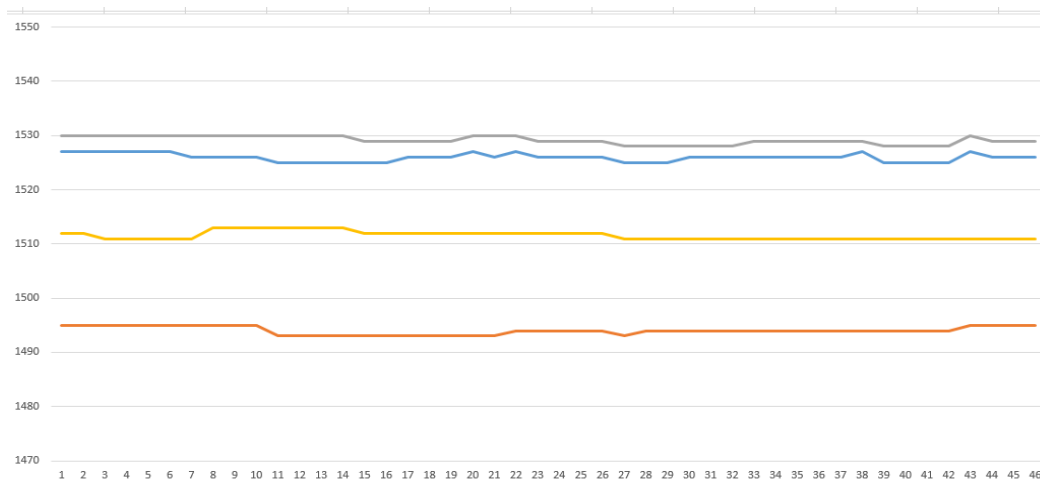


Figure 6-18 Hysteresis result on Z axis

#### 6.4. **Calibration**

Calibration of multi-axis force/torque sensors is a time-consuming ordeal that traditionally requires the precise application of a set of known forces and torques carefully selected to adequately span the range of the sensor. Reduction by least squares, the standard technique of force sensor calibration, requires both the application of a spanning set of precisely known loads and the measurement of associated sensor (e.g. strain gage) values. Although effective, this approach is cumbersome because of the relatively large number of accurate loads that must be applied to the sensor to reduce noise introduced by measurement error; often 12 to 30 or more loads are required to produce a reasonably accurate calibration matrix for a 6-degree-of-freedom (DOF) sensor, even though six are theoretically sufficient. For example, Lord Corporation allows up to 60 loads for their user calibration function. [35]

The calibration procedure determines the measurement uncertainty, and it plays an important role in sensor development for reaching the required measurement specifications.

As the strain gauge sensor transfers forces and torques into voltage signals, calibration factors are required to calculate the acting forces and torques. Because the sensor used is a monolithic structure, forces and torques cause mutual interferences.

### 6.4.1. Matrix

The mean measurement for the six-component force sensor aims to measure the strain registered by gauges attached to an elastic sensor body and to calculate the subsequent applied forces and moments.

Consider the elastic body of a force sensor on which an external force vector  $\vec{F} = (F_x, F_y, F_z, M_x, M_y, M_z)^T$  acts upon a predetermined point [36].

The forces and moments are measured by eight strain gauge bridges at given points on the elastic body thereby yielding the strain signal vector  $\vec{S} = (S_0, S_1, S_2, S_3, S_4, S_5, S_6, S_7)^T$ .

Provided that the force sensor behaves within the elastic range of the material, vectors  $\vec{F}$  and  $\vec{S}$  are related by

$$\vec{S} = [C] * \vec{F}, \quad (37)$$

where [C] is a 6\*8 strain compliance matrix. The solution of Eq. (37) for  $\vec{F}$  can be derived as

$$\vec{F} = [C]^{-1} * \vec{S} = [B] * \vec{S}, \quad (38)$$

where [B] denotes the calibration matrix. The accuracy of a force sensor is reflected by influences such as linearity, cross-sensitivity, and calibration error. The fact that force sensors are employed under linear elastic behaviour of their material accounts for why the compliance matrix is a constant one and can be normalized by the corresponding component nominal loading as

$$\vec{S} = [C] * \vec{F}_1, \quad (39)$$

where [C] represents a normalized compliance matrix and  $\vec{F}_1 = (1, 1, 1, 1, 1, 1)^T$ . If a force sensor is mechanically de-coupled, all off-diagonal elements of the corresponding matrix [A] are zero. The measuring signals to reach their maximum value  $S_{in}$  when all force components reach to their nominal values simultaneously can be expressed as

$$S_{in} = \sum_{j=1}^6 C_{ij} F_{jn}. \quad (40)$$

The final calibration matrix must be expressed as

$$\begin{bmatrix} \Delta S_0 \\ \Delta S_1 \\ \Delta S_2 \\ \Delta S_3 \\ \Delta S_4 \\ \Delta S_5 \\ \Delta S_6 \\ \Delta S_7 \end{bmatrix} = \begin{bmatrix} C_{0,0} & C_{0,1} & C_{0,2} & C_{0,3} & C_{0,4} & C_{0,5} \\ C_{1,0} & C_{1,1} & C_{1,2} & C_{1,3} & C_{1,4} & C_{1,5} \\ C_{2,0} & C_{2,1} & C_{2,2} & C_{2,3} & C_{2,4} & C_{2,5} \\ C_{3,0} & C_{3,1} & C_{3,2} & C_{3,3} & C_{3,4} & C_{3,5} \\ C_{4,0} & C_{4,1} & C_{4,2} & C_{4,3} & C_{4,4} & C_{4,5} \\ C_{5,0} & C_{5,1} & C_{5,2} & C_{5,3} & C_{5,4} & C_{5,5} \\ C_{6,0} & C_{6,1} & C_{6,2} & C_{6,3} & C_{6,4} & C_{6,5} \\ C_{7,0} & C_{7,1} & C_{7,2} & C_{7,3} & C_{7,4} & C_{7,5} \end{bmatrix} \begin{bmatrix} Fx \\ Fy \\ Fz \\ Mx \\ My \\ Mz \end{bmatrix} \quad (41)$$

Where  $C_{n,m}$  are constants results from calibration curves.

Actually, a perfect diagonal matrix [A] is difficult to obtain, and non-zero off-diagonal elements,  $C_{n,m}$ , always remain non zero, resulting in the sensor's cross-sensitivity. For this reason, only the channels that affect to the final result will be used. For instance, as can be seen in figure 6-16, the four channels more sensible to the +Z force, represents the 94.34% of the strength. But the best advantage, is that if you use four channels instead of the eight ones, you save time in mathematical operations in the Force/Torque calculus. On the other hand, you have less precision in the final result.

For this reason, the actual calibration matrix results as

$$[C] = \begin{bmatrix} \Delta S_0 \\ \Delta S_1 \\ \Delta S_2 \\ \Delta S_3 \\ \Delta S_4 \\ \Delta S_5 \\ \Delta S_6 \\ \Delta S_7 \end{bmatrix} = \begin{bmatrix} C_{0,0} & 0 & 0 & 0 & 0 & C_{0,5} \\ C_{1,0} & 0 & 0 & 0 & 0 & C_{1,5} \\ 0 & 0 & C_{2,2} & 0 & C_{2,4} & 0 \\ 0 & 0 & C_{3,2} & 0 & C_{3,4} & 0 \\ 0 & C_{4,1} & 0 & 0 & 0 & C_{4,5} \\ 0 & C_{5,1} & 0 & 0 & 0 & C_{5,5} \\ 0 & 0 & C_{6,2} & C_{6,3} & 0 & 0 \\ 0 & 0 & C_{7,2} & C_{7,3} & 0 & 0 \end{bmatrix} \begin{bmatrix} Fx \\ Fy \\ Fz \\ Mx \\ My \\ Mz \end{bmatrix} \quad (42)$$

For a more graphical explanation, the channels used to calculate the final results of each force/torque can be seen in figure 6-19.

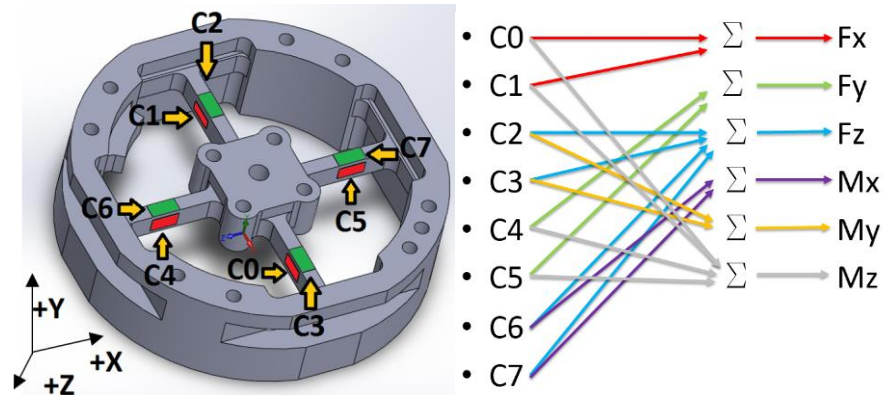


Figure 6-19 Results and sensing channels relationships

From matrix  $[C]$  (42) being now available, the force vector  $\vec{F}$  can be calculated by matrix inversion in accordance with  $\vec{F} = [C]^{-1} * \vec{S} = [A] * \vec{S}$ , where the matrix  $[A]$  is the calibration matrix of the sensor.

In expanded scalar forms, the forces are

$$\begin{aligned}
 F_x &= (C_{0,0} * S_0 + C_{1,0} * S_1) / 2 \\
 F_y &= (C_{4,1} * S_4 + C_{5,1} * S_5) / 2 \\
 F_z &= (C_{2,2} * S_2 + C_{3,2} * S_3 + C_{6,2} * S_6 + C_{7,2} * S_7) / 4 \\
 M_x &= (C_{6,3} * S_6 + C_{7,3} * S_7) / 2 \\
 M_y &= (C_{2,4} * S_2 + C_{3,4} * S_3) / 2 \\
 M_z &= (C_{0,5} * S_0 + C_{1,5} * S_1 + C_{4,5} * S_4 + C_{5,5} * S_5) / 4
 \end{aligned} \tag{43}$$

The forces/torques result from 2 or 4 different strain gauges, so it must be divided by 2 or 4 respectively.

#### 6.4.2. Calibration

For the calibration we have used 8 different weights of 146, 364, 790, 1114, 1154, 1656, 2020 and 2161 grams (figure 6-20), which represents 1.432, 3.570, 7.747, 16.240 and 21.192 Newtons respectively.



And the setup used is the explained in section 6.2. (Figures 6-21). Also it is only measured one direction per force/torque, because we assume that the sensor is symmetrical. For a complete calibration matrix, the measurements in both directions are mandatory.

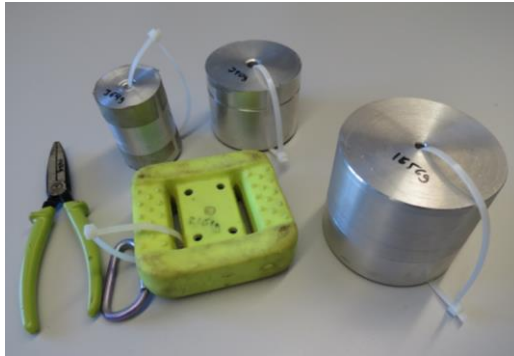


Figure 6-20. Weights used



Figure 6-22. Z torque setup

We are going to show a table with the force applied and the ADC value of each channel. Also this values are shown in a graph, with the equation of the calibration curves most representative for each test.

And finally, a table that justifies, if it is possible to use a reduced matrix calibration as explained in section 6.18. This is demonstrated if the deformation in the involved arm is much more representative than in the other ones. In this tables the percentage of the value of each channel in the final value of the force measured is shown. In green the percentages of the sensors involved for each test are remarked.

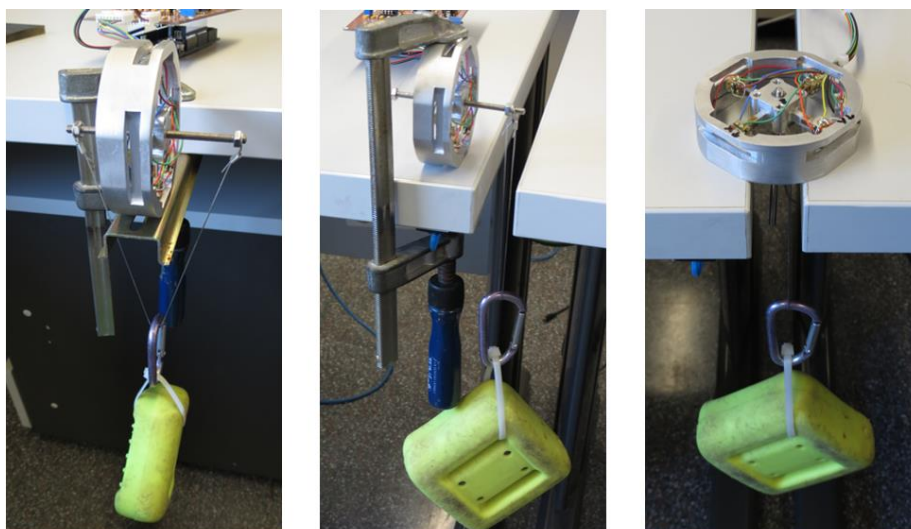


Figure 6-21. X and Y force, X and Y torque and Z force setups

**+FY test**

+FY(N)	CH0	CH1	CH2	CH3	CH4	CH5	CH6	CH7
0,000	1499	1500	1498	1499	1497	1497	1497	1495
1,432	1501	1502	1502	1489	1473	1513	1499	1498
3,570	1502	1503	1506	1479	1441	1543	1497	1499
7,747	1506	1504	1510	1469	1382	1601	1499	1502
16,240	1507	1504	1514	1459	1258	1711	1484	1497
21,192	1512	1508	1518	1449	1182	1779	1480	1500

Table 12 – ADC values in +FY test

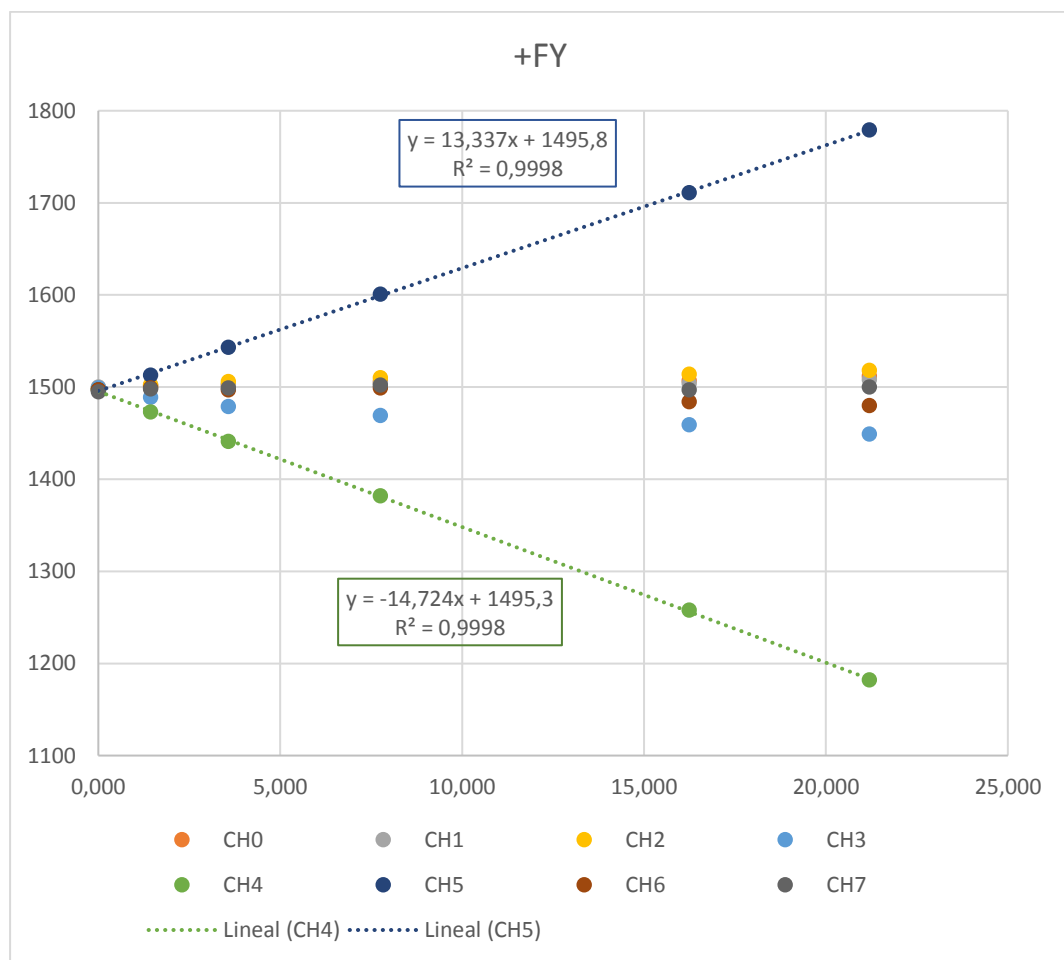


Figure 6-23. +FY test

$\Delta$ CH0	$\Delta$ CH1	$\Delta$ CH2	$\Delta$ CH3	$\Delta$ CH4	$\Delta$ CH5	$\Delta$ CH6	$\Delta$ CH7	$\Delta$ Total
13	8	20	50	315	282	17	5	710
1,83%	1,13%	2,82%	7,04%	44,37%	39,72%	2,39%	0,70%	100,00%

Table 13 – percentage of variation of each channel in +FY test

**+FX test**

+FX(N)	CH0	CH1	CH2	CH3	CH4	CH5	CH6	CH7
0,000	1458	1455	1450	1452	1451	1448	1451	1452
1,432	1480	1441	1453	1458	1454	1450	1457	1453
3,570	1509	1414	1450	1457	1451	1450	1439	1454
7,747	1565	1361	1449	1461	1450	1452	1422	1455
16,240	1675	1253	1444	1464	1446	1454	1430	1456
21,192	1741	1190	1440	1469	1429	1455	1420	1457

Table 14 – ADC values in +FX test

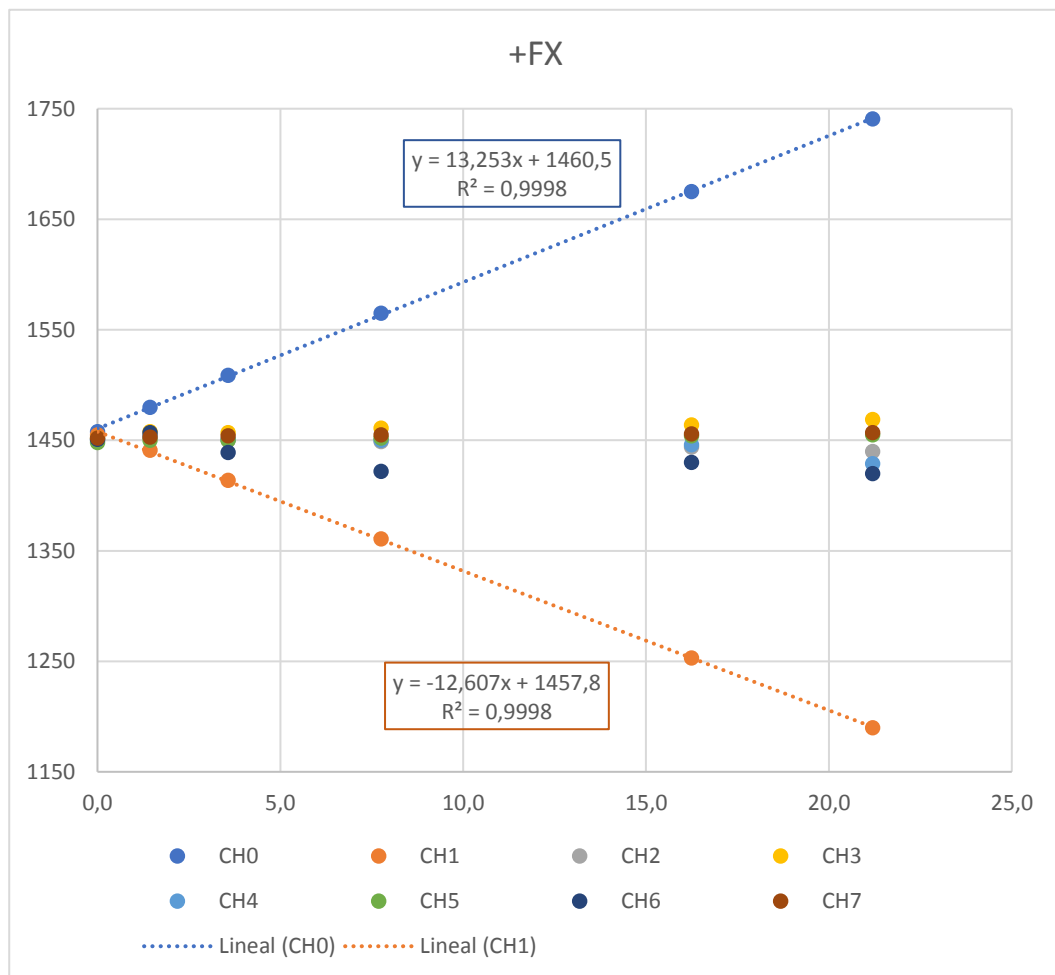


Figure 6-24. +FX test

ΔCH0	ΔCH1	ΔCH2	ΔCH3	ΔCH4	ΔCH5	ΔCH6	ΔCH7	ΔTotal
283	265	10	17	22	7	31	5	640
44%	41%	2%	3%	3%	1%	5%	1%	100%

Table 15 – percentage of variation of each channel in +FY test

**+FZ test**

+FZ(N)	CH0	CH1	CH2	CH3	CH4	CH5	CH6	CH7
0,000	1505	1505	1506	1506	1505	1504	1506	1504
1,432	1507	1508	1533	1522	1505	1508	1526	1530
3,570	1509	1511	1565	1553	1506	1509	1560	1562
7,747	1508	1513	1627	1608	1515	1510	1618	1624
16,240	1510	1520	1762	1723	1526	1516	1745	1758
21,192	1509	1519	1815	1795	1540	1515	1825	1811

Table 16 – ADC values in +FZ test

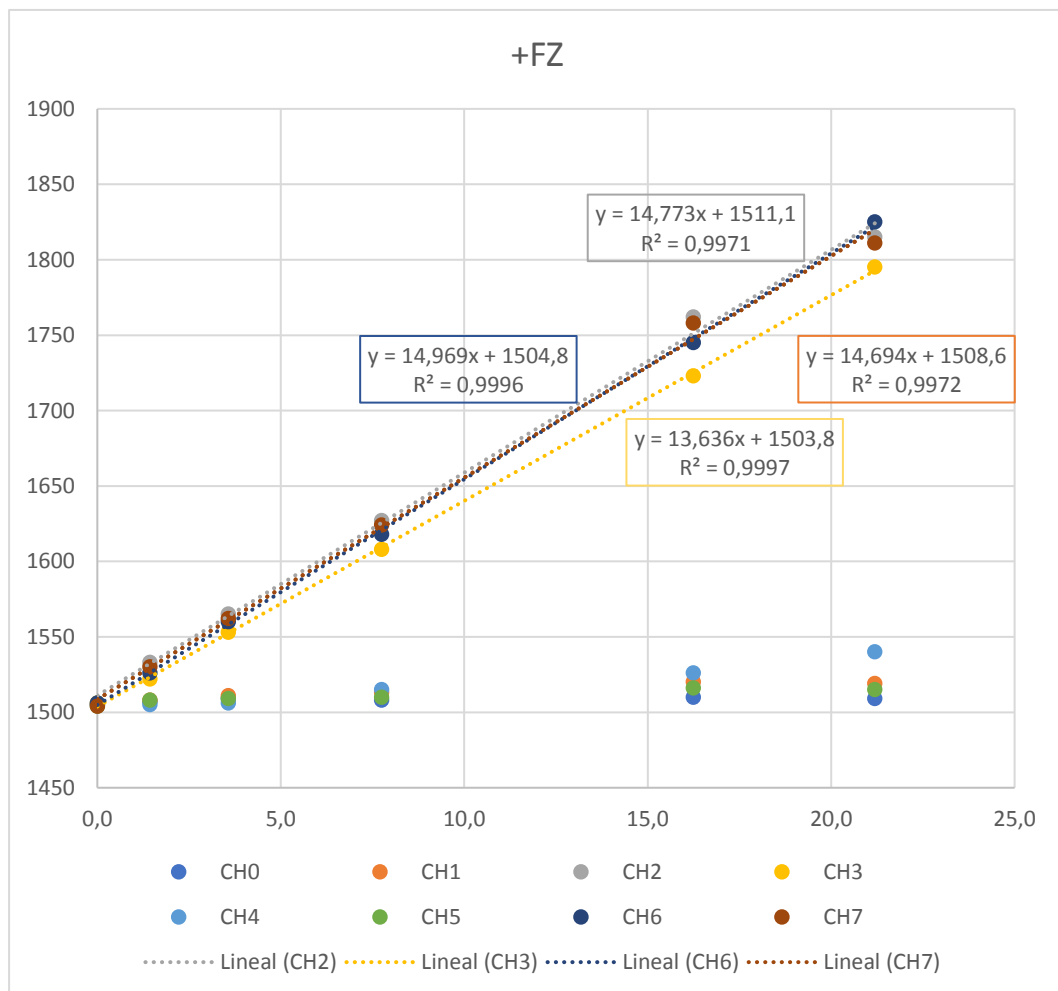


Figure 6-25. +FZ test

$\Delta$ CH0	$\Delta$ CH1	$\Delta$ CH2	$\Delta$ CH3	$\Delta$ CH4	$\Delta$ CH5	$\Delta$ CH6	$\Delta$ CH7	$\Delta$ Total
4	14	309	289	35	11	319	307	1288
0%	1%	24%	22%	3%	1%	25%	24%	100%

Table 17 – percentage of variation of each channel in +FZ test

**+MX test**

Nm	CH0	CH1	CH2	CH3	CH4	CH5	CH6	CH7
0,000E+00	1432	1428	1427	1431	1431	1429	1427	1428
4,868E-02	1451	1410	1424	1428	1420	1432	1363	1491
1,214E-01	1474	1380	1418	1427	1405	1432	1274	1576
2,634E-01	1526	1350	1410	1427	1382	1437	1105	1744
5,522E-01	1550	1330	1388	1425	1335	1447	766	2079
7,205E-01	1560	1250	1381	1427	1307	1455	564	2284

Table 18 – ADC values in +MX test

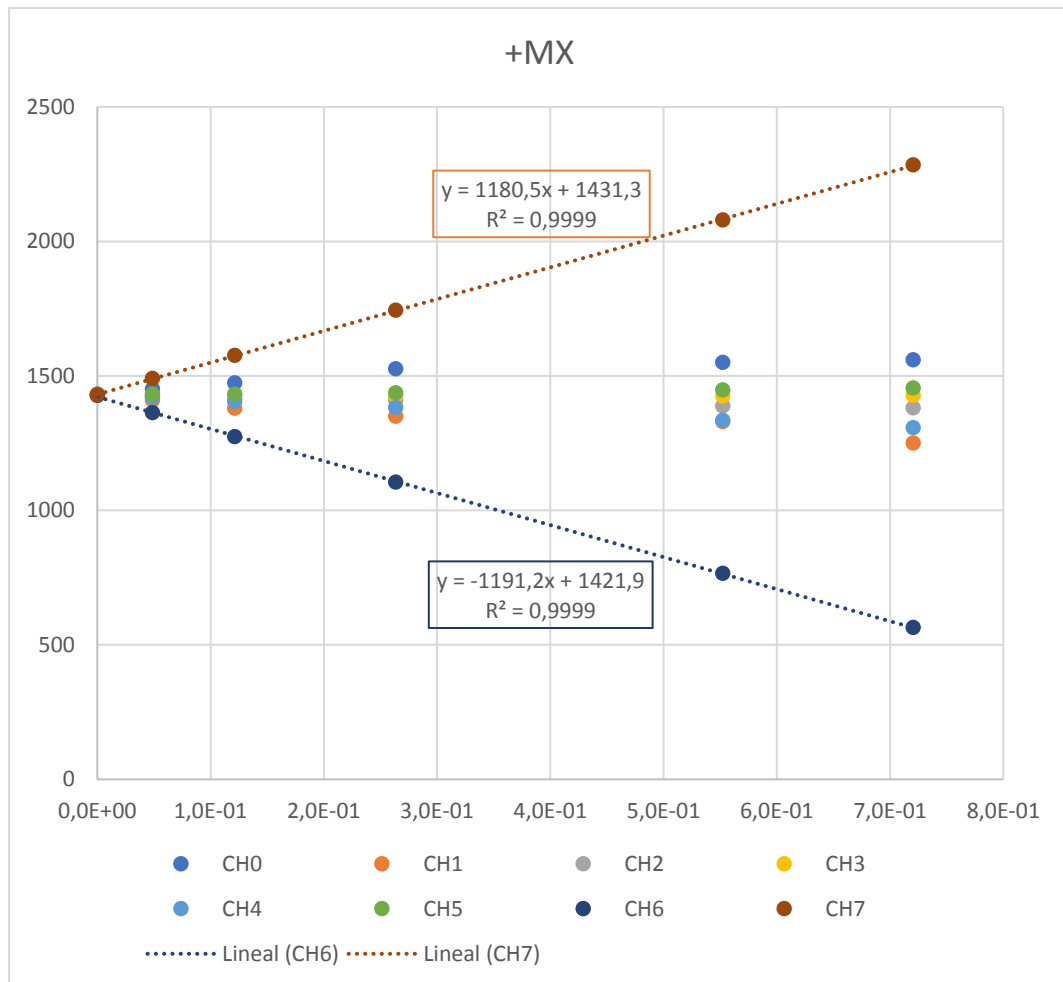


Figure 6-26 +MX test

ΔCH0	ΔCH1	ΔCH2	ΔCH3	ΔCH4	ΔCH5	ΔCH6	ΔCH7	ΔTotal
128	178	46	4	124	26	863	856	2225
6%	8%	2%	0%	6%	1%	39%	38%	100%

Table 19 – percentage of variation of each channel in +MX test

**+MY test**

Nm	CH0	CH1	CH2	CH3	CH4	CH5	CH6	CH7
0,000E+00	1497	1499	1501	1500	1501	1503	1501	1499
4,868E-02	1497	1503	1563	1443	1477	1523	1498	1500
1,214E-01	1498	1508	1648	1359	1453	1530	1492	1499
2,634E-01	1500	1514	1812	1199	1429	1563	1481	1499
5,522E-01	1506	1529	2137	877	1405	1583	1454	1495
7,205E-01	1505	1534	2293	688	1381	1603	1440	1492

Table 20 – ADC values in +MY test

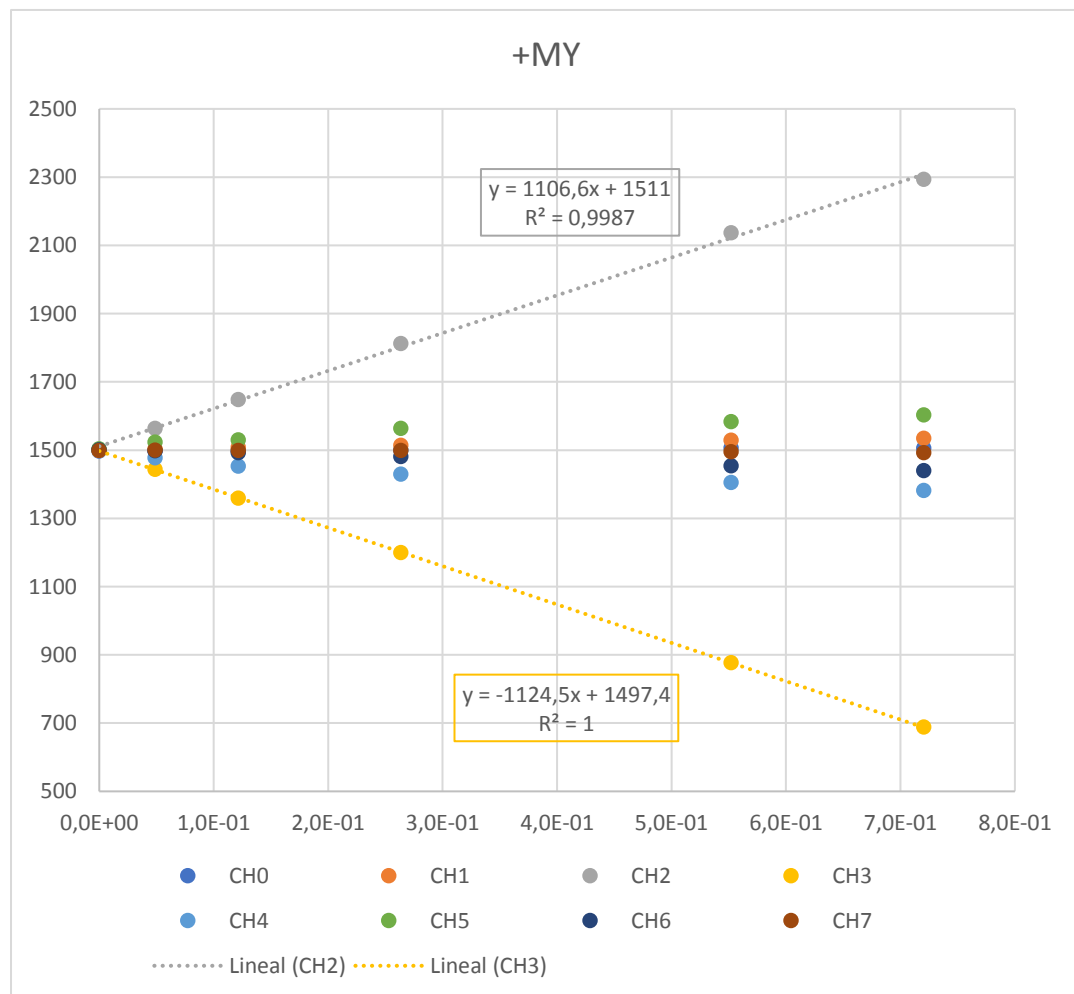


Figure 6-27. +MY test

$\Delta$ CH0	$\Delta$ CH1	$\Delta$ CH2	$\Delta$ CH3	$\Delta$ CH4	$\Delta$ CH5	$\Delta$ CH6	$\Delta$ CH7	$\Delta$ Total
8	35	792	812	120	100	61	7	1935
0%	2%	41%	42%	6%	5%	3%	0%	100%

Table 21 – percentage of variation of each channel in +MY test

**+MZ test**

Nm	CH0	CH1	CH2	CH3	CH4	CH5	CH6	CH7
0,000E+00	1509	1506	1509	1511	1508	1502	1506	1505
4,868E-02	1536	1543	1517	1513	1545	1531	1521	1509
1,214E-01	1558	1563	1512	1520	1577	1550	1525	1518
2,634E-01	1594	1608	1488	1535	1635	1588	1517	1502
5,522E-01	1701	1724	1504	1540	1774	1686	1540	1538
7,205E-01	1760	1771	1477	1545	1864	1730	1558	1539

Table 22 – ADC values in +MZ test

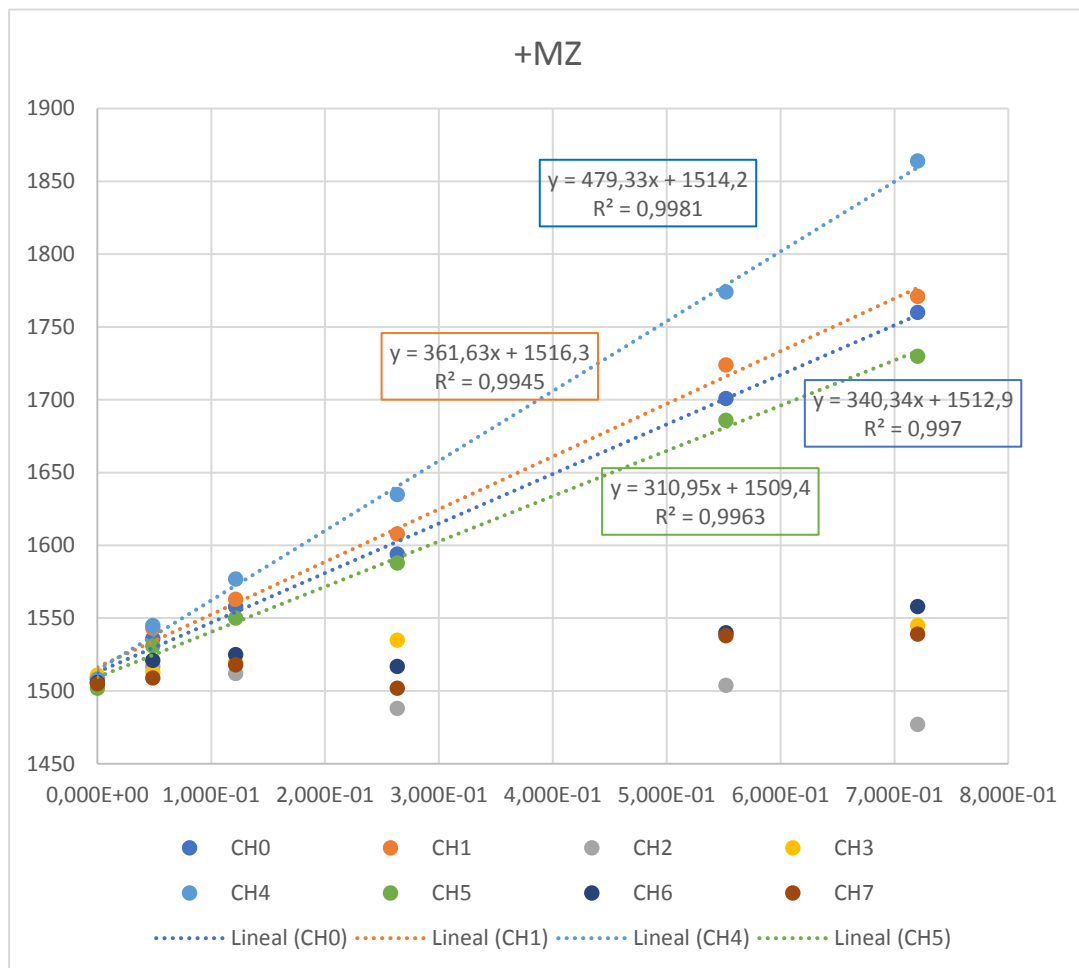


Figure 6-28. +MZ test

$\Delta$ CH0	$\Delta$ CH1	$\Delta$ CH2	$\Delta$ CH3	$\Delta$ CH4	$\Delta$ CH5	$\Delta$ CH6	$\Delta$ CH7	$\Delta$ Total
251	265	32	34	356	228	52	34	1252
20%	21%	2%	3%	28%	18%	4%	3%	100%

Table 23 – percentage of variation of each channel in +MZ test

From this tables and figures, we can conclude three important points.

The first conclusion can be derived from tables 13, 15, 17, 19, 21 and 23. We can see that the sensor shape is correct because each sensor is lineally independent. That means that only the arms involved in each force are deformed, so the mechanical design and the milling of the sensor is correct.

Another conclusion, is that the strain gauges are correctly bonded because they are very sensitive, and all of them have a similar slope in the calibration curves.

And finally, we can check in the figures 6.25 to 6.28 that the deformation in the sensor arms is clearly lineal in the range of forces that we want to measure.



### 6.4.3. Calibration matrix calculation

From calibration curves of figures 6.24 to 6.27, we obtain the  $C_{n,m}$  values. Where  $n$  is the number of sensor, and  $m$  is the magnitude calculated.

#### +FX

$$y_{+FX1} = 13,253x_{+FX1} + 1460,5 \Rightarrow x_{+FX1} = \frac{y_{+FX1} - 1460,5}{13,253} = C_{0,0}$$

$$y_{+FX2} = -12,607x_{+FX2} + 1457,8 \Rightarrow x_{+FX2} = \frac{y_{+FX2} - 1457,8}{-12,607} = C_{1,0}$$

#### +FY

$$y_{+FY1} = 13,337x_{+FY1} + 1495,8 \Rightarrow x_{+FY1} = \frac{y_{+FY1} - 1495,8}{13,337} = C_{5,1}$$

$$y_{+FY2} = -14,724x_{+FY2} + 1495,3 \Rightarrow x_{+FY2} = \frac{y_{+FY1} - 1495,3}{-14,724} = C_{4,1}$$

#### +FZ

$$y_{+FZ1} = 14,773x_{+FZ1} + 1511,1 \Rightarrow x_{+FZ1} = \frac{y_{+FZ1} - 1511,1}{14,773} = C_{2,2}$$

$$y_{+FZ2} = 14,969x_{+FZ2} + 1504,8 \Rightarrow x_{+FZ2} = \frac{y_{+FZ2} - 1504,8}{14,969} = C_{6,2}$$

$$y_{+FZ3} = 14,694x_{+FZ3} + 1508,6 \Rightarrow x_{+FZ3} = \frac{y_{+FZ3} - 1508,6}{14,694} = C_{7,2}$$

$$y_{+FZ4} = 13,636x_{+FZ4} + 1503,8 \Rightarrow x_{+FZ4} = \frac{y_{+FZ4} - 1503,8}{13,636} = C_{3,2}$$

#### +MX

$$y_{+MX1} = 1180,5x_{+MX1} + 1431,3 \Rightarrow x_{+MX1} = \frac{y_{+MX1} - 1431,3}{1180,5} = C_{7,3}$$

$$y_{+MX2} = -1191,2x_{+MX2} + 1421,9 \Rightarrow x_{+MX2} = \frac{y_{+MX2} - 1421,9}{-1191,2} = C_{6,3}$$

#### +MY

$$y_{+MY1} = 1106,6x_{+MY1} + 1511 \Rightarrow x_{+MY1} = \frac{y_{+MY1} - 1511}{1106,6} = C_{2,4}$$

$$y_{+MY2} = -1124,5x_{+MY2} + 1497,4 \Rightarrow x_{+MY2} = \frac{y_{+MY2} - 1497,4}{-1124,5} = C_{3,4}$$

### +MZ

$$y_{+MZ1} = 479,33x_{+MZ1} + 1514,2 \Rightarrow x_{+MZ1} = \frac{y_{+MZ1} - 1514,2}{479,33} = C_{4,5}$$

$$y_{+MZ2} = 361,63x_{+MZ2} + 1516,3 \Rightarrow x_{+MZ2} = \frac{y_{+MZ2} - 1516,3}{361,63} = C_{1,5}$$

$$y_{+MZ3} = 340,34x_{+MZ3} + 1512,9 \Rightarrow x_{+MZ3} = \frac{y_{+MZ3} - 1512,9}{340,34} = C_{0,5}$$

$$y_{+MZ4} = 310,95x_{+MZ4} + 1509,4 \Rightarrow x_{+MZ4} = \frac{y_{+MZ4} - 1509,4}{310,95} = C_{5,5}$$

Once we have all  $C_{n,m}$  values, it is possible to fill the equations (43).

$$Fx = \frac{(C_{0,0} * S_0 + C_{1,0} * S_1)}{2} = \frac{\left( \frac{S_0 - 1460,5}{13,253} + \frac{S_1 - 1457,8}{-12,607} \right)}{2}$$

$$Fy = \frac{(C_{4,1} * S_4 + C_{5,1} * S_5)}{2} = \frac{\left( \frac{S_4 - 1495,3}{-14,724} + \frac{S_5 - 1495,8}{13,337} \right)}{2}$$

$$Fz = \frac{(C_{2,2} * S_2 + C_{3,2} * S_3 + C_{6,2} * S_6 + C_{7,2} * S_7)}{4} = \frac{\left( \frac{S_2 - 1511,1}{14,773} + \frac{S_3 - 1503,8}{13,636} + \frac{S_6 - 1504,8}{14,969} + \frac{S_7 - 1508,6}{14,694} \right)}{4}$$

$$Mx = \frac{(C_{6,3} * S_6 + C_{7,3} * S_7)}{2} = \frac{\left( \frac{S_6 - 1421,9}{-1191,2} + \frac{S_7 - 1431,3}{1180,5} \right)}{2}$$

$$My = \frac{(C_{2,4} * S_2 + C_{3,4} * S_3)}{2} = \frac{\left( \frac{S_2 - 1511}{1106,6} + \frac{S_3 - 1497,4}{-1124,5} \right)}{2}$$

$$Mz = \frac{(C_{0,5} * S_0 + C_{1,5} * S_1 + C_{4,5} * S_4 + C_{5,5} * S_5)}{4} = \frac{\left( \frac{S_0 - 1512,9}{340,34} + \frac{S_1 - 1516,3}{361,63} + \frac{S_4 - 1514,2}{479,33} + \frac{S_5 - 1509,4}{310,95} \right)}{4}$$

Translated to C code:

```
FX = (((sensorValue0-1460.5)/13.253) + ((sensorValue1-1457.8)/-12.607))/2;  
FY = (((sensorValue4-1495.3)/-14.724) + ((sensorValue5-1495.8)/13.337))/2;  
FZ = (((sensorValue2-1511.1)/14.773) + ((sensorValue3- 1503.8)/13.636) +  
((sensorValue6-1504.8)/14.969) + ((sensorValue7-1508.6)/14.694))/4;  
MX = (((sensorValue6-1421.9)/-1191.2) + ((sensorValue7-1431.3)/1180))/2;  
MY = (((sensorValue2-1511)/1106.6) + ((sensorValue3-1497.4)/-1124.5))/2;  
MZ = (((sensorValue0-1512.9)/340.34) + ((sensorValue1- 1516.3)/361.63) +  
((sensorValue4-1514.2)/479.33) + ((sensorValue5-1509.4)/310.95))/4;
```

Finally we want to test if the calibration matrix values are correct. To do this, we are going to repeat the same setup explained, but we are going to use different weights. In this case are of 88, 512 and 1725 grams, which represents 0.862, 5.021 and 16.896 Newtons respectively. In torques, a distance of 34mm that represents 0.29, 17.07 and 57.43 Ncm.

**+FY test**

+FY(N) Applied	+FY(N)	+FX(N)	+FZ(N)	+MY(Ncm)	+MX(Ncm)	+MZ(Ncm)
0	0,05	0,04	-0,02	0,02	0,03	0,01
0,862	0,855	0,06	-0,02	0,02	0,03	0,01
5,021	4,998	0,1	-0,04	0,06	0,04	0,02
16,896	16,826	0,15	-0,06	0,07	0,04	0,03

Table 24 – Force and Torque values in +FY test

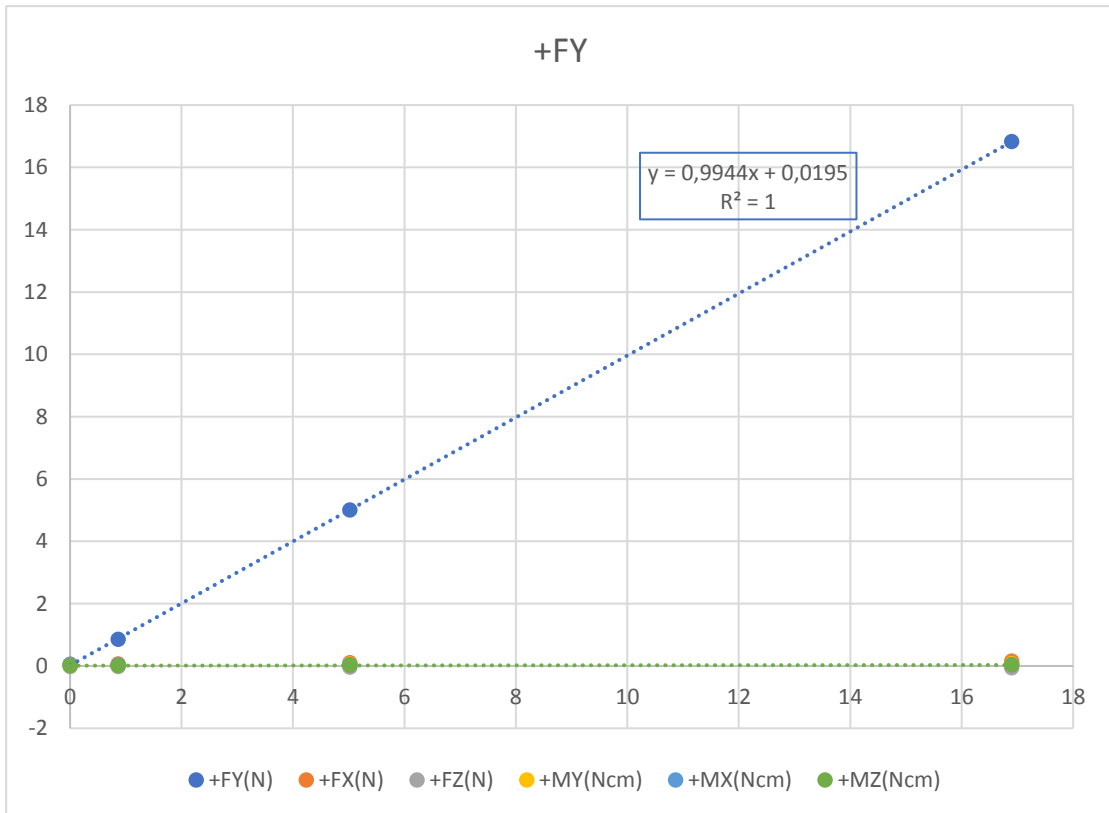


Figure 6-29. – Force and Torque in +FY test

**+FX test**

+FX(N) Applied	+FY(N)	+FX(N)	+FZ(N)	+MY(Ncm)	+MX(Ncm)	+MZ(Ncm)
0	0,05	0,04	-0,02	0,02	0,03	0,01
0,862	0,07	0,87	-0,03	0,03	0,03	0,01
5,021	0,09	5,1	-0,06	0,05	0,06	0,03
16,896	0,1	16,98	-0,08	0,08	0,08	0,06

Table 25 – Force and Torque values in +FX test

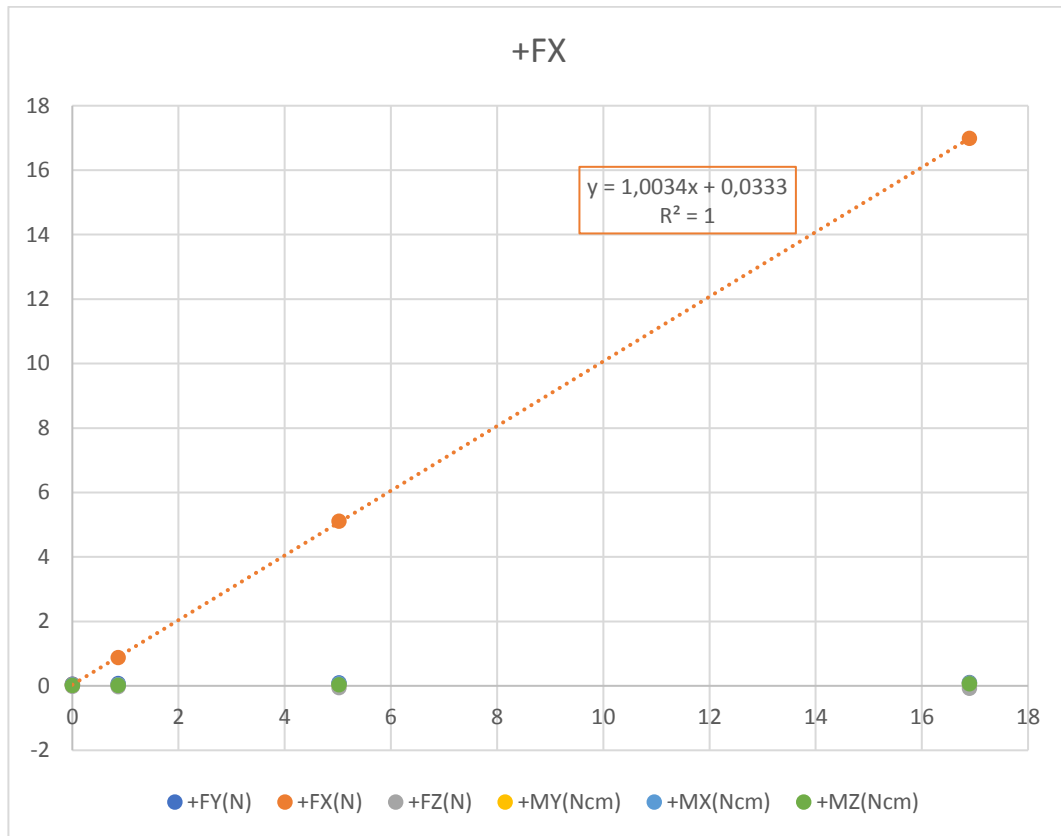


Figure 6-30. – Force and Torque in +FY test

**+FZ test**

+FZ(N) Applied	+FY(N)	+FX(N)	+FZ(N)	+MY(Ncm)	+MX(Ncm)	+MZ(Ncm)
0	0,05	0,04	-0,02	0,02	0,03	0,01
0,862	0,07	0,06	0,83	0,03	0,03	0,01
5,021	0,09	0,1	4,9	0,03	0,04	0,03
16,896	0,1	0,15	16,76	0,05	0,06	0,08

Table 26 – Force and Torque values in +FZ test

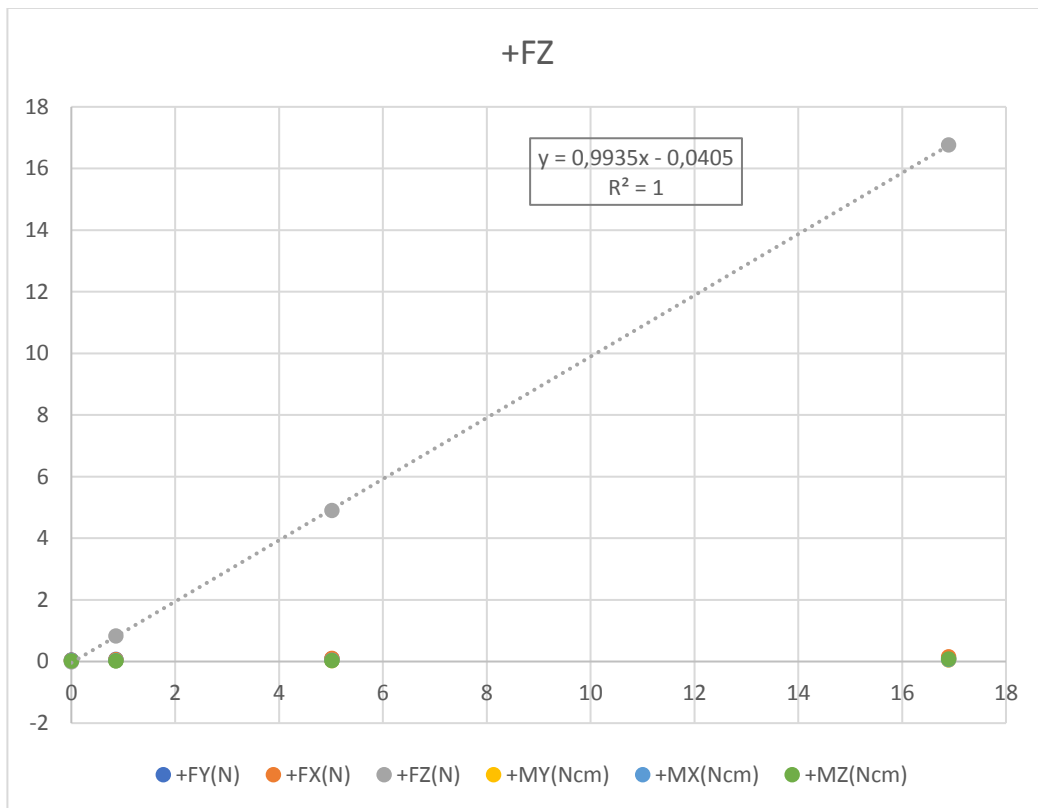


Figure 6-31. – Force and Torque in +FZ test

**+MY test**

+MY(Ncm) Applied	+FY(N)	+FX(N)	+FZ(N)	+MY(Ncm)	+MX(Ncm)	+MZ(Ncm)
0,00	0,05	0,04	-0,02	0,00	0,03	0,01
0,29	0,07	0,06	-0,02	0,32	0,03	0,01
17,07	0,13	0,1	-0,04	17,37	0,04	0,02
57,43	0,19	0,15	-0,06	58,16	0,04	0,03

Table 27 – Force and Torque values in +MY test

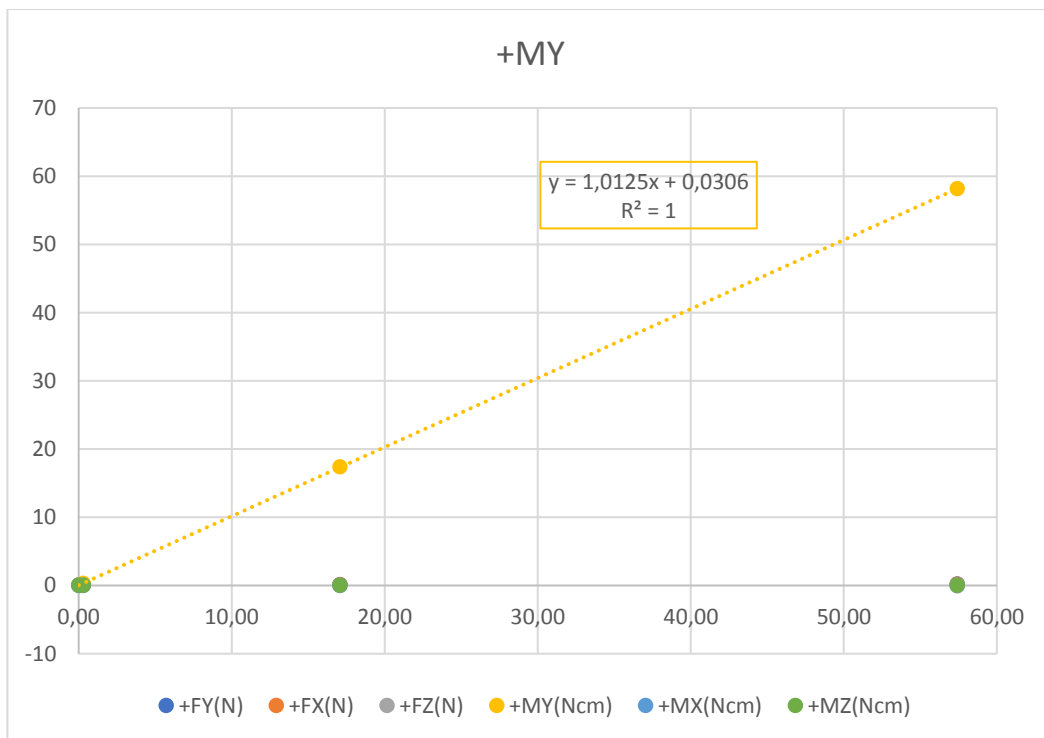


Figure 6-32. – Force and Torque in +MY test

**+MX test**

+MX(Ncm) Applied	+FY(N)	+FX(N)	+FZ(N)	+MY(Ncm)	+MX(Ncm)	+MZ(Ncm)
0,00	0,05	0,04	-0,02	0,02	0,03	0,01
0,29	0,07	0,06	-0,02	0,03	0,32	0,01
17,07	0,13	0,1	-0,04	0,07	18,34	0,02
57,43	0,19	0,15	-0,06	0,08	59,64	0,03

Table 28 – Force and Torque values in +MX test

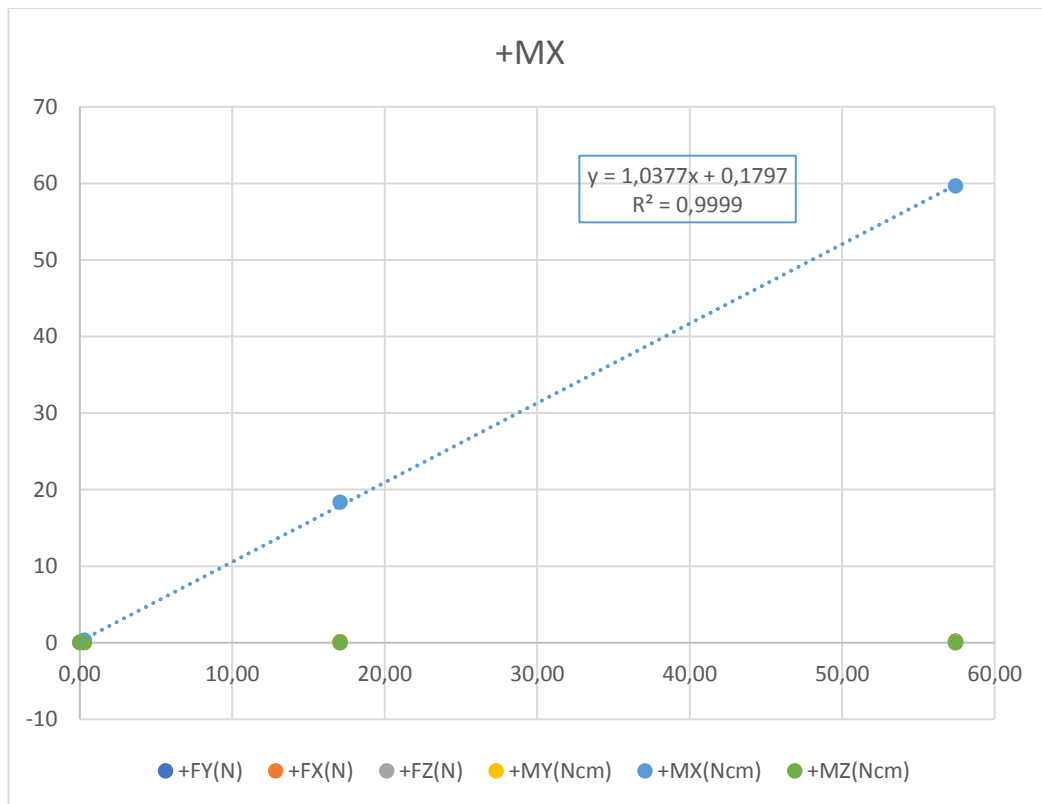


Figure 6-33. – Force and Torque in +MX test



**+MZ test**

+MZ(Ncm) Applied	+FY(N)	+FX(N)	+FZ(N)	+MY(Ncm)	+MX(Ncm)	+MZ(Ncm)
0,00	0,05	0,04	-0,02	0,02	0,01	0,00
0,29	0,07	0,06	-0,02	0,03	0,01	0,32
17,07	0,13	0,1	-0,04	0,07	0,02	17,67
57,43	0,19	0,15	-0,06	0,08	0,03	58,66

Table 29 – Force and Torque values in +MZ test

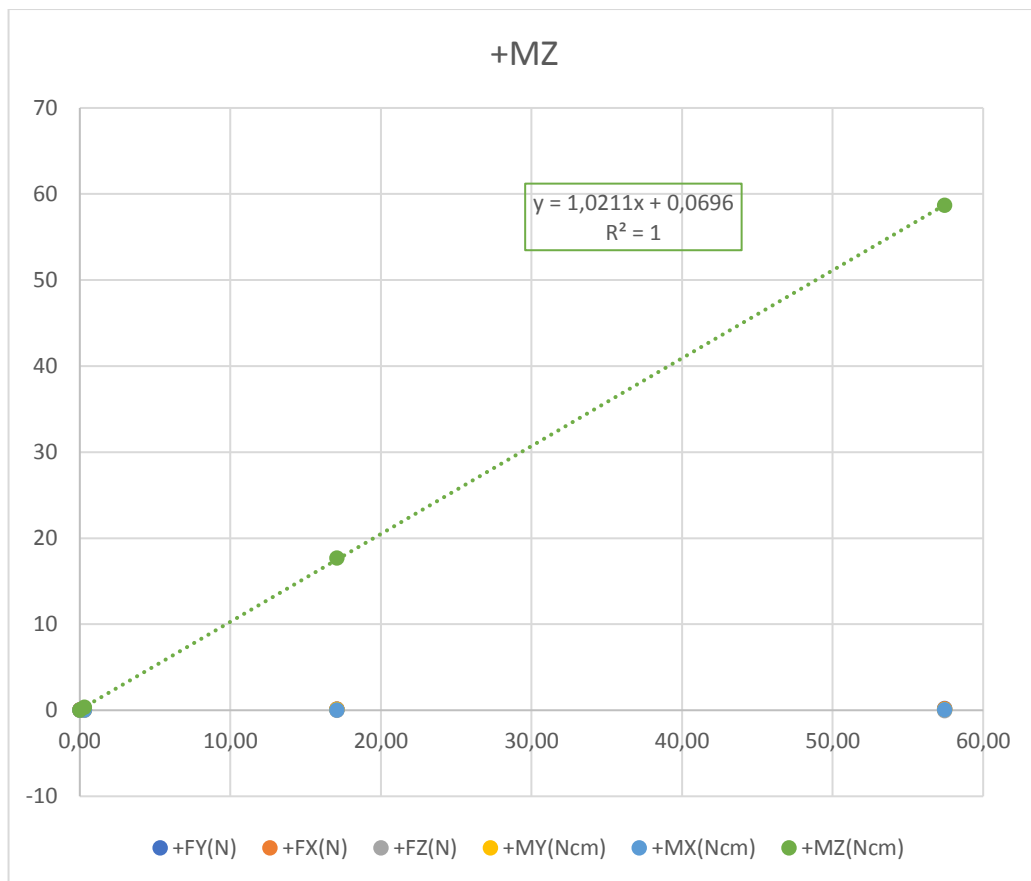


Figure 6-34. – Force and Torque in +MZ test

From figures 6-30 to 6-34 we can conclude that the calibration matrix values are correct. The Force / Torque involved in the measurement, must have an equation of  $y=x$ , and as we can see, this values are pretty good. With a more exhaustive calibration, better results could be achieved.

## 7. Budget

### 7.1. Introduction

It is presented a comprehensive economic analysis of this project. It has been divided into several blocks: the first scheduling, development costs and materials and, finally, the total cost of the set. It should be noted that this budget is only about the design and construction of the sensor.

Depreciation and maintenance of CNC machines have been used, which are in the laboratory of product development, have been also taken into account.

### 7.2. Tasks

The following table represents the planning of the project according to the different phases that correspond to the tasks.

It has been considered an eight-hour work day to calculate the hours spent working.

TASKS	Days	Hours
Study of the project	4	32
Defining the scope	4	32
Previous studies development	20	160
Design and theoretical calculations	22	176
Prototype Design & Simulations	14	112
Implementation of the prototype	16	128
Mechanical prototype testing phase	10	80
Electronics and PCB Design	16	128
PCB Assembly	4	32
PCB testing phase	8	64
Implementation of processing software	18	144
Calibration System	20	160
Interface development	30	240
Test phase and final improvements	12	96
Documentation	50	400
<b>TOTAL</b>	<b>248</b>	<b>1984</b>

Table 30 – Tasks definition and hour cost

### 7.3. Personnel costs

In order to quantify the costs of development (presented in the next section), it is assumed that the designer salary is € 30 per hour, regardless of the work they have undertaken in order to simplify the process.

PHASE	Hours	Cost (€)
Study of the project	32	960
Defining the scope	32	960
Previous studies development	160	4800
Design and theoretical calculations	176	5328
Prototype Design & Simulations	112	3360
Implementation of the prototype	128	3840
Mechanical prototype testing phase	80	2400
Electronics and PCB Design	128	3840
PCB Assembly	32	960
PCB testing phase	64	1920
Implementation of processing software	144	4320
Calibration System	160	4800
Interface development	240	7200
Test phase and final improvements	96	2880
Documentation	400	12000
<b>TOTAL</b>	<b>1984</b>	<b>59520</b>

Table 31 – Tasks definition and hour cost

### 7.4. Material costs

The costs relating to hardware and materials used, without considering the cost of installation or assembly, are shown in the table below. It should be mentioned that the price of the PC used to view the data has not been considered in this budget.

The detailed price per component, can be seen in Annex C

ATTRIBUTE	COST (€)
Aluminium materials	35,00
Screws	25,00
Electronic components	24.8
cabling	3,00
connectors	7,00
PCB	3,86
additional materials	10,00
<b>TOTAL</b>	<b>108.66</b>

Table 32 – Material costs

### 7.5. Total cost of development

In order to calculate the real cost of the project, it also has to take into account the cost of the facilities where the sensor has been build, as well as the amortization of machinery used. To make these calculations, it has been estimated that the cost represented by the UPC, the owner of the facilities and machinery, and the workload has been estimated that this project represents in relation to all projects that occupy the same space and / or sharing the use of machinery.

CONCEPT	COST (€)
Cost of annual maintenance of facilities	18000
Annual depreciation of equipment	35000
<b>Estimated time for this project total project</b>	<b>8%</b>

Table 33 – Annual cost of equipment

Based on the analysis made in the previous sections, the total cost of the project development has proved to:

CONCEPT	COST (€)
Personnel costs	<b>59520</b>
Material costs	<b>108.66</b>
Costs for facilities	1440
Impact of equipment	2800
<b>TOTAL</b>	<b>63869.66</b>

Table 34 – Total cost

### 7.6. Cost per unit of the force sensor

In order to calculate the cost per unit, only has been taken into account the cost of the components (electronic and mechanical) and PCB. And as is shown in Table 26, this costs represents 108.66€.

This price can be sensible lower as we know that the electronic components are much cheaper if they are obtained in large quantities, and the cost in hours of the aluminium milling is faster in production phases.

## 8. Conclusions and future development

### 8.1. Conclusions

In this project, a design of a sensor device for 6-DoF force/torque measurement is described. It is compact, well-decoupled and low cost. Good results in terms of the measurement isotropy and measurement sensitivity have been obtained. By performing the design optimization in conjunction with the finite element analysis, affect the optimal sizes of the force-sensing arms were determined.

Although high couplings exist in such a six component force sensor, they sparsely in a few places in the calibration matrix, making the calculations for the force components reasonably easy and quick.

Both analytical and numerical tools were employed in optimization analyses used to determine the sensor's geometric parameters. Design and fabrication rules were generated for manufacturing a compact and temperature-stable signal conditioning circuit. The performance of the sensor was tested both in benchtop calibration experiments.

The cheap material and the simple structure of the sensor make it low cost. Also the sensor is available for large forces and moments if is mechanically redesigned. The elastic body is designed to obtain the large measurement range. Then, ANSYS has been used to optimize the size. The high precision are supported by the design of hardware, the calibration system and the decoupling algorithm. Calibration system is specially designed to provide standard force and torque source.

	ATI Gamma	Prototype proposed	Goal achieved
Data byte	24	10/12	12/14 ✓
Baud rate	100k/s	100/s	685/s ✓✓
Software	Closed	Open source	Open source ✓
Communications	PCI board	Serial USB, Ethernet	Serial & USB ✓
Price	8000€ approximately	<800€	109€ ✓✓✓

Table 35 - Comparisons between commercial F/T sensor, proposed specifications and goals achieved

In table 35, we have our original targets and if we have reached them or not.

Firstly, we wanted at least 10 bits ADC values, and in the final prototype we can reach up to 14 bits with an acceptable noise. Then, our goal for baud rate was 100 samples per second, and we have reached 685 sps for 12 bits data.

The control software has been implemented with the Arduino IDE, so it means that is a totally open source.

The communications now are via serial and USB.

And finally with reference to the materials price, we have reached a final value of 109€. This is less than the expected, and 90 times less than a commercial force sensor. In other words, the cost of this sensor is only a 1.36% on the price of the ATI Gamma sensor.

So, in spite of its low cost, the sensor's measurement performance is comparable to more expensive, commercial 6-DoF sensors (e.g. ATI Gamma). The introduced calibration method allow to achieve high angular and magnitudinal accuracy, which makes it possible to use the 3D force sensor in any application in which both precision and low cost sensor play a significant role.

## 8.2. Future development

Some works can be done to improve the sensor specifications.

First of all, we must study a way to calibrate much better the sensor. To do this job, it is necessary to repeat all calibration setups, but if we take into account that our sensor have 6 degrees of freedom, with 2 directions each, and a minimum of 6 weights for each test, this is a total of 72 tests. Moreover, if we also want to calibrate for different temperatures, for 4 different temperatures we have 288 tests. And if we want to use the different gains to do the auto-scale, for 5 of them we have 1440 tests. That is why this project has finished with a basic calibration matrix.

Other work in order to do the sensor much faster is to pack the data to do the communication between the sensor and the computer, and change the microcontroller for a Cortex M4 or similar.

## **Bibliography**

- [1] Google [Accessed: 13 October 2015]  
<http://www.google.com.ar/patents/EP2510325A2?cl=en>
- [2] K. Tanie, et al.: A High-Resolution Tactile Sensor, *Robot Sensors*, Vol. 2, 1986, pp. 189-198
- [3] Wang, A.B.; He, S.; Fang, X.J.; Jin, X.D.; Lin, J.X. Optical fiber pressure sensor based on photoelasticity and its application. *J. Lightwave Technol.* 1992, 10, 1466–1472.
- [4] Urban, F.; Kadlec, J.; Vlach, R.; Kuchta, R. Design of a pressure sensor based on optical fiber bragg grating lateral deformation. *Sensors* 2010, 10, 11212–11225.
- [5] Sensor Contributor. "Acceleration/Vibration Tunable Lasers for Multichannel Fiber-Optic Sensors". *Sensors Online*, 2015. [Online] Available: <http://www.sensormag.com/sensors/acceleration-vibration/tunable-lasers-multichannel-fiber-optic-sensors-823>. [Accessed: 2 November 2015].
- [6] Qiaokang Liang, Dan Zhang, Yaonan Wang, Yunjian Ge. "Design and Analysis of a Novel Six-Component F/T Sensor based on CPM for Passive Compliant Assembly", *MEASUREMENT SCIENCE REVIEW*, Volume 13, No. 5, pp253-264, 2013
- [7] Jin, W.L., Mote, C.D., Jr. "A six-component silicon micro force sensor. *Sensors and Actuators*" A: Physical, 65 (2-3), 109-115. 1998.
- [8] Mei, T., Ge, Y., Chen, Y., Ni, L., Liao, W.H., Xu, Y., Li, W.J. "Design and fabrication of an integrated three-dimensional tactile sensor for space robotic applications". In *Micro Electro Mechanical Systems (MEMS '99): 12th IEEE International Conference*, 17-21 January 1999. IEEE, 112-117.
- [9] Brookhuis, R.A., Lammerink, T.S.J., Wiegerink, R.J., de Boer, M.J., Elwenspoek, M.C. "3D force sensor for biomechanical applications". *Sensors and Actuators A: Physical*, 2012
- [10] Takenawa, S. (2009). "A soft three-axis tactile sensor based on electromagnetic induction". In *Mechatronics 2009. ICM 2009: IEEE International Conference*, 14- 17 April 2009. IEEE, 1-6.
- [11] Gobbi, M., Previati, G., Guarneri, P., Mastinu, G. "A new six-axis load cell. Part II: Error, analysis, construction and experimental assessment of performances". *Experimental Mechanics*, 51, 2011
- [12] Liu, T., Inoue, Y., Shibata, K., Yamasaki, Y., Nakahama, M. (2004). "A six-dimension parallel force sensor for human dynamics analysis". In *Robotics, Automation and Mechatronics*, 1-3 December 2004.
- [13] Hirose, S., Yoneda, K. (1990). "Development of optical six-axial force sensor and its signal calibration considering nonlinear interference". In *Robotics and Automation*, 13-18 May 1990. IEEE, 46-53.
- [14] Jia, Z.Y., Lin, S., Liu, W. "Measurement method of six-axis load sharing based on the Stewart platform". *Measurement*, 43, 2010

- [15] Dan Mihai Stefanescu, "Handbook of Force Transducers, Principles and Components", Springer, ISBN 978-3-642-18295-2, 2011
- [16] Ralph S. Shoberg, "Driveline torque and/or thrust sensor," U.S. Patent 3956930 A, September 23, 1974.
- [17] Seahak Kim, Shoichi Hasegawa, Yasuharu Koike, and Makoto Sato, "Tension Based 7-DOF Force Feedback Device: SPIDAR-G", Proceedings of the IEEE Virtual Reality 2002 (VR'02), 2002
- [18] B. Dasgupta, S. Reddy, T.S. Mruthyunjaya, Synthesis of a force-torque sensor based on the Stewart Platform mechanism, in: Proceedings of National Convention of Industrial Problems in Machines and Mechanisms (IPROMM'94), Bangalore, India, pp. 14-23
- [19] Timoshenko, S. "On the correction for shear of the differential equation for transverse vibrations of prismatic bars". Lond. Edinb. Dublin Philos. Mag. J. Sci. 1921, 41, 744-746.
- [20] Junqing Ma and Aiguo Song "Fast Estimation of Strains for Cross-Beams Six-Axis Force/Torque Sensors by Mechanical Modeling" Sensors 2013, 13, 6669-6686; DOI:10.3390/s130506669.
- [21] Pilkey, W.D.; Pilkey, H.O. "Mechanics of Solids"; RE Krieger Publishing Company: Malabar, FL, USA, 1986.
- [22] Barry Dupen "Applied Strength of Materials for Engineering Technology" Indiana University – Purdue University Fort Wayne, 2014
- [23] Dan Mihai Stefanescu "Handbook of Force Transducers"; Springer-Verlag Berlin Heidelberg, 2011
- [24] Marek Krehel, René M. Rossi<sup>1</sup>, Gian-Luca Bona and Lukas J. Scherer, \*. "Characterization of Flexible Copolymer Optical Fibers for Force Sensing Applications". Sensors, 2015. [Online] Available: <http://www.mdpi.com/1424-8220/13/9/11956/htm>. [Accessed: 2 November 2015].
- [25] Simultaneous Sampling Data Acquisition Architectures  
<http://www.ni.com/white-paper/4105/en/> [Accessed: 9 September 2016]
- [26] Key parameters for ATmega328  
<http://www.atmel.com/devices/atmega328.aspx?tab=parameters> [Accessed: 9 September 2016]
- [27] <http://soliton.ae.gatech.edu/people/jcraig/classes/ae3145/Lab2/strain-gages.pdf>
- [28] <http://www.ti.com/lit/an/slva689/slva689.pdf>
- [29] <https://www.hbm.com/en/4314/tips-and-tricks-the-correct-selection-of-adhesives-for-the-installation-of-strain-gauges/>
- [30] [http://www.atmel.com/Images/Atmel-42735-8-bit-AVR-Microcontroller-ATmega328-328P\\_Summary.pdf](http://www.atmel.com/Images/Atmel-42735-8-bit-AVR-Microcontroller-ATmega328-328P_Summary.pdf)<sup>000</sup>
- [31] <http://ww1.microchip.com/downloads/en/DeviceDoc/21909d.pdf>
- [32] <http://www.nxp.com/assets/documents/data/en/data-sheets/MMA8451Q.pdf>



[33] [http://www.analog.com/media/en/analog-dialogue/volume-39/number-2/articles/the-right-adc-architecture .pdf](http://www.analog.com/media/en/analog-dialogue/volume-39/number-2/articles/the-right-adc-architecture.pdf)

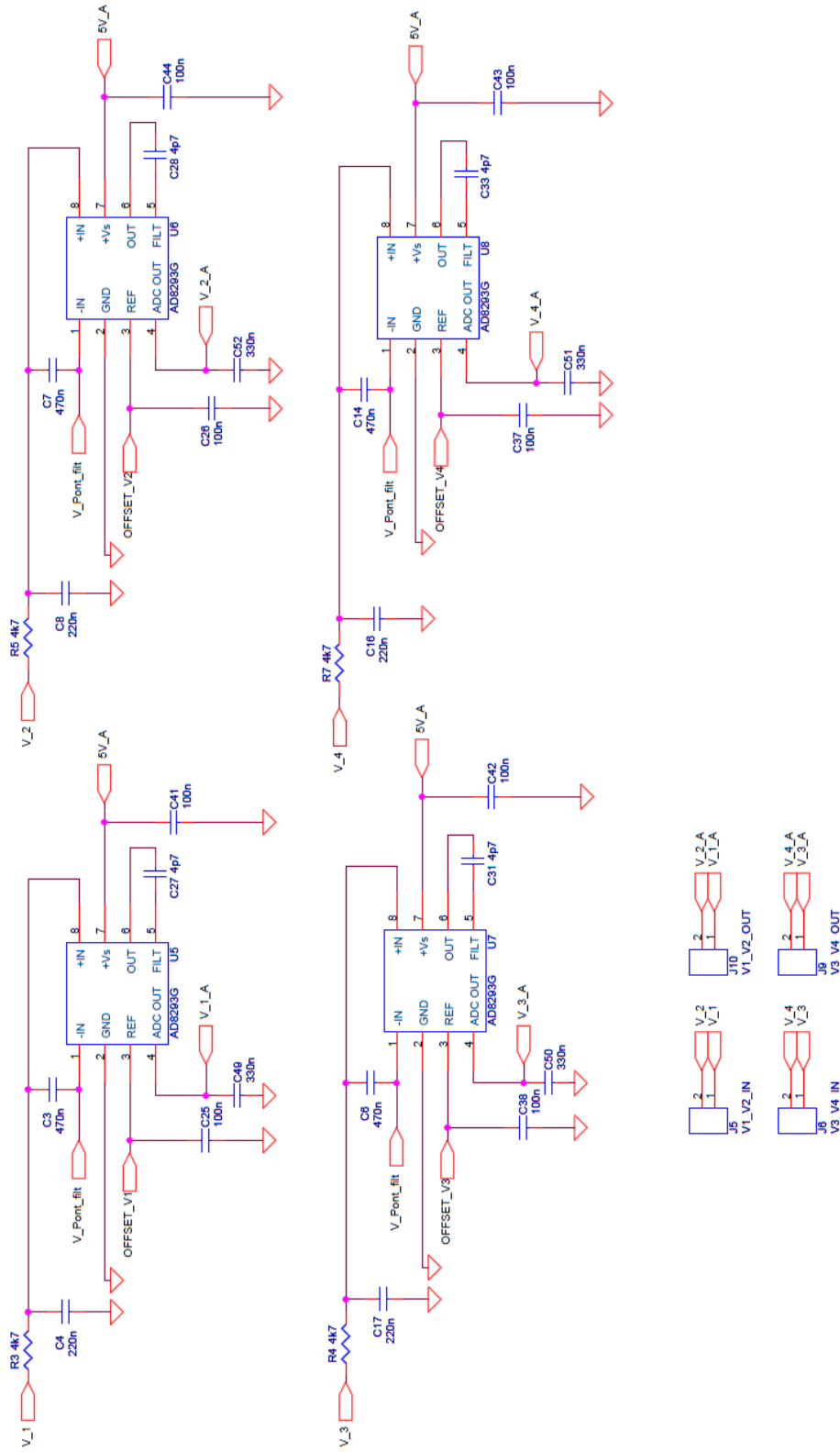
[34] K. Kalantar-zadeh, Sensors: An Introductory Course, DOI 10.1007/978-1-4614-5052-8\_2, # Springer Science+Business Media New York 2013

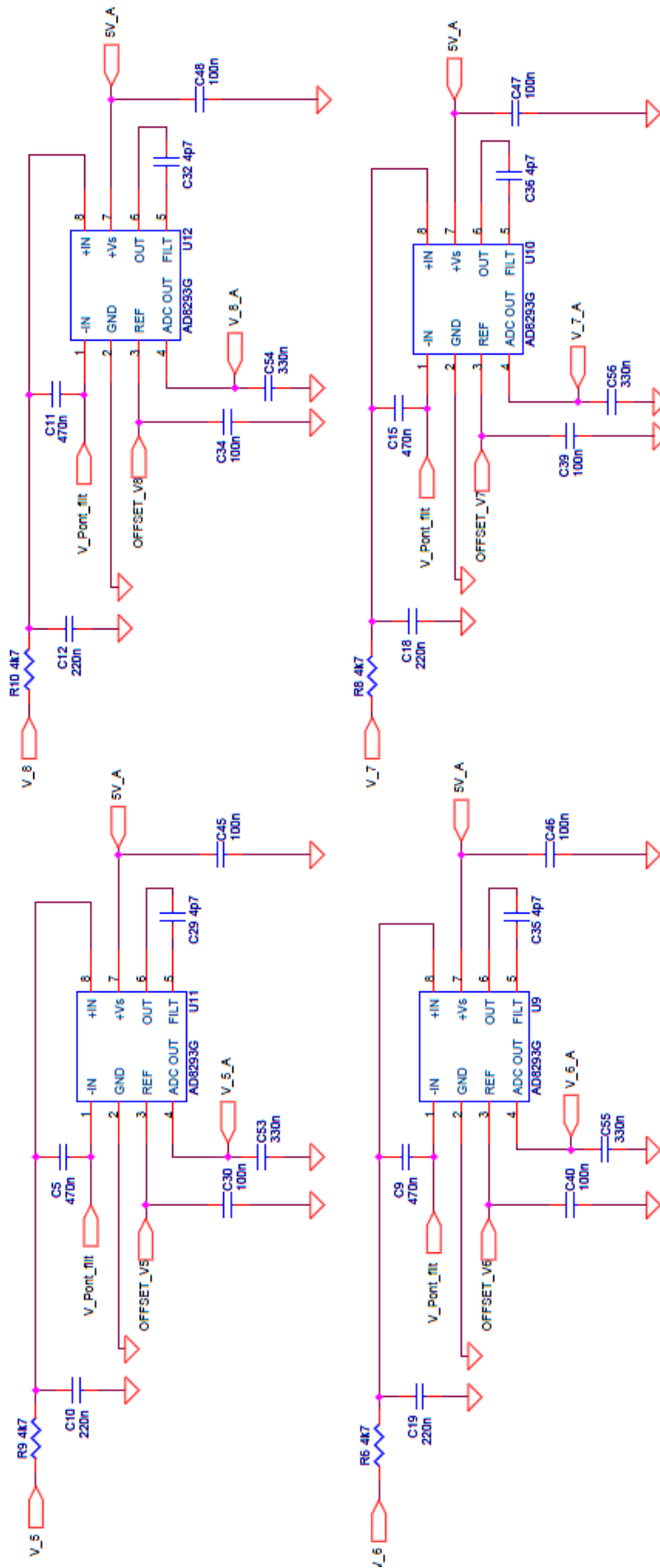
[35] Richard M. Voyles, Jr., J. Daniel Morrow, THE SHAPE FROM MOTION APPROACH TO RAPID AND PRECISE FORCE/TORQUE SENSOR CALIBRATION

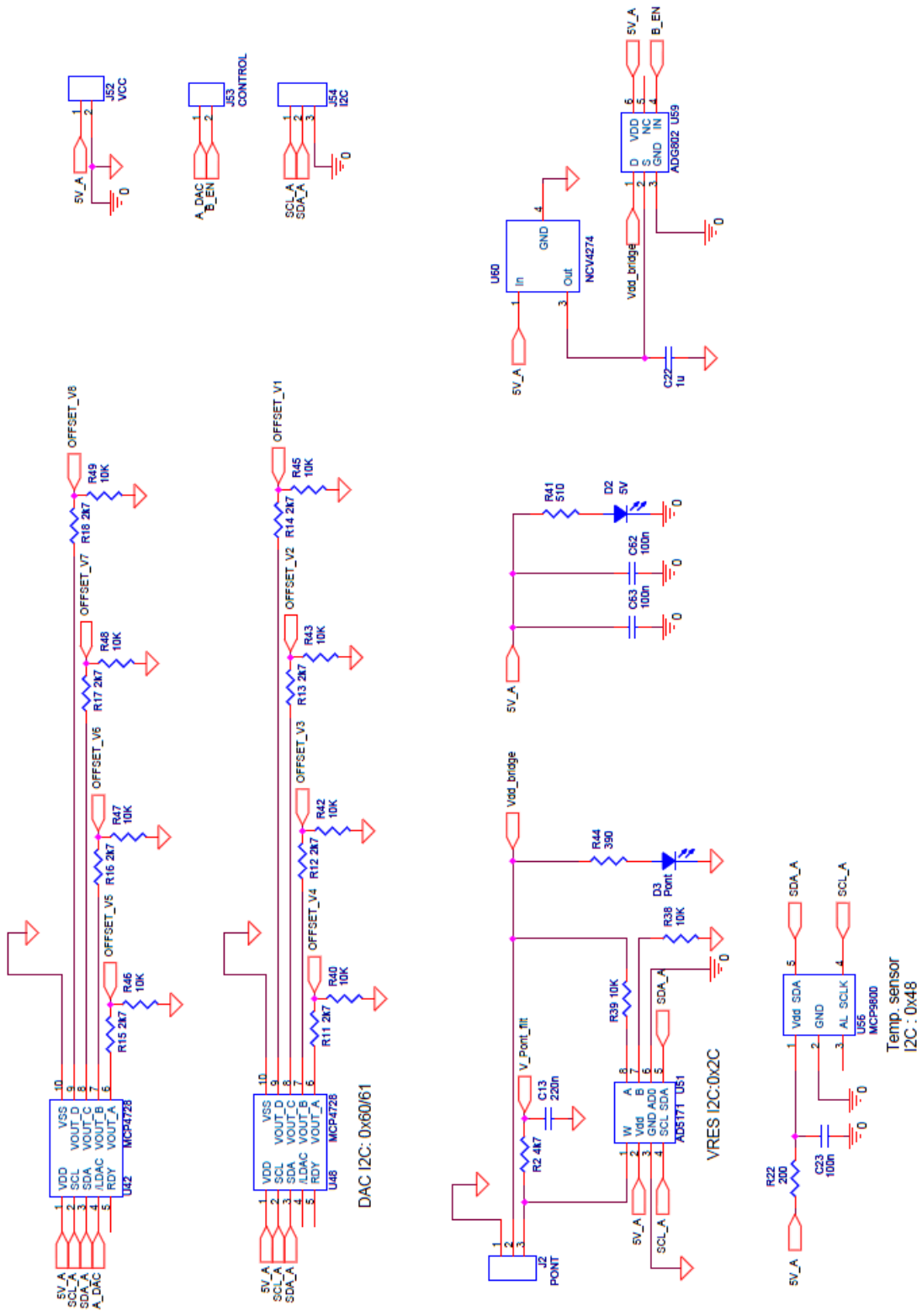
[36] Lu-Ping Chao, Ching-Yan Yin, The six-component force sensor for measuring the loading of the feet in locomotion, Department of Mechanical Engineering, Feng Chia University, Taichung, Taiwan. 18 January 1999

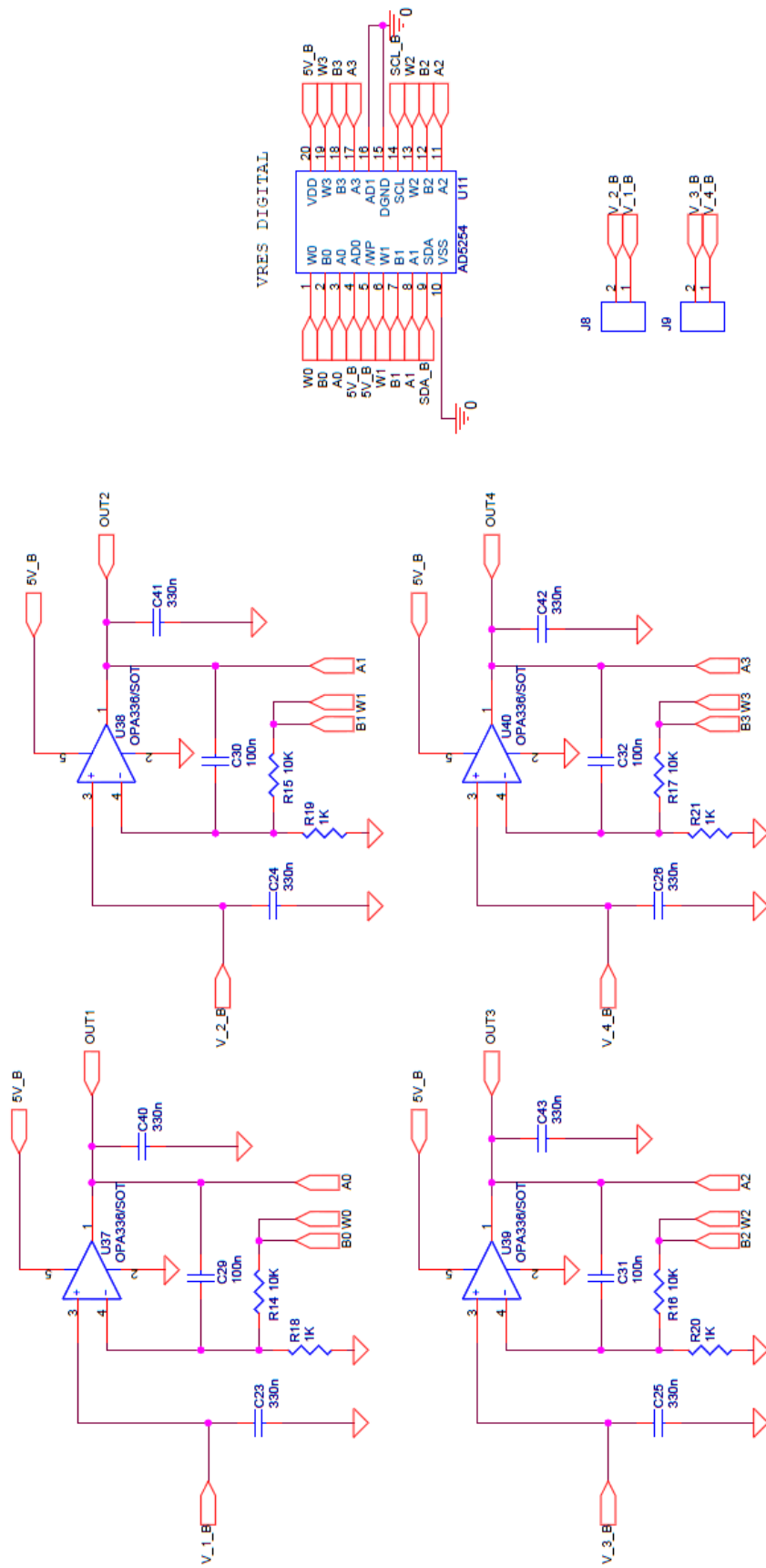
# Annexes

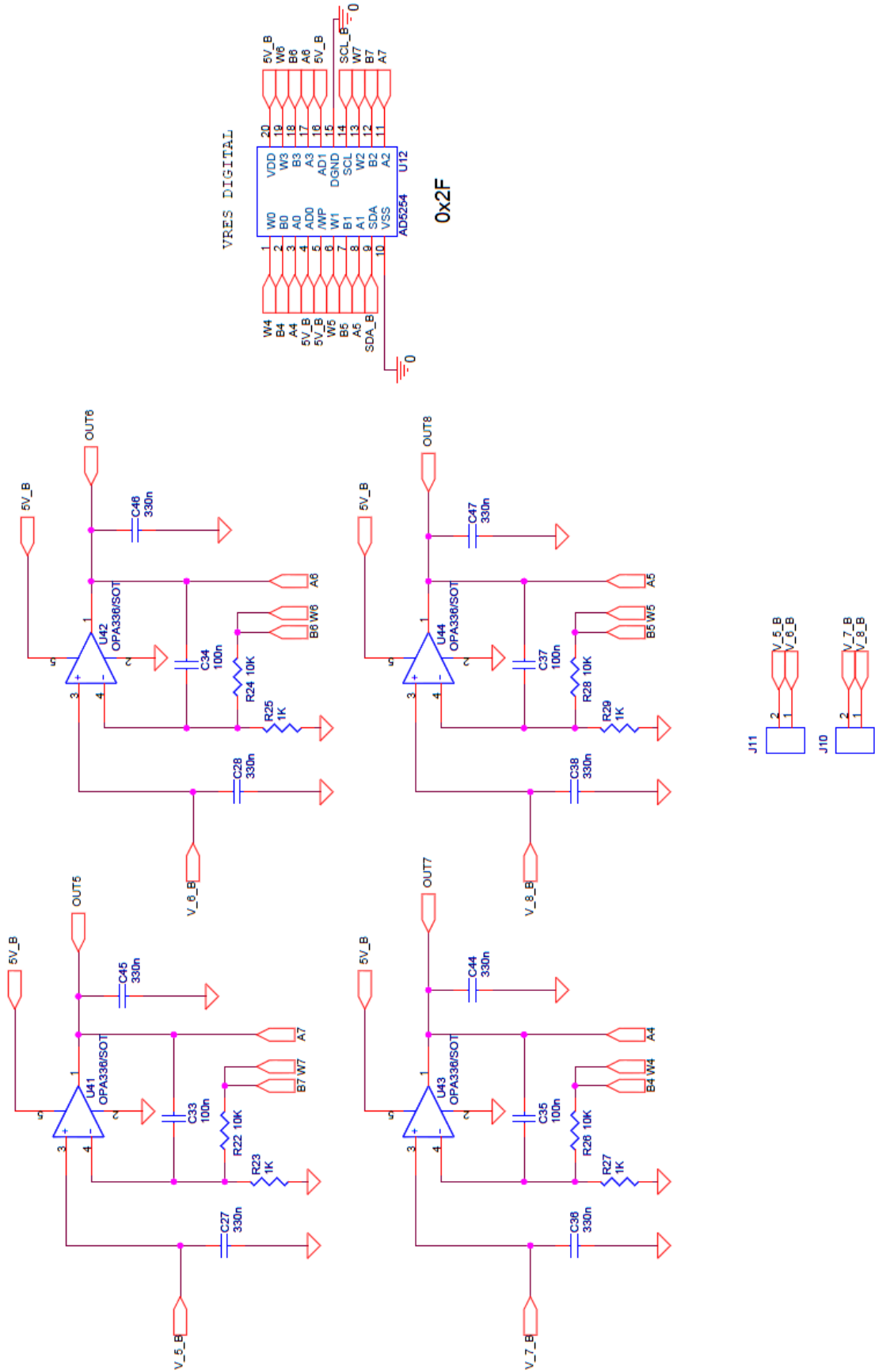
## ANNEX A (Schematics)

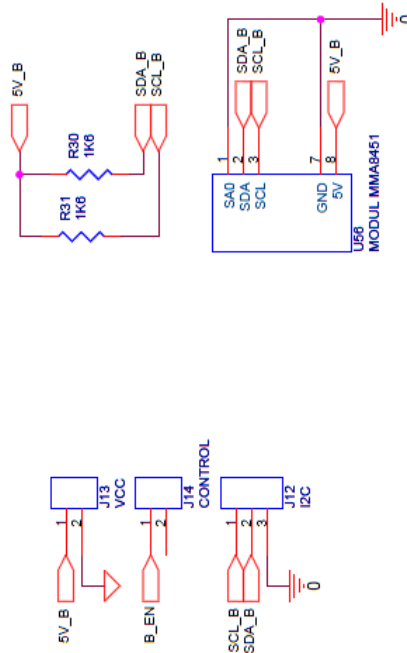
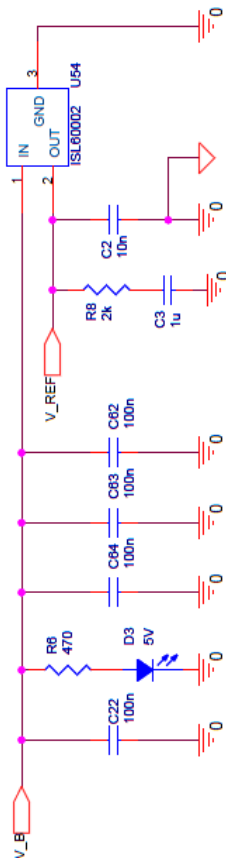
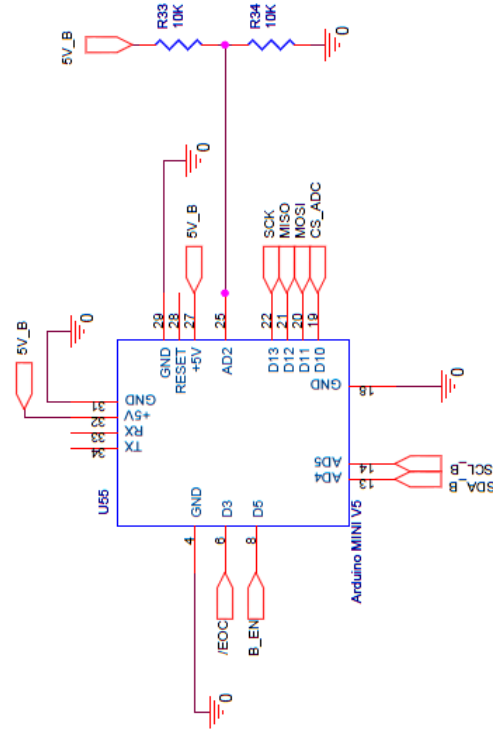
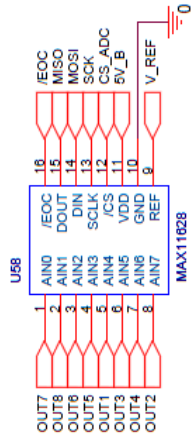






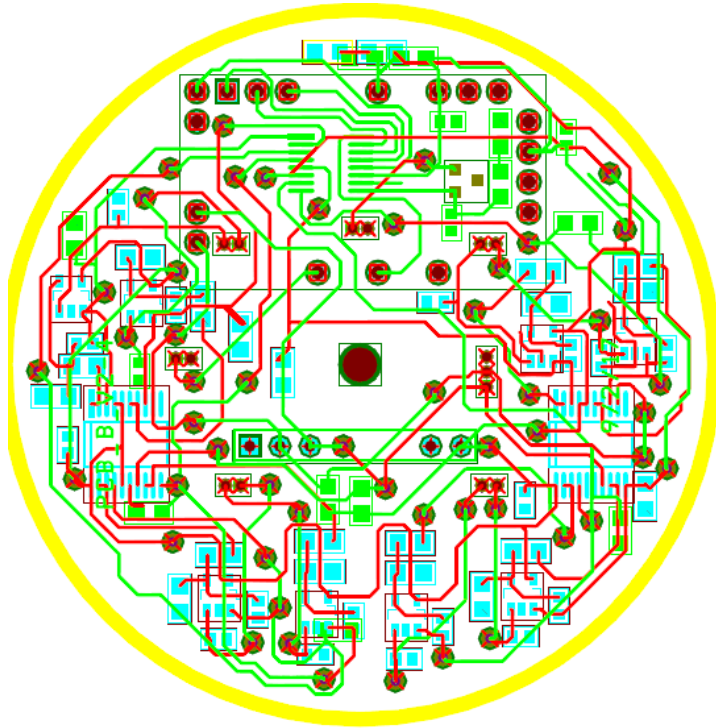




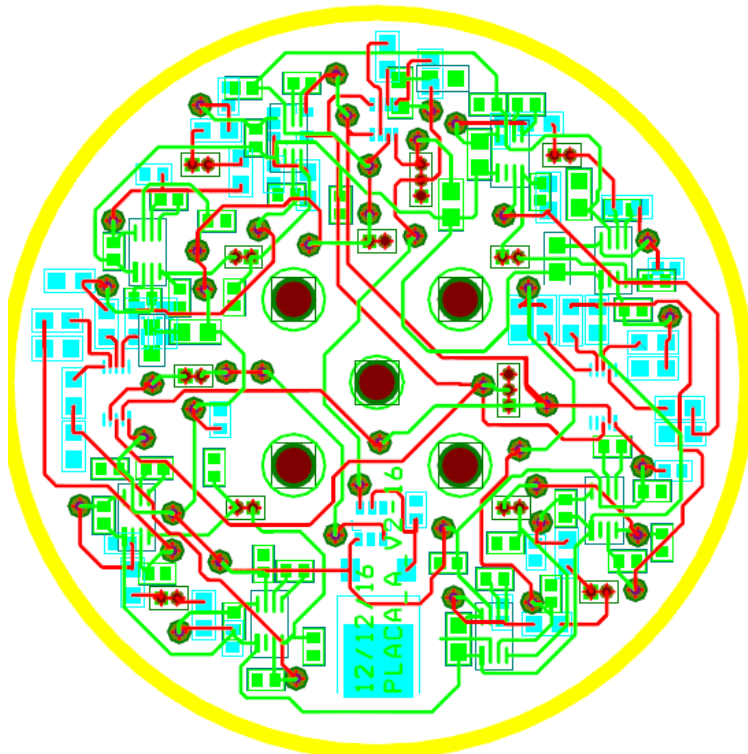


ANNEX B (PCB)

PCB\_B\_V4



PCB\_A\_V16





## ANNEX C (Component prices)

Component	Name	Value/Reference	Qty.	RS-reference	Price unit	Total price
Resistor	R22	200/0,125W	1	675-1068	0,012 €	0,012 €
Resistor	R44	390/0,125W	1	223-0360	0,012 €	0,012 €
Resistor	R41	510/0,125W	1	920-7128	0,012 €	0,012 €
Resistor	R9, R10, R6, R8, R3, R5, R4, R7, R2	4K7/0,125W	9	662-0486	0,012 €	0,108 €
Resistor	R39, R38, R46, R47, R48, R49, R40, R41, R42, R43, R45	10K/0,125W	11	666-2594	0,012 €	0,132 €
Resistor	R11, R12, R13, R14, R15, R16, R17, R18	2K7/0,125W	8	770-8925	0,012 €	0,096 €
Capacitor	C29, C32, C35, C36, C27, C28, C31, 33	4p7/6V	8	616-9206	0,003 €	0,022 €
Capacitor	C30, C45, C34, C48, C40, C46, C39, C47, C25, C41, C38, C42, C26, C44, C37, C43, C63, C62, C23	100n/6V	19	391-246	0,005 €	0,095 €
Capacitor	C22	1u/6V	1	435-1403	0,004 €	0,004 €
Capacitor	C12, C18, C19, C4, C8, C17, C16, C13	220n/6V	8	391-135	0,008 €	0,064 €
Capacitor	C5, C11, C9, C15, C3, C7, C6, C14	470n/6V	8	616-9688	0,006 €	0,045 €
Capacitor	C53, C54, C55, C56, C49, C52, C50, C51	330n/6V	8	147-522	0,008 €	0,064 €
IC	U5, U6, U7, U8, U11, U9, U12, U10	AD8293G160	8	819-7332	1,140 €	9,120 €
IC	U56	MCP9800	1	668-7215	1,140 €	1,140 €
IC	U60	NCV4274	1	757-7184	1,205 €	1,205 €
IC	U59	ADG802	1	820-9208	2,218 €	2,218 €
IC	U51	AD5171	1	820-9680	1,942 €	1,942 €
IC	U42, U48	MCP4728	2	687-8736	1,820 €	3,640 €
Led	D2, D3	HSMG-C170	2	435-6767	0,227 €	0,454 €
Connector	J5, J10, J6, J9, J8, J12, J7, J11, J50	Molex Pico 2w	9	279-9213	0,250 €	2,250 €
Connector	J52, J54, J2	Molex Pico 3w	3	319-1064	0,304 €	0,912 €
Connector	J8, J12, J7, J11, J5, J10, J6, J9, J2	Base múltiple 2w	1	267-7416	1,200 €	1,200 €
Connector	J2	Base múltiple 3w	1	896-7620	0,054 €	0,054 €
						24,801 €

